Technical Design Report
for J-PARC E63 experiment
"Gamma-Ray Spectroscopy of Light Λ Hypernuclei II"

Y. Akazawa, M. Fujita, M. Ikeda, H. Kanauchi, T. Koike, K. Miwa, S. Nagao, Y. Ogura, S. Ozawa, H. Tamura(spokesperson), Y. Sasaki, T. Yamamoto
Department of Physics, Tohoku University, Japan

K. Aoki, T. Takahashi, M. Ukai
Institute of Particle and Nuclear Studies, High Energy Accelerator Research Organization (KEK), Japan

K. Hosomi, S. Sato, K. Tanida
Advanced Science Research Center, Japan Atomic Energy Agency (JAEA), Japan

P. Evtoukhovitch, Z. Tsamalaidze
Joint Institute for Nuclear Research, Russia

J. Lee, T. Moon, S. Yang
Department of Physics and Astronomy, Seoul National University, Korea

R. Honda
Department of Physics, Osaka University, Japan

K. Shirotori
Research Cetner for Nuclear Physics, Osaka University, Japan

E. Botta
Dipartimento di Fisica, Universitá di Torino, and
Istituto Nazionale di Fisica Nucleare (INFN), Sezione di Torino, Italy

A. Feliciello
Istituto Nazionale di Fisica Nucleare (INFN), Sezione di Torino, Italy

M. Agnello
Dipartimento di Scienze Applicate e Tecnologia, Politecnico di Torino, Italy

J.K. Ahn, S. Kim
Korea University, Korea

T. Wang
Beihang University, China

1 Introduction

Following our successful runs of the E13 (1st part) experiment for γ-ray spectroscopy of ${}^{4}_{\Lambda}$He and ${}^{19}_{\Lambda}$F hypernuclei performed in April and June, 2015, we proposed in the previous PAC meeting held in January, 2016, the next-step experiment for hypernuclear γ-ray spectroscopy to investigate ${}^{4}_{\Lambda}$H and ${}^{7}_{\Lambda}$Li. It was stage-1 approved as E63.

1.1 Summary of the E63 proposal

The purposes of the E63 experiment are as follows.

(1) We will measure the ${}^{4}_{\Lambda}\mathrm{H}(1^+ \to 0^+)$ γ transition energy with Ge detectors to definitely confirm a large charge symmetry breaking effect in $A = 4$ hypernuclei, which was found in our previous experiment J-PARC E13 by observing the ${}^{4}_{\Lambda}\mathrm{He}(1^+ \to 0^+)$ γ transition [1], and to provide reliable and precise data to theorists.

(2) We will precisely measure the g-factor of Λ hyperon in a nucleus via γ-ray spectroscopy of ${}^{7}_{\Lambda}$Li hypernuclei. It will be the first measurement of the baryon's g-factor inside a nucleus. It may reveal a possible modification of a baryon in nuclear matter due to a possible effect of partial restoration of chiral symmetry and/or baryon-baryon mixing in nuclear matter.

Employing the K1.1 beam line and the SKS spectrometer system, we produce excited states of these hypernuclei using 0.9 GeV/c and/or 1.1 GeV/c (K^-, π^-) reaction. We detect γ rays from hypernuclei using Hyperball-J, a large germanium detector array developed for hypernuclear γ-ray spectroscopy at J-PARC and successfully employed in E13.

(1) For the ${}^{4}_{\Lambda}$H study, the ${}^{4}_{\Lambda}\mathrm{H}(1^+)$ state is produced by ${}^{7}\mathrm{Li}(K^-,\pi^-)$ reaction as a hyperfragment via highly excited unbound ${}^{7}_{\Lambda}\mathrm{Li}^*$ states, and the $1^+ \to 0^+$ γ-ray energy will be determined in a 5 keV accuracy. We request 6 days for the ${}^{4}_{\Lambda}$H run.

(2) We will measure the reduced transition probabilities ($B(M1)$) of the Λ spin-flip $M1$ transitions and extract the g-factor of the Λ inside a nucleus. For this purpose, we measure the ${}^{7}_{\Lambda}\mathrm{Li}(3/2^+ \to 1/2^+)$ lifetime, where the $3/2^+$ state is populated from the $1/2^+(T = 1)$ state via the fast $1/2^+(T = 1) \to 3/2^+$ transition as well as from the spin-flip direct production of the $3/2^+$ state. A Li_2O target is used to optimize the stopping time in the target for Doppler shift attenuation method. In order to measure the $B(M1)$ value in an accuracy of 6%, (which corresponds to the accuracy of 3% in $|g_\Lambda - g_c|$), about 2000 events of $3/2^+ \to 1/2^+$ γ ray is necessary. We request 35 days for physics run.

In both measurements, we assume beam intensities of 1.8×10^5 K^- beam per spill for $p_{K^-} =$ 1.1 GeV/c and 0.56×10^5 K^- beam per spill for $p_{K^-} = 0.9$ GeV/c, that are expected for 50 kW and 6 s cycle operation of the accelerator.

Before the physics run, we study the sensitivity for $B(M1)$ measurement by taking test data at 1.1 and 0.9 GeV/c K^- momenta for 2 days each. In addition, we request 10 days for a detector commissioning and beam tuning at 1.1 and 0.9 GeV/c, and 5 days for various control runs.

The upstream part of the K1.1 beam line has been used for E36 as the K1.1BR line, but the downstsream part of the K1.1 beam line needs to be prepared. Almost all the detectors for the K1.1/SKS spectrometers and Hyperball-J are ready. We will be ready to run this experiment after the E03 experiment at K1.8 probably in 2017.

See the E63 proposal [2] for details of the experiment.

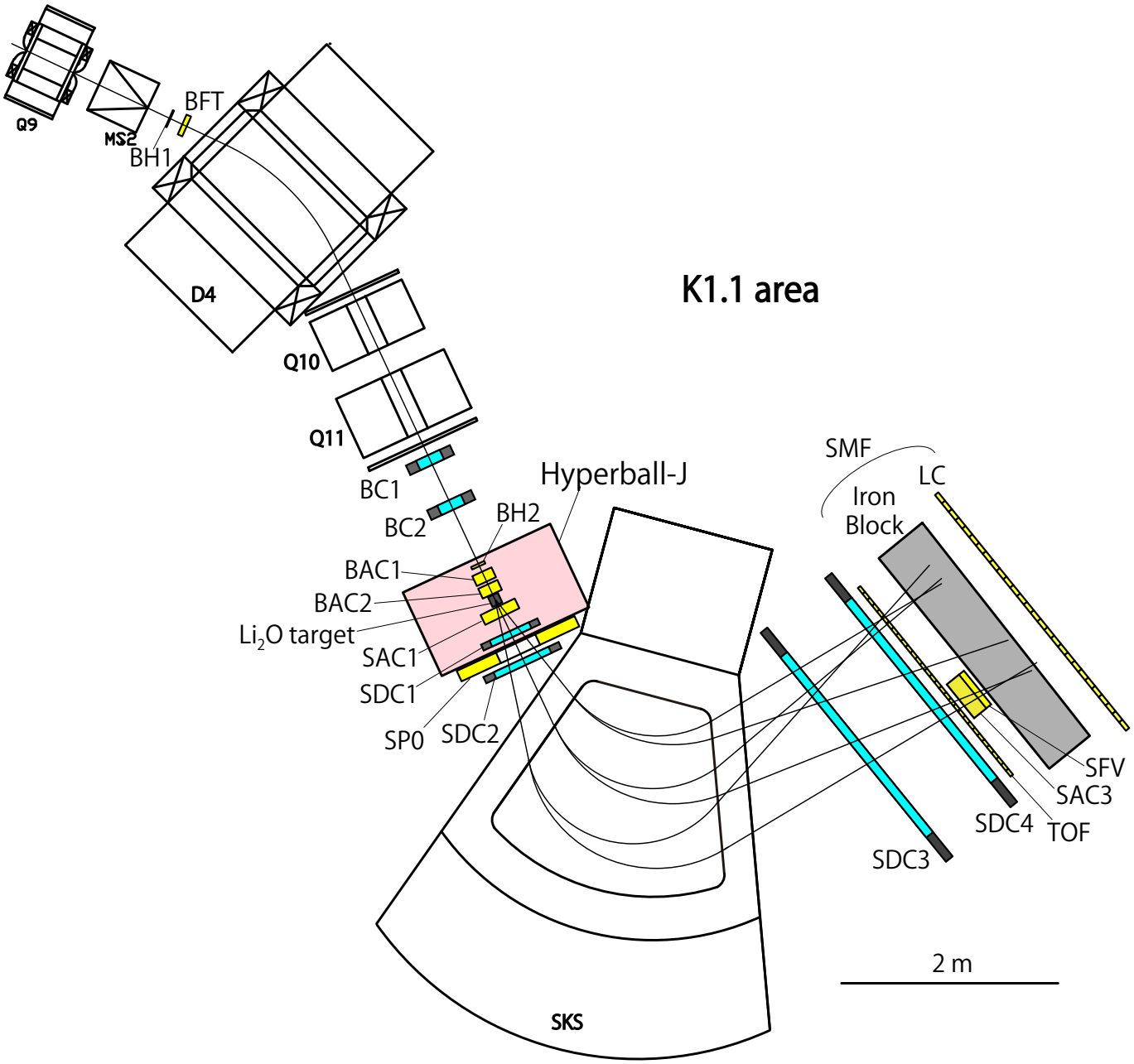

Figure 1: Experimental setup for the K1.1 beam spectrometer, the SKS spectrometer, and detectors around the target.

1.2 Difference between E13 and E63

The experimental setup for E63 is shown in Fig. 1. It is essentially the same as the previous experiment E13 which we successfully carried out at the K1.8 beam line in 2015. The experimental conditions and setup are compared between E13 and E63 in Table 1. The SKS magnet has been already moved to the K1.1 area from K1.8, while the downstream part of the K1.1 beam line has to be prepared.

Table 1: Comparison of experimental conditions and setup between E13 and E63.

Experiment	E13	E63
Beamline	K1.8	K1.1
Beam K^- momentum	1.5 and 1.8 GeV/c	0.9 and 1.1 GeV/c
Beam K^- intensity / spill	3–4$\times 10^5$	0.6 and 1.9$\times 10^5$ (expected)
Target	liquid ^{4}He and liquid CF_4	^{7}Li (metal) and Li_2O
π^- momentum of interest	1.4 and 1.7 GeV/c	0.8 and 1.1 GeV/c
SKS entrance angle	15°	25°
SKS bending angle (central track)	55°	100°
SKS peak acceptance	105 and 95 msr	130 and 130 msr

Almost all the detectors for the K1.1 spectrometer, the SKS spectrometer, and the Hyperball-J Ge detector array were successfully used at K1.8 in E13 and will be installed again at K1.1. Table 2 lists all the detectors to be used for E63 showing whether they need to be changed or not from E13.

Table 2: Detectors for E63 changed or unchanged from E13.

BH1	Unchanged from E13
BFT	Enlarge the horizontal size: $\pm$80 mm $\rightarrow$ $\pm$140 mm
BH2	Unchanged from E13
BC3,BC4	Unchanged from E13
BAC1,BAC2	Unchanged from E13
BH2	Unchanged from E13
SAC1	Change the radiator: n =1.03$\rightarrow$1.05
SP0	Unchanged from E13
SDC1,SDC2	Unchanged from E13
SAC3/SFV	Change the radiator: n =1.03$\rightarrow$1.05 / Unchanged from E13
SDC3,SDC4	Unchanged from E13
TOF	Same as E13 (unchanged)
SMF Iron Block	Change the thickness: 75 cm + 50 cm $\rightarrow$ 50 cm only
SMF LC	Unchanged from E13
Hyperball-J	Unchanged from E13, but Ge positions are optimized.

Details of those detectors are described in the following sections.

2 K1.1 Beam Line

Figure 2 shows the K1.1 beam line and the K1.1 experimental area.

The K1.1 beam line is designed to deliver high purity kaon beams up to 1.1 GeV/c employing double-stage electrostatic separators (ESS1, ESS2) together with an intermediate focus point (IF). The layout of K1.1 and the beam envelope are shown in Fig. 2, and the specifications are

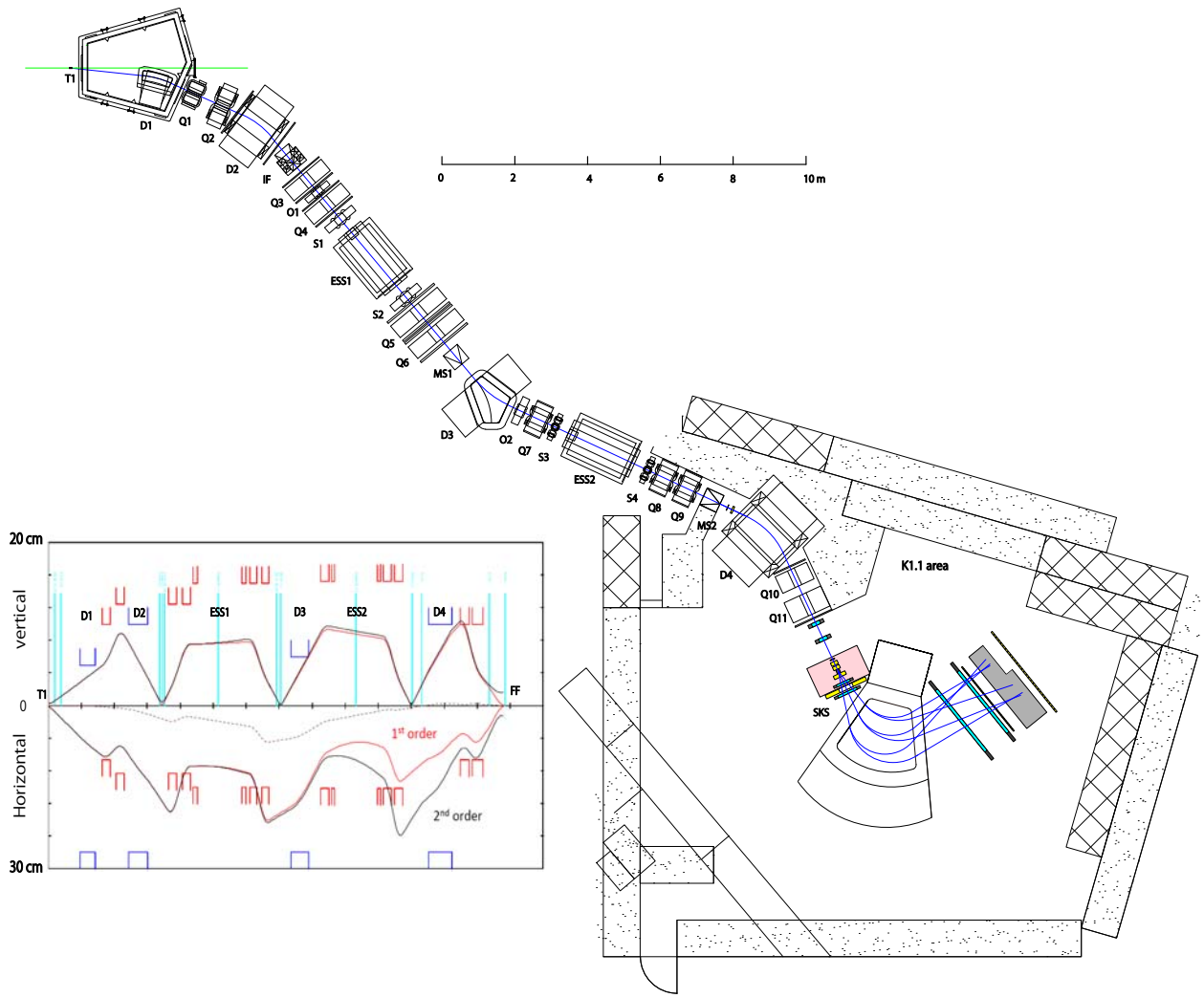

Figure 2: Layout of the K1.1 beam line and the K1.1 area. The calculated beam envelope is also shown.

listed in Table 3. The upstream part of K1.1 has been successfully operated as the K1.1BR line. The downstream part after D3 needs to be prepared.

The K^- intensity and purity depend on the openings of the intermediate focus slit (IF) and the two mass slits (MS1, MS2). Table 4 shows the results of simulations using Decay Turtle code with various slit openings. The highest K^- intensity with a reasonably small π^- contamination was found as 1.89×10^5 K^-/spill (with a $K^-/(K^-+\pi^-)$ ratio of 0.37) for $p_{K^-} =$ 1.1 GeV/c, where the proton beam intensity of 5×10^{13} per spill (40 kW beam power for 6 s cycle operation) and a 50%-loss production target are assumed. The electric field of ESS1 and ESS2 is assumed to be 70 kV/cm ($\pm$350 kV at the electrodes). The beam size at the focusing point is smaller than $\pm$ 2 cm for horizontal and vertical directions. In the same slit openings, the K^- intensity at 0.9 GeV/c is expected to be 0.6×10^5 K^-/spill.

Table 3: Specifications of the K1.1 beam line.

Maximum momentum	1.1 GeV/c
Extraction angle	6°
Length	28.13 m
Momentum bite	±3%
Electric separator	11.88 m ×2, E =75kV/cm (max)

Table 4: Expected K^- yield per spill and purity at the K1.1 beam line simulated with the Decay Turtle code. The proton beam intensity of 5×10^{13} per spill (40 kW beam power for 6 s cycle) and the production target of 50% loss is assumed. IFV is the opening of the vertical slit at the intermediate focus point, and MS1/MS2 are the openings of the first and the second mass slit (vertical).

	IFV: ±1.5 mm	IFV: ±3.0 mm
MS1/MS2: ±1.0 mm	1.18×10^5 (98%)	1.21×10^5 (98%)
MS1/MS2: ±1.5 mm	1.64×10^5 (89%)	1.88×10^5 (28%)
MS1/MS2: ±2.0 mm	1.89×10^5 (37%)	2.51×10^5 (78%)

3 Beam spectrometer and beam counters

At the K1.1 beam line, the last bending magnet (D4) together with Q10 and Q11 plays a role of the beam spectrometer. The dipole magnet D4 has a effective field length of 1.4 m with the maximum field of 1.8T. During the beam time, the central field will be measured and monitored via a Hall probe installed in the gap.

At the entrance of D4 we will install a tracking device (BFT) made of ϕ1 mm scintillating fibers is installed, providing a powerful means to select a true track when multiple beam tracks are recorded. We successfully used the same type of detector for E10, E27 and E13 at K1.8. At the exit of the beam line, we install 1 mm-pitch MWPC's (BC3, BC4) which were used as BC1 and BC2 at the upstream of the beam line spectrometer at K1.8 for the E19 and E10 experiments. We install plastic scintillator hodoscopes (BH1, BH2) to separate K^- and π^- in the beam by time-of-flight.

The momentum resolution of the K1.1 beam line spectrometer is estimated to be 0.042% (FWHM) according to the simulation, which gives a negligible effect to the energy resolution of the hypernuclear mass spectrum with our thick targets (∼20 g/cm^2). The actual momentum resolution would be worse due to multiple scattering of the beam particles on BC3 and possible misalignment of BFT, BC3 and BC4 with respect to the D4 magnet. The momentum resolutions of the K1.1 spectrometer and the SKS spectrometer will be checked via beam-through data in the commissioning run, and the missing mass resolution will be measured with the $K^-p \to \Sigma^+\pi^-$ and $K^-\ ^{12}\mathrm{C} \to {}^{12}_{\Lambda}\mathrm{C}(\mathrm{gs})\ \pi^-$ reactions.

The kaon beam is irradiated on a 26 cm-thick ^{7}Li target and a 10 cm-thick $^{nat}Li_2O$ target. Just upstream and downstream of the target, aerogel Cerenkov counters (BAC1,2 and SAC1) (see Fig. 14) are located to identify kaons in the beam and pions in the scattered particles. Beam particles unscattered or scattered at very forward angles are detected by the SFV counter

located downstream of the TOF counter. The SFV signal is used to veto the trigger.

Expected specifications of the K1.1 beam line spectrometer are listed in Table 5.

Table 5: Specifications of the beam line spectrometer.

Maximum momentum	1.1 GeV/c
Bending angle	40°
Flight path	∼5.2 m
Effective field length and strength of D4	1.4 m, 1.8 T
Momentum resolution (expected)	4.2×10^{-4} (FWHM)

3.1 Counters for particle identification

The beam line spectrometer is equipped with counters for particle identification. Incident kaons are particle-identified by aerogel Čerenkov counters (BC1 and BC2) at the trigger level and by the time-of-flight method in the off-line analysis with the timing counters (BH1 and BH2). BH2 is used as a timing reference counter for all other detectors. Specifications of these counters are listed in Table 6.

Time-of-flight counters

Beam particles are identified by the time-of-flight method using horizontally segmented plastic scintillation counters located at upstream (BH1) and at the downstream (BH2) of the K1.1 spectrometer. The flight path length between BH1 and BH2 is typically 5.2 m. BH1 and BH2 have thickness of 5 mm and 8 mm, respectively. In the E13 experiment, the BH1-BH2 time-of-flight resolution was 155 ps (rms) for K^- at 1.5 GeV/c as shown in Fig. 5. The figure indicates perfect separation between kaons and pions. In K1.1, the flight length between BH1 and BH2 is only 5.2 m, much shorter than the K1.8 case (11.1 m). However, the time-of-flight difference between 1.1 GeV/c K^- and π^- at K1.1 is 1.53 ns, which is comparable to the case of 1.5 GeV/c at K1.8 (1.8 ns) and much longer then the time resolution of σ =155 ps.

Aerogel Čerenkov counters

Threshold-type aerogel Čerenkov counters (BAC1 and BAC2) are installed at the upstream of the experimental target. These counters should be placed as close to the target as possible to minimize contamination from beam K^- decay events in the trigger. Figure 3 shows the refractive index threshold for Čerenkov radiation as a function of momentum. The refractive index is chosen to be 1.03, corresponding to the threshold momentum of 0.6 GeV/c for pions and 2.0 GeV/c for kaons. It worked well in E13 for 1.5 and 1.8 GeV/c beam, and can be also used for 1.1 and 0.9 GeV/c in E63. Figure 4 shows a schematic view of the BAC1,2 used in E13. BACs cover 160 × 52 mm^2 area with a 66-mm thick silica aerogel radiator, of which length is optimized. Polytetrafluoroethylene $(CF_2)_n$ is chosen for inner diffused-type reflector. For BACs, three 2" fine-mesh type PMTs, Hamamatsu H6614-70UV, are connected to the radiator directly. By summing up analog signals from three PMTs before discriminators, K/π

Table 6: Specifications of counters for particle identification

Detector	Effective area W × H × T [mm]	Spec.	PMT (Hamamatsu)
BH1	170 × 66 × 5	11 segments, double-side readout, booster	H6524MOD
BH2	111 × 50 × 8	5 segments, single-side readout, booster	H6524MOD
BAC1	160 × 57 × 66	1 segment, 3 PMTs readout	H6614-70UV
BAC2	160 × 57 × 66	1 segment, 3 PMTs readout	H6614-70UV
SAC1	342 × 80 × 66	1 segment, 5 PMTs readout	H6614-70UV
TOF	2240 × 1000 × 30	32 segments, double-side readout	H1949
SFV	400 × 200 × 8	6 segments, single-side readout	H3167
SAC3	400 × 200 × 120	1 segment, 16 PMTs readout	R6681
SP0	1200 × 1100 × 8 (×8 layers)	6 segments, 8 layers, double-side readout	R980
SMF LC	2800 × 1400 × 40	28 segments, double-side readout	H1949, H6410

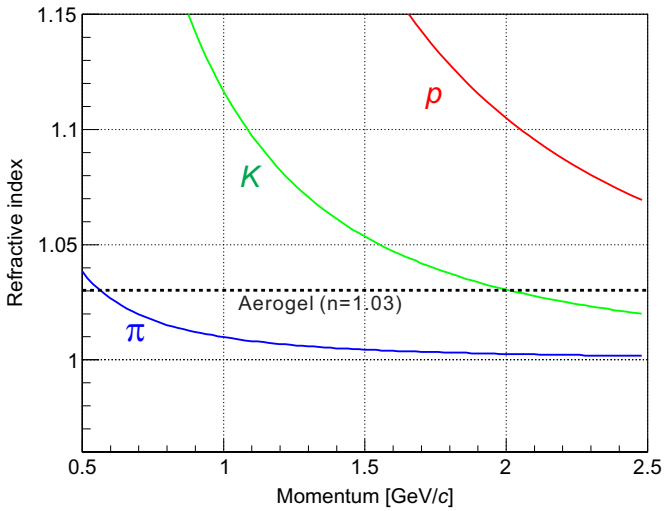

Figure 3: Threshold of refractive index for Čerenkov radiation as a function of momentum.

separation was improved. The performance of each of BAC1 and BAC2 was investigated using 1.3–1.8 GeV/c K^- and π^- beams and the π^- detection efficiency was found to be more than 99.5% with a misidentification rate of K^- as π^- being less than 2.5% [3].

The two counters (BAC1 and BAC2) are necessary because the beam pions that are misidentified as kaons directly increase the trigger rate. The beam K^- trigger ("K_{in} trigger") is defined

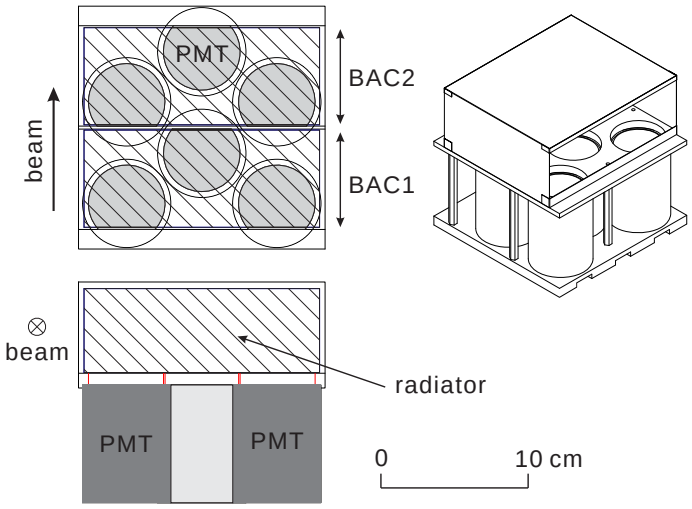

Figure 4: Schematic view of BAC1,2. An effective area is 160 × 52 mm^2 with a 66-mm thick silica aerogel radiator ($n = 1.03$). Three 2" fine-mesh type PMTs, Hamamatsu H6614-70UV, are connected on the radiator directly.

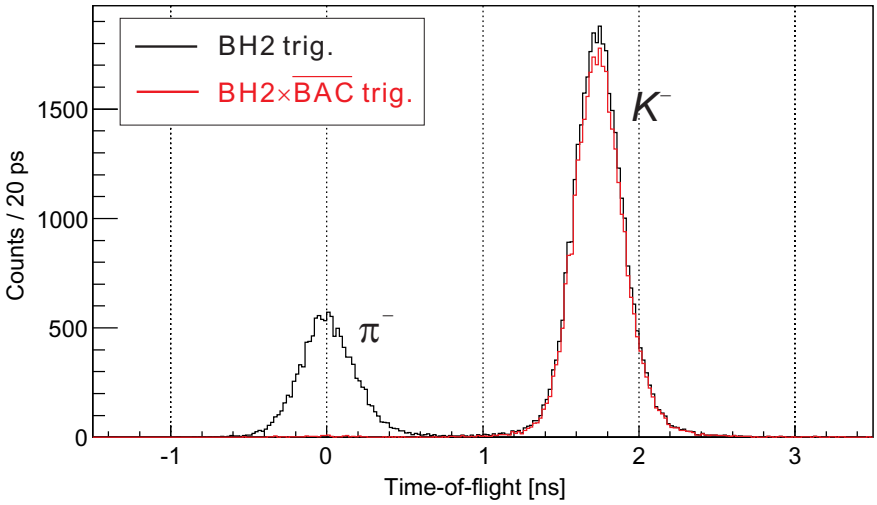

Figure 5: A time-of-flight (= BH2 − BH1) distribution with at typical beam condition in E13 for 1.5 GeV/c. Black and red lines show the distributions with the BH2 trigger and the BH2×$\overline{\text{BAC1}}$ × $\overline{\text{BAC2}}$ trigger, respectively.

as BH2×$\overline{\text{BAC1}}$ × $\overline{\text{BAC2}}$ (see Section 6.1 for the trigger system).

In a typical beam condition with $p_{K^-} = 1.5$ GeV/c in E13, the K_{in} trigger efficiency was more than 95% with a π^- misidentification rate of less than 3% in the trigger level as shown together in Fig. 5. The numbers of photo-electron were measured to be ∼20 per detector.

3.2 Tracking detectors

BFT

One scintillation fiber counter (BFT) and two multi-wire drift chambers (BC3,4) are used to measure the beam particle track. BFT is placed upstream of the DQQ magnets, and BC3,4 is placed downstream of them. The momenta of the beam particles are obtained by using track information from these detectors. Table 7 shows their specifications. BFT is a set of ϕ1 mm scintillation fibers arranged horizontally in two layers (xx') giving a 0.5 mm pitch as shown in Fig. 6 [4]. A Multi-Pixel Photon Counter (MPPC) device is connected to one end of each fiber. BFT was used in E10, E27, and E13 at K1.8 beam line and showed excellent performance; it had a time resolution better than 2 ns (FWHM) and clearly separated multiple beam tracks in unwanted bunched time structure of the slow extraction beam. It was confirmed at K1.8 that with this detector we can accept intense beam up to 3×10^7/spill (2 s) with a realistic bunched beam structure. The highest K^- plus π^- intensity of the 1.1 GeV/c K^- beam will be less than 5×10^5/spill(2 s) for 50 kW operation, which is much lower than the operation limit.

Since the horizontal beam size at the BFT position of the K1.1 beam line is expected to be larger ($\pm$120 mm) than that of K1.8 and cannot be covered with the existing BFT used in E13 with the horizontal size of $\pm$80 mm, we will fabricate a new BFT with the same specifications but the horizontal size of 140 mm.

BC3, BC4

The drift chambers, BC3,4, have six layers of sense-wire plane ($xx'uu'vv'$). x, u and v denote a vertical wire plane and a wire plane tilted by $\pm15°$, respectively. BC3,4 have a drift length of 1.5 mm with a typical position resolution of 0.2 mm (σ) for a sense plane as shown in Fig. 7.

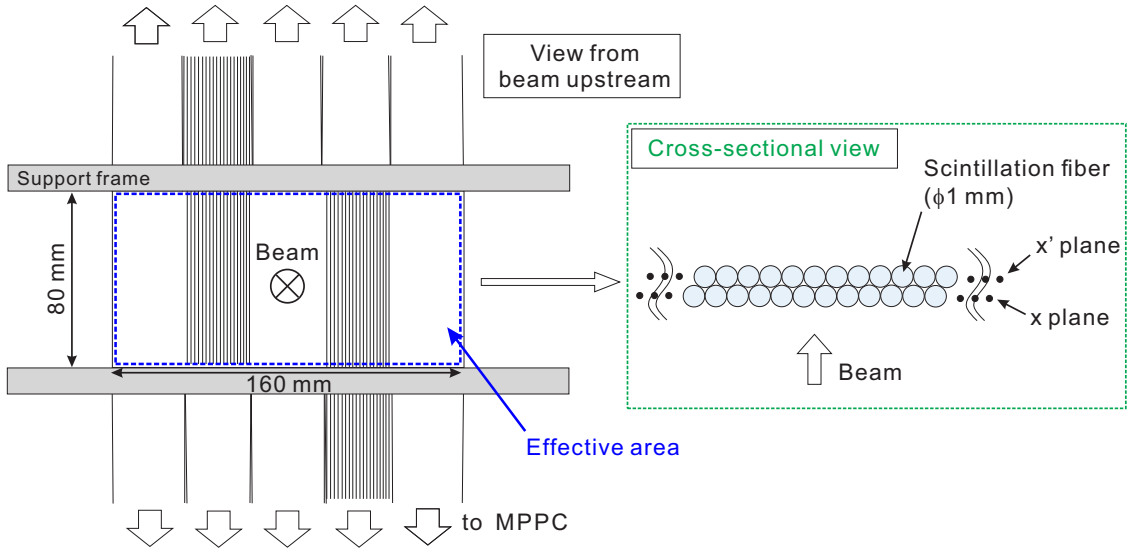

Figure 6: Schematic view of BFT. BFT was a set of ϕ1 mm scintillation fibers arranged horizontally in two layers(xx'). MPPC devices are connected to each fiber.

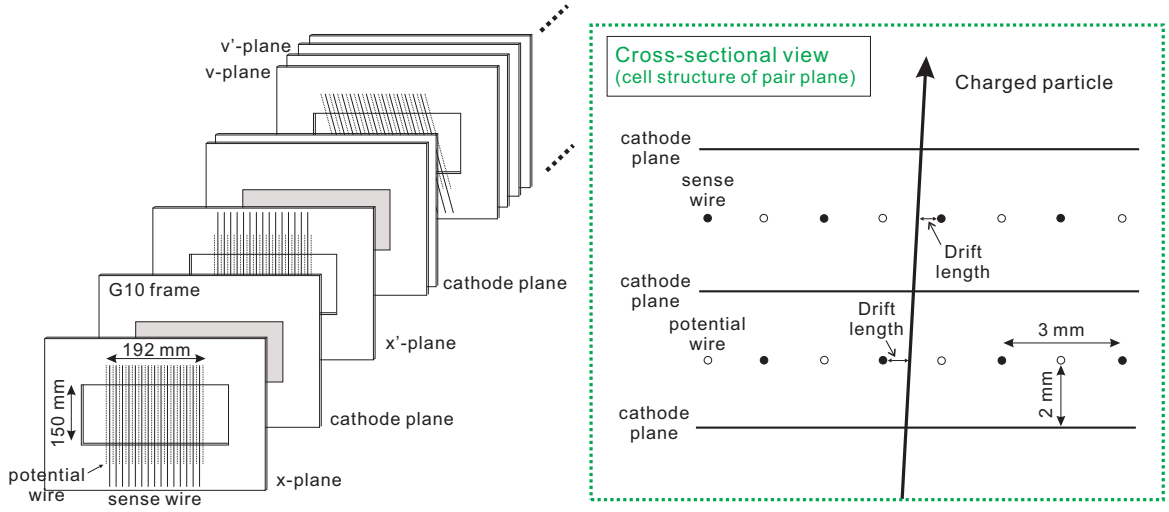

Figure 7: Schematic view of BC3.

This type of drift chambers were designed to be operational in high rate beam conditions in hadron beams and used in many experiments since 1990's at KEK-PS and then at J-PARC. We use the gas mixture of Ar:C_4H_{10}:Methylal = 76:20:4 at atmospheric pressure as we did in E13. In E63, we will employ the chambers that were used as BC1 and BC2 in E19 and E10 after maintenance.

Table 7: Specifications of the tracking detectors. BFT is a scintillation fiber detector and others are drift chambers. Typical position resolutions for a sense plane are listed.

Detector	Effective area W × H [mm]	Planes	Tilted angle (x, x') [deg.]	Diameter [mm]	resolution σ[mm]
BFT	160 × 80	xx'	0	1.0	0.15

Detector	Effective area W × H [mm]	Planes	Tilted angle (x, u, v) [deg.]	Drift length [mm]	resolution σ[mm]
BC3	192 × 150	$xx'vv'uu'$	0, +15, −15	1.5	0.20
BC4	192 × 150	$uu'vv'xx'$	0, +15, −15	1.5	0.20
SDC1	400 × 150	$xx'vv'uu'$	0, +15, −15	2.5	0.20
SDC2	560 × 150	$uu'xx'$	0, +15, −15	2.5	0.15
SDC3	2140 × 1140	$vxuvxu$	0, +30, −30	10.0	0.25
SDC4	2140 × 1140	$vxuvxu$	0, +30, −30	10.0	0.25

Table 8: Specifications of SKS spectrometer (SKS0 setting) for 1.1 GeV/c (K^-,π^-) reaction

Momentum acceptance	$0.7 - 1.1$ GeV/c
Momentum resolution	<0.2% (FWHM)
Bending angle	100°
Magnetic field at the center (coil current)	2.5 T (400 A)
Solid angle	140 msr at maximum
Flight path	$\sim$ 5 m

4 SKS spectrometer

Scattered π^- mesons are particle-identified and momentum-analyzed by the SKS spectrometer based on the SKS (Superconducting Kaon Spectrometer) magnet. The SKS spectrometer [5] has been used for reaction spectroscopy experiments at the KEK K6 beam line as well as at the J-PARC K1.8 beam line [6].

Due to spatial constraints in the K1.1 area, we choose the original spectrometer setting (called SKS0) with a larger tilted entrance angle with respect to the magnet edge (25°) and a larger bending angle of the central track (100°) which are different from the previous setting (SksMinus) used for E13 (the entrance angle of 25° and the bending angle of 55°). The SKS0 setting is characterized by a better momentum resolution and a larger peak acceptance than SksMinus, but a narrower momentum acceptance. The narrow momentum acceptance is not a problem for Λ hypernuclear production via the (K^-, π^-) reaction.

Specifications of the SKS spectrometer are summarized in Table 8. The features of SKS0 are listed as follow:

- A large acceptance of $\sim$140 msr at maximum.
- Momentum acceptance wide enough to cover hypernuclear production events, 0.7–1.1 GeV/c with 2.5 T excitation for the 1.1 and 0.9 GeV/c (K^-,π^-) reaction.
- A wide angular acceptance (0°–20°) covering almost all the angular range which contributes to the hypernuclear production for ${}^{7}_{\Lambda}$Li ($\theta_{K\pi}$ range characterized by angular momentum transfer of $\Delta L = 0$ and 1).
- A momentum resolution better than 0.2% (FWHM), which corresponds to a missing mass resolution of hypernuclei, $\sim$2 MeV (FWHM). Thus the mass resolution is determined by energy loss effect in the thick ^{7}Li ($\sim$ 15 g/cm^2) and Li_2O ($\sim$ 20 g/cm^2) targets.
- Excellent particle identification between kaons and pions in the on-line and the off-line levels by use of aerogelc Čerenkov counters (SAC1, SAC3) and time-of-flight measurement between the beam timing counter BH2 and the TOF hodoscope.
- Capability to suppress background events from decay of beam K^- such as $K^- \to \mu^-\nu$ and $K^- \to \pi^-\pi^0$, using a muon filter counter system, SMF, and a π^0 counter system, SP0.

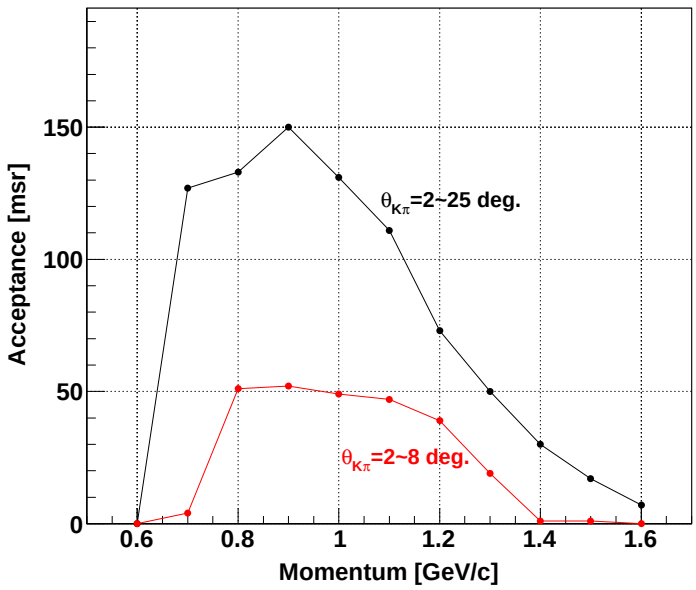

Figure 8: Solid angle of the SKS spectrometer (SKS0 setting, full excitation)) as a function of the scattered particle momentum, shown for all (K^-,π^-) scattering angles (black solid line) and forward angles (red dotted line).

The SKS spectrometer consists of a superconducting dipole magnet SKS, four sets of drift chambers (SDC1,2,3,4), four types of trigger counters (SAC1, TOF, SAC3, SFV) and two sets of counters for suppressing K^- beam decay events (SP0 and SMF) as shown in Fig.1. It covers scattering angles of $\pm 20^\circ$ in the horizontal direction and $\pm 5^\circ$ in the vertical direction. The SKS magnet is fully excited to 2.5 T (400 A) in which scattered particles are bent by about 100° horizontally for $\sim$1.0 GeV/c pions from hypernuclear production by the (K^-, π^-) reaction with a 1.1 GeV/c K^- beam. Figure 8 shows the solid angle as a function of the scattered particle momentum. This system covers a momentum range of 0.7–1.1 GeV/c with more than 100 msr. The forward angles less than 2° are excluded because events in this region will be rejected in the off-line analysis due to a worse vertex resolution and thus a larger background ratio than for the other angles. With the full excitation (2.5T, 400A), the π^- solid angle for the (K^-,π^-) hypernuclear production reaction is 130 msr both for a 1.1 GeV/c K^- beam (p_{π^-} = 0.93–1.3 GeV/c) and for a 0.9 GeV/c K^- beam (p_{π^-} = 0.75–0.85 GeV/c).

The trajectory of scattered π^- is reconstructed by the Runge-Kutta method [7] based on position information measured by the drift chambers at upstream (SDC1,2) and downstream (SDC3,4) of the SKS magnet, using the magnetic field map calculated by the TOSCA code [8].

At KEK-PS, the momentum resolution of the SKS spectromter with the SKS0 setting and a similar set of detectors was 0.1–0.15% (FWHM) for 0.72 GeV pions [9, 10]. We expect a similar resolution in E63, whose effect onto the missing mass resolution is negligibly small compared to the effect of energy loss struggling in our thick target. The magnetic field is monitored with a NMR probe during the data taking to correct for the fluctuation of the actual field. The SKS pole gap is filled with helium gas contained in a bag with 16 μm-thick Mylar windows to

reduce multiple scattering effect.

4.1 Counters for particle identification

In order to identify the (K^-, π^-) reaction events from a huge amount of background events, the setup incorporates counters for particle identification. Scattered pions are particle-identified by a aerogel Čerenkov counter (SAC1) in the trigger level and by time-of-flight method in the off-line analysis.

Time-of-flight counters

TOF is a set of 30 mm-thick horizontally-segmented plastic scintillation counters. Scattered particles are identified by the time-of-flight method with a typical flight length of 5 m between BH2 and TOF. Corresponding time difference between kaon and pion is ∼1.5 ns for 1.1 GeV/c. The specification of TOF is listed in Table 6. and the time resolution was typically $\sigma = 0.2$ ns.

TOF was used in E13 for the (K^-,π^-) reaction at 1.5 GeV/c Figure 33 shows the performance of time of flight measurement in E13, where pions and kaons at ∼1.4 GeV/c were clearly separated. The separation will be further improved in the proposed experiment due to lower momenta (∼0.8 and ∼1.0 GeV/c).

Aerogel Čerenkov counters

A threshold-type aerogel Čerenkov counter (SAC1) is installed downstream of the experimental target. Figure 9 shows a schematic view of SAC1. SAC1 covers a 342 × 80 mm^2 area with a 66-mm thick silica aerogel radiator. Polytetrafluoroethylene $(CF_2)_n$ is chosen as inner diffused-type reflector. Five 2" fine-mesh type PMTs, Hamamatsu H6614-70UV, are connected to the radiator directly. The analog signals from the five PMTs are summed up before discrimination.

In E13, the refractive index of SAC1 was 1.03, corresponding to the threshold pion momentum of 0.6 GeV/c. In E63, however, the photon yield for the lowest momentum π^- entering SKS (∼0.7 GeV/c) is expected to be small for $n = 1.03$. Therefore, we will replace the radiator with the one with $n = 1.05$ (pion threshold of 0.45 GeV/c) to increase the efficiency.

4.2 Tracking detectors SDC1,2,3,4

The drift chambers SDC1 and SDC2 are placed upstream of the SKS magnet. SDC1, 2 have a drift length of 2.5 mm with a spatial resolution of less than $\sigma = 0.2$ mm. SDC1 has six layers of sense wire plane ($xx'uu'vv'$) and SDC2 has four layers of sense wire plane ($uu'xx'$), where x, u and v denote a vertical wire plane and wire planes tilted by ± 15°, respectively.

The drift chambers SDC3 and SDC4 are placed at the downstream of the SKS magnet. SDC3,4 have a drift length of 10 mm with a spatial resolution of $\sigma = 0.25$ mm. Both SDC3 and SDC4 have six layers of sense wire plane ($vxuvxu$), where x, u and v denote a vertical wire plane and a wire plane tilted by ± 30°, respectively.

The gas mixture in use is Ar:C_4H_{10}:Methylal = 76:20:4 for SDC1,2 and Ar:C_2H_6 = 50:50 for SDC3,4 at atmospheric pressure. These detectors have effective areas wide enough to cover the scattered particle profile with scattering angles of 0–20°. Specifications of SDCs are summarized in Table 7. Those drift chambers were used in all the experiments at J-PARC K1.8 (E19, E10,

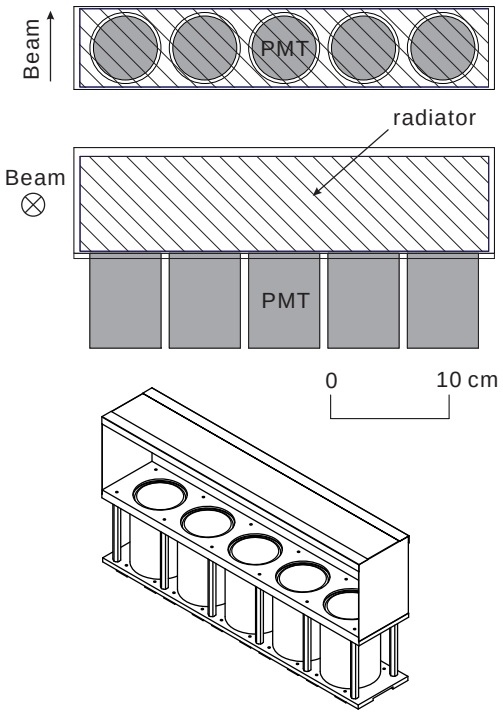

Figure 9: Schematic view of SAC1. An effective area is 342 × 80 mm^2 with a 66-mm thick silica aerogel radiator ($n = 1.05$). Five 2" fine-mesh type PMTs, Hamamatsu H6614-70UV, are connected on the radiator directly.

E27, E13, and E05) without serious problems. They will be installed at the K1.1 area after maintenance.

4.3 Beam-through veto counter

The "beam-through veto counter" system, which was successfully introduced in E13, will be employed to suppress kaon events which are misidentified as pions by SAC1. The system is placed to cover the very forward region (the beam hitting region) downstream of all the tracking detectors to reduce amount of material on the scattered particle trajectory. The system consists of a scintillator hodoscope (SFV) and an aerogel Čerenkov counter (SAC3). It suppresses, at the trigger level, beam-through kaon events and forward-scattered kaon events which slip through the SAC1 veto, while scattered pions which pass through this counter system are not vetoed by using SAC3 signal. Figure 10 shows a schematic view of the beam-through veto counter system. SFV is a segmented plastic scintillation counter with an effective area of 400 × 200 mm^2, covering the kaon beam size. SAC3 is an aerogel Čerenkov counter and distinguishes between kaons and pions using $n = 1.028$ silica aerogel with a thickness of 120 mm. The analog signals from the PMTs are summed up as for the other ACs. The K^- beam-through trigger logic is defined as SFV × $\overline{\text{SAC3}}$.

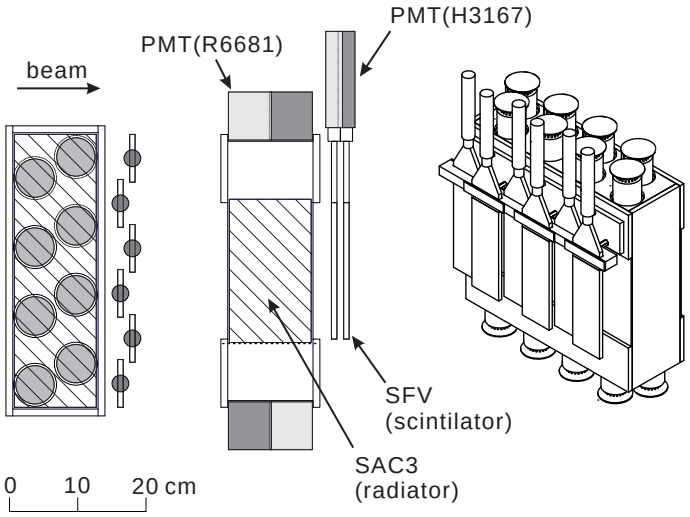

Figure 10: Schematic view of the beam-through veto counter (SFV and SAC3). SFV is a segmented plastic scintillation counter, and SAC3 is an aerogel Čerenkov counter using silica aerogel radiator ($n = 1.028$).

4.4 Beam-decay suppression detectors

Beam kaons decay in two dominant channels, $K^- \to \pi^-\pi^0$ (21%) and $K^- \to \mu^-\overline{\nu_\mu}$ (64%). When a kaon decays between BACs and SAC1, it is identified as a (K^-, π^-) event at the trigger level. Such events cause a large amount of fake triggers. In addition, those events cannot be eliminated from the missing mass spectrum as well as from the γ-ray spectrum. Figure 11 shows correlation between the momentum and the scattering angle ($\theta_{K\pi}$) for hypernuclear production and beam kaon decays at p_{K^-}=1.1 and 0.9 GeV/c. The decay events overlap with the hypernuclear production events at scattering angles of 3°–12° for 1.1 GeV/c and 6°–14° for 0.9 GeV/c. They cannot be separated kinematically.

Because the event rate for the K^- decay is much larger than that for the hypernuclear production, contamination from the decay events is a serious problem as in previous experiments using the (K^-, π^-) reaction [11, 12]. For this reason, the decay suppression counters (SP0, SMF) were introduced in E13 to suppress the background events due to the beam K^- decay.

SP0 can reject $K^- \to \pi^-\pi^0$ decay events by tagging an electromagnetic shower caused by high energy γ rays from π^0 emitted to forward directions from the target region. Figure 12 shows a schematic view of SP0. The detector consists of 8 layers of segmented plastic scintillators ($t = 8$ mm) with lead plate ($t = 4$ mm) converters in between. The number of layers and their thickness were optimized by Monte Carlo simulation. The response of the whole detector was measured in advance with $e^\pm$ and neutron beams. The effective area is 1200×1100 mm^2 with a 400×120 mm^2 hole for scattered π^- to go through. Electromagnetic showers from $\pi^0 \to 2\gamma$ hit 5 layers in average while hadronic particles from hypernuclear decay hit less than 2 layers. Therefore, $K^- \to \pi^-\pi^0$ decay events are suppressed by selecting the number of hit layers larger than 3 or 4 with a small chance of misidentification to other particles. Hypernuclear decay events emitting π^0 are also rejected by SP0. However, the loss of hypernuclear events is negligibly small due to a low branching ratio of π^0 emission channel (about 10% or less for

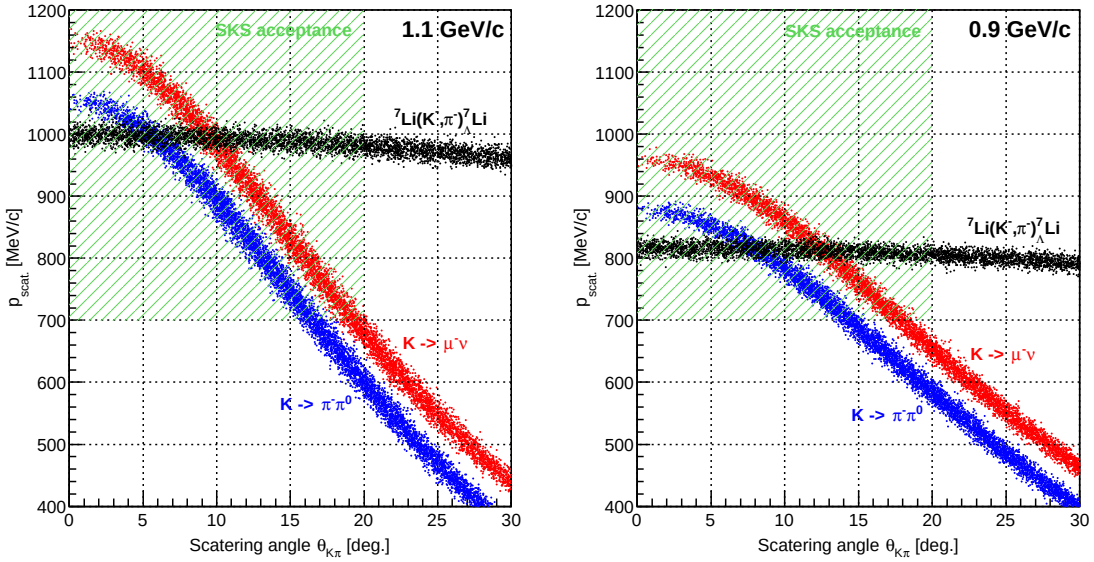

Figure 11: Correlation between $p_{scat.}$ and $\theta_{K\pi}$ for hypernuclear production events and beam kaon decay events with p_K=1.1 and 0.9 GeV/c. The acceptance coverage of the SKS spectrometer is also shown.

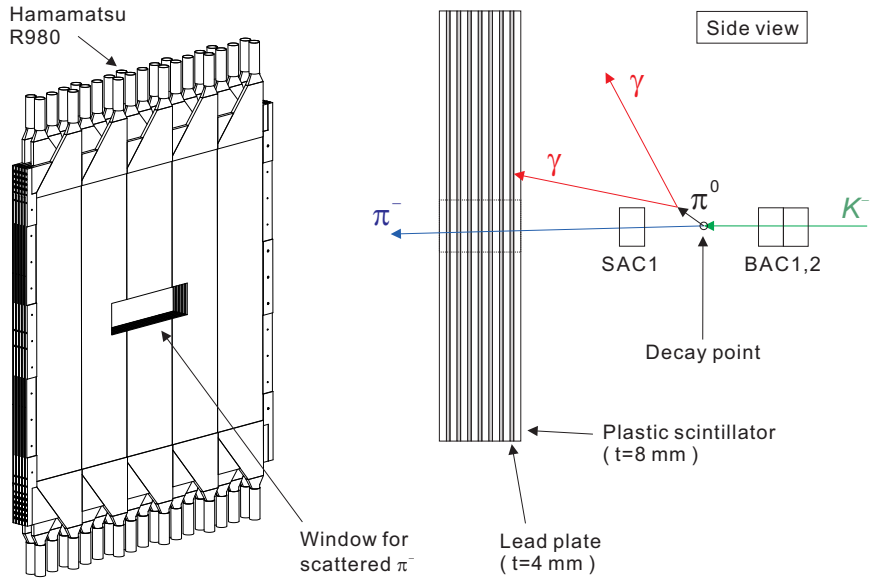

Figure 12: Schematic view of SP0. The detector consists of 8 layers of segmented plastic scintillators (t = 8 mm) with lead plates (t =4 mm) between each scintillator layer as a converter. The effective area is 1200 × 1100 mm^2 with a 400 × 120 mm^2 hole for scattered π^- to get through toward the SKS magnet.

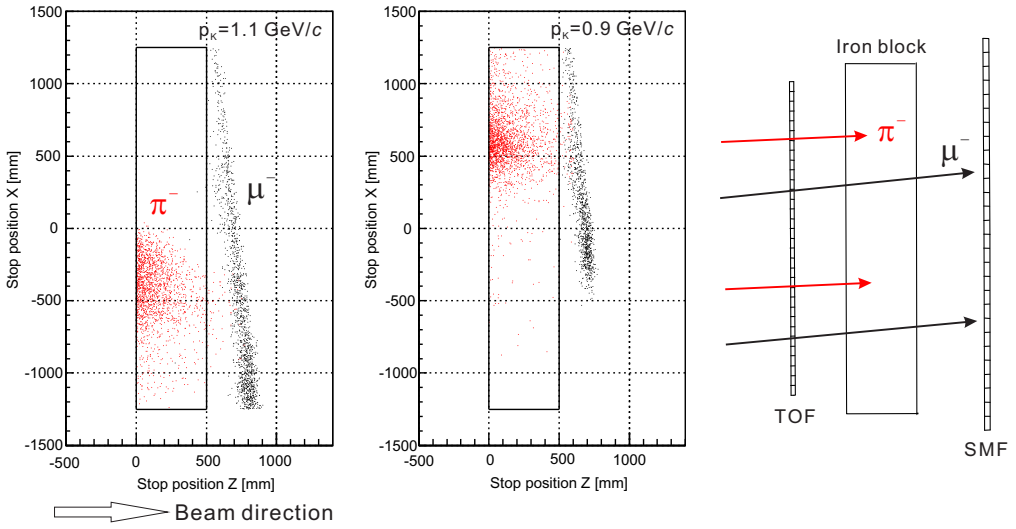

Figure 13: Simulated stopped/absorbed position in iron for μ^- from the K^- decay (black points) and π^- from the hypernuclear production (red points) for K^-momentum of 1.1 and 0.9 GeV/c. Particles are incident in +z direction, and z=0 corresponds to the iron block surface. Considering the passing-through probability for pions and muons, the optimum size of the iron block is found as the rectangular in solid line.

${}^{4}_{\Lambda}$H and ${}^{7}_{\Lambda}$Li) in hypernuclear decay and the small solid angle of SP0 seen from the target. The signal from each scintillator segment is read out by PMTs (Hamamatsu R980) and the timing information is recorded. The suppression efficiency for $K^- \to \pi^-\pi^0$ was measured in E13 to be 69% (see Section A.9).

SMF can reject $K^- \to \mu^-\overline{\nu_\mu}$ decay events by discriminating μ^- from the scattered π^- emitted in hypernuclear production reaction. SMF consists of a 50 cm-thick iron block and a lucite Čerenkov counter hodoscope (LC) behind it. All the μ^- pass through the iron block while almost all the π^- are absorbed via hadronic interactions. Therefore, the decay events are suppressed by detecting outgoing μ^- at the downstream of the iron block.

This system was successfully used in E13 but the thickness of the iron block should be reconsidered for E63. Figure 13 shows distribution for a stopped/absorbed position of the scattered π^- and μ^- in an infinite thickness of iron for 1.1 and 0.9 GeV/c K^- beam. The thickness of the iron block was determined to be 50 cm so as to optimize the μ^-/π^- separation as shown in the figure. The hodoscope (SMF LC) was also used as a Čerenkov counter to reject protons for the (π, K) reaction experiments (E19, E10, E27) at J-PARC K1.8.

It is noted that some neutrons and γ rays produced by π^- absorption in the iron block hit LC and cause overkill of π^-. In the case of E13 with K^- momentum of 1.5 GeV/c, the muon suppression efficiency was measured to be 99.5%, while the pion overkill probability was measured to be 13% for Σ^+ production events which corresponds to ∼10% for hypernuclear production events. (see Section A.9.)

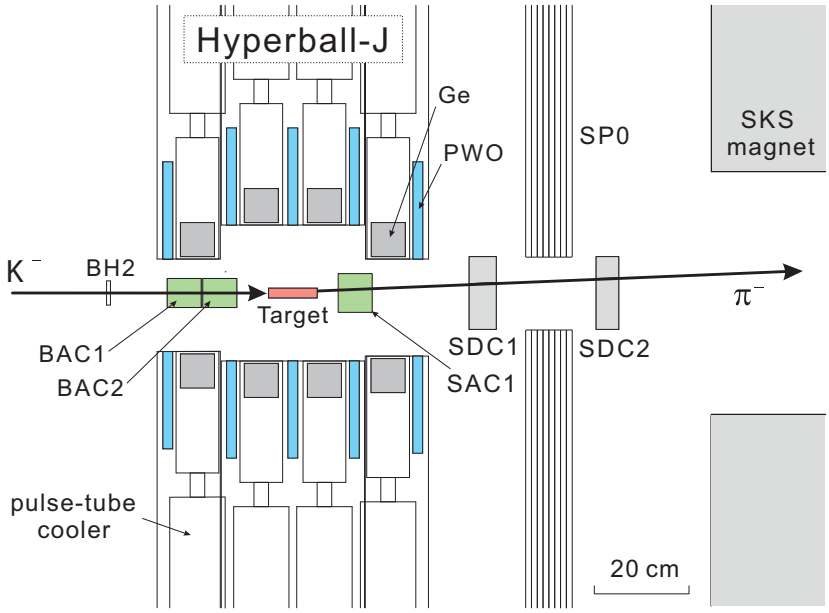

Figure 14: Experimental setup around the target and Hyperball-J (side view).

5 Hyperball-J

Hyperball-J is a Ge detector array for hypernuclear γ-ray spectroscopy developed for J-PARC experiments and successfully used in E13. The array is designed to tolerate severe radiation and high counting rate conditions with intense hadron beams, by adopting mechanical cooling of Ge detectors [13] and fast background suppression counters made of PWO scintillator. Figure 15 illustrates the lower half of Hyperball-J, and Fig. 16 shows photographs of Hyperball-J installed at K1.8 for E13.

Hyperball-J consists of 28 Ge detectors each of which has a Ge crystal of 60% efficiency relative to the ϕ =3"$\times$ ℓ = 3" NaI crystal. Each Ge crystal is mechanically cooled with a pulse-tube refrigerator [13], which decreases the crystal temperature down to 65–70 K, much lower than the temperature reached by liquid nitrogen (90–95 K), and greatly reduce serious effects of radiation damage peculiar to high-energy hadron beam experiments. This unique feature is particularly effective to reduce the systematic error from change of γ-ray peak shape due to radiation damage of Ge detectors for our $B(M1)$ measurement by Doppler shift attenuation method in E63.

Each Ge detector is surrounded by PWO scintillation counters (20 mm thick) to suppress Compton scattering events, electromagnetic shower from high energy photons, and penetrating high energy particles. Compared to commonly-used BGO scintillator, PWO has a higher density and a larger effective atomic number, and emits a light with much shorter decay time ($\sim$ 10 ns). Although the light output of PWO is much smaller than BGO, we developed PWO counter having nearly 100% efficiency for 100 keV photons by using specially doped PWO crystal with a temperature lower than 0°C.

Figure 17 shows the total photo-peak efficiency as a function of γ-ray energy for a point source and for the realistic condition considering the beam size and γ-ray absorption in the

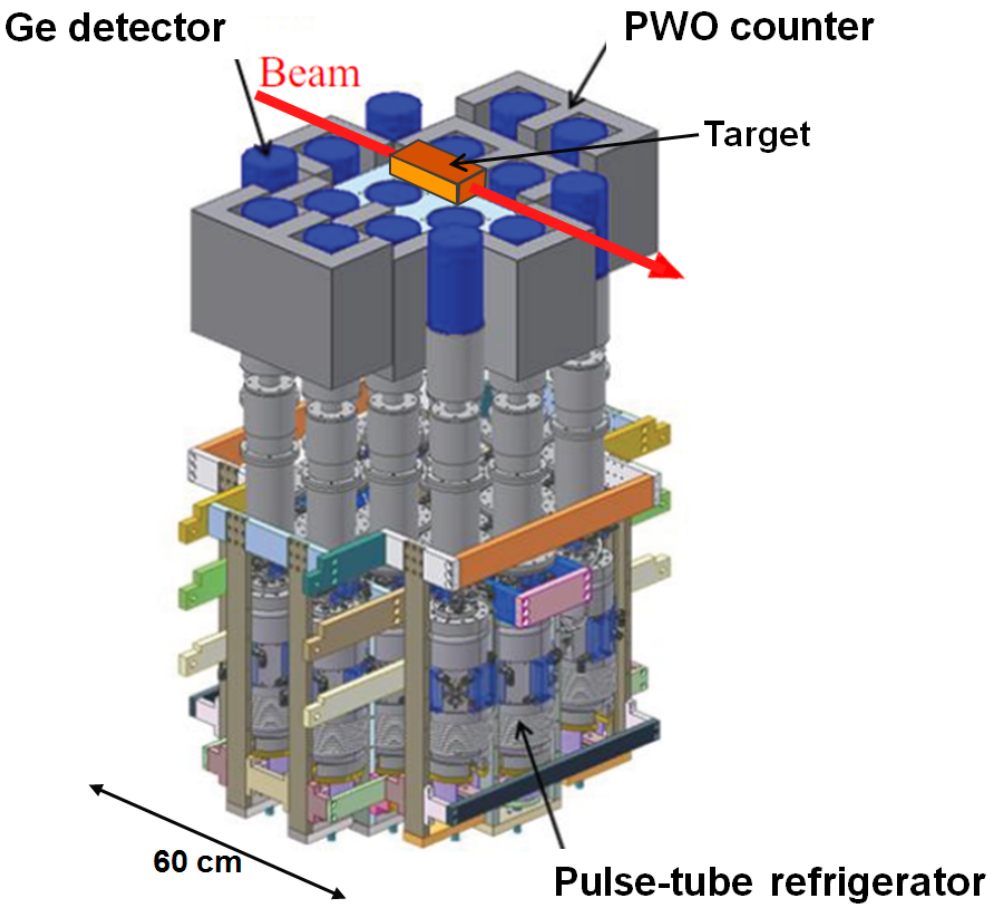

Figure 15: Schematic view of Hyperball-J (the lower half only). The array consists of Ge detectors cooled by a pulse-tube refrigerator and of PWO counters.

Li_2O target. In E13, the energy resolution for the final spectrum summed up for all the Ge detectors after energy calibration was 4.5 (FWHM) off the beam spill and 5.0 keV (FWHM) during the beam spill. Some of the Ge detector had worse resolution due to external electric noise from the power modules for the refrigerator. We are planning to change the power system to remove the noise.

There are four types of Ge + PWO detector units (B-, E-, C-, L-type) as shown in Fig. 18. Figure 19 shows the detector arrangement of Hyperball-J. In the original design, each half of Hyperball-J (the upper half and the lower half) had one set of the B-type detector unit, four sets of the E-type detector unit, two sets of the C-type detector unit and four sets of the L-type detector unit. In total, 32 Ge detectors can be mounted to the Hyperball-J frame (16 detectors for each half), but four L-type detectors at the downstream side are missing at present. The detector units are mounted to vertically movable frames, which allow for various detector arrangement.

In the E63 experiment, the detectors of Hyperball-J will be first arranged in the same configuration as in E13 so as to avoid interference between the Hyperball-J detectors and the trigger counters. Figure 14 shows a schematic side view of the detector system around the

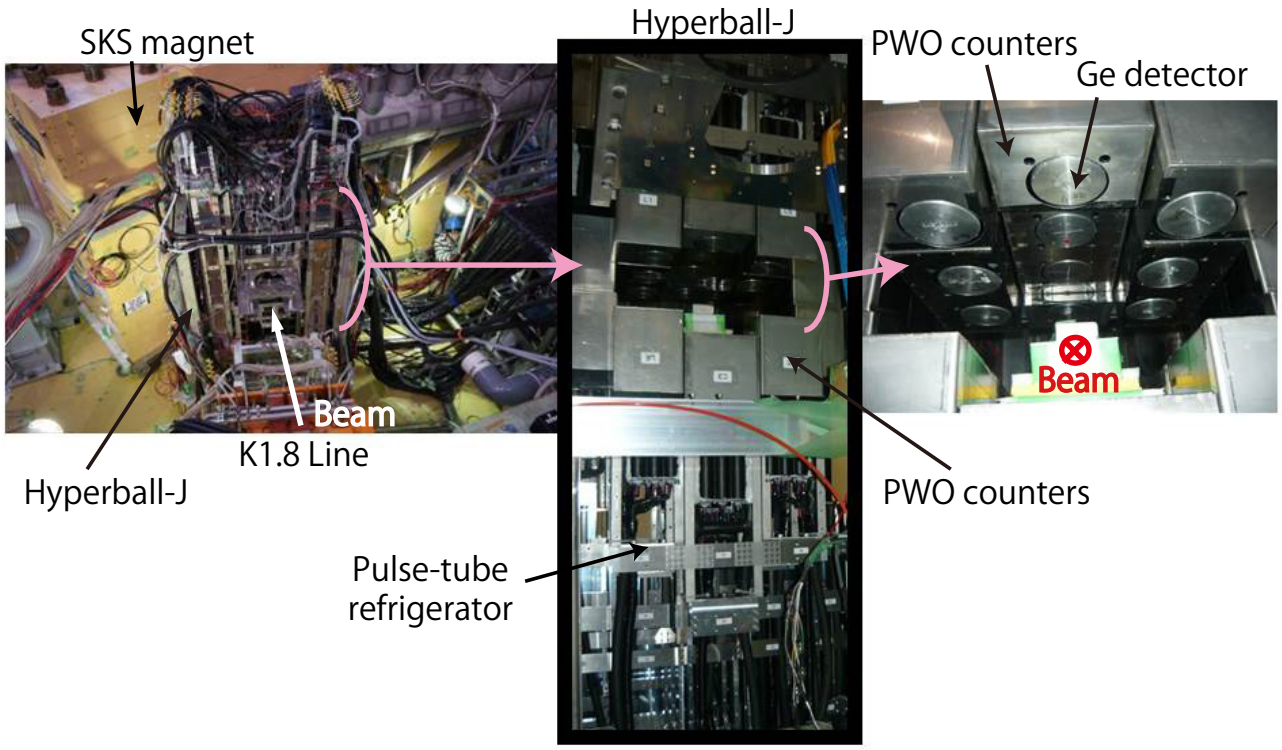

Figure 16: Photograph of Hyperball-J. Left: Hyperball-J installed in front of the SKS magnet. Center: Hyperball-J detectors with pulse-tube refrigerators viewed from upstream to downstream. Right: inner part of Hyperball-J.

experimental target. The distance between a Ge detector housed in the B-type unit and the target center is 14 cm. The Ge crystals cover a total solid angle of $0.24\times4\pi$ sr for the source point at the center.

In the ${}^{4}_{\Lambda}$H run, the efficiency of Hyperball-J can be increased by arranging each Ge detectors closer to the target, since the Doppler shift correction is not effective in the case of fragmentation production of ${}^{4}_{\Lambda}$H (see Fig. 10 in the E63 proposal [2]) and the counting rate of our Ge detectors is expected to be much lower than the operation limit. The optimum Ge detector positions will be determined in the commissioning run by actually changing the positions and measuring the live time.

5.1 Ge detectors

The Ge detectors are of coaxial type with a typical size of $\phi = 70 \times \ell = 70$ mm^3. The relative efficiency of each Ge crystal with respect to a ϕ =3" $\times$ ℓ =3" NaI(Tl) counter is ~60%. Features of the Ge detectors are listed in Table 9.

Mechanical cooling

It is reported [14] that radiation damage to Ge crystals by fast neutrons, which is serious in our experiments using high intensity hadron beams, is significantly reduced when a crystal

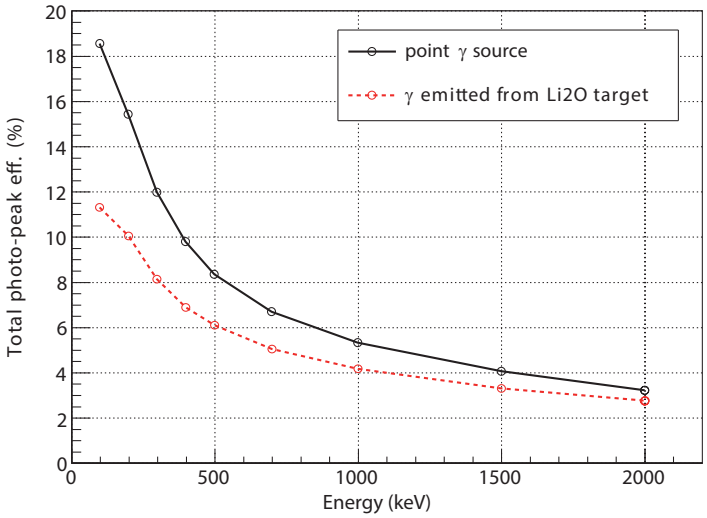

Figure 17: Simulated efficiency curve of Hyperball-J (with 28 Ge detectors) for a point source and for realistic conditions with a source point distribution and absorption in the Li_2O target taken into account.

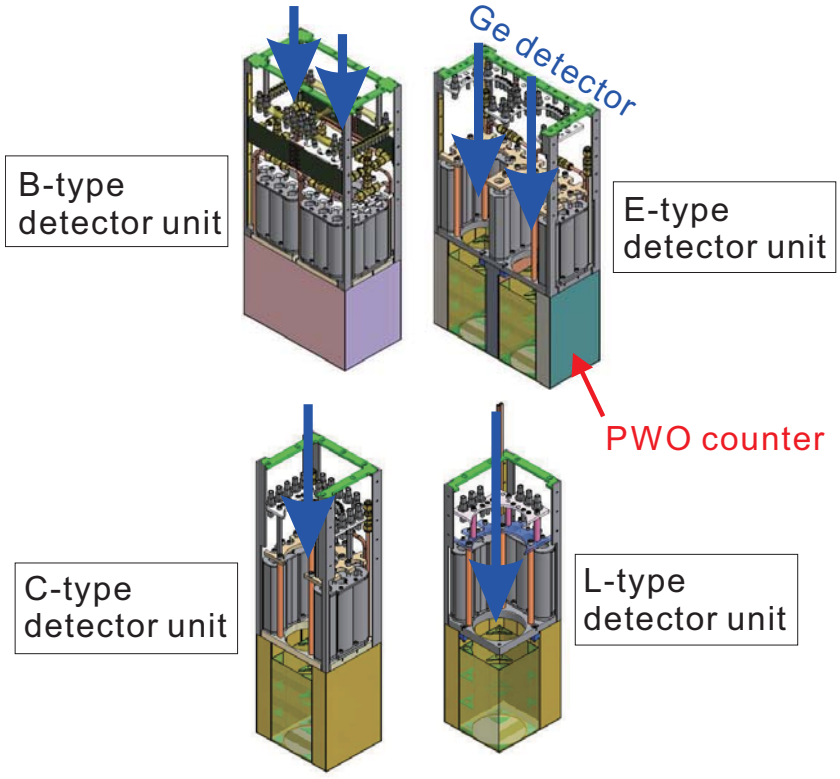

Figure 18: The Ge + PWO detector units for Hyperball-J (for the upper half).

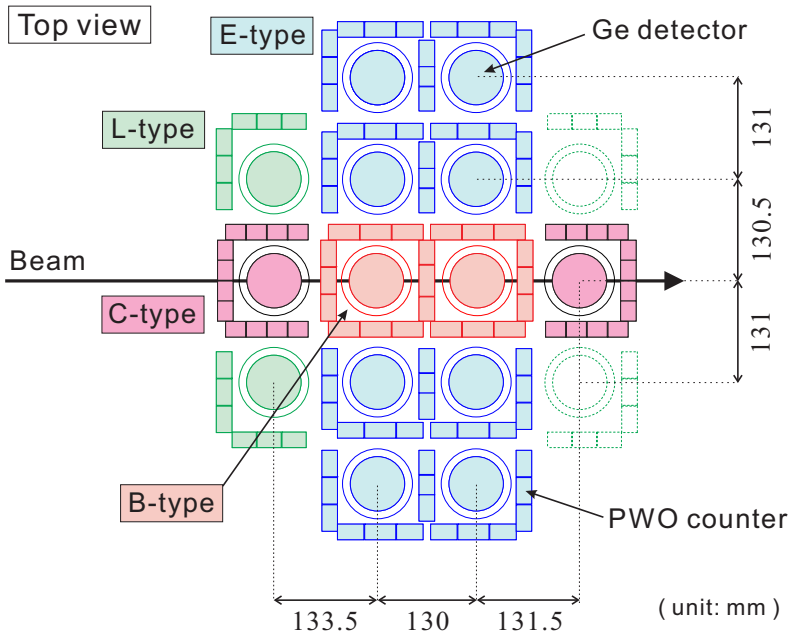

Figure 19: Schematic view of the Hyperball-J detector configuration.

Table 9: Specifications of the Ge detectors.

Crystal	N-type (closed end shape)
Preamplifier	transistor-reset type
Detector gain	50 mV/MeV
Reset energy	∼120 MeV/reset
Crystal size	$\phi = 70 \times \ell = 70$ mm^3 (250 cm^3 in volume)
Relative efficiency	60%
Window in front of the crystal	Al ($t = 1$ mm)
Cooling method	mechanical cooling with a pulse-tube refrigerator
Crystal temperature	73 K (typical)
Thermometer	Pt100

temperature is kept below 80 K, much lower than the conventional liquid nitrogen (LN_2) cooling case (∼90-95 K). In the Ge detectors for Hyperball-J, we developed a mechanical cooling method [13] instead of the LN_2 cooling and succeeded in cooling down the Ge crystals below 70K.

Figure 20 shows a schematic view of the Ge detector unit developed by our group. A pulse-tube refrigerator (PTR) manufactured by Fuji Electric Co. Ltd. is coupled to the Ge crystal. Water cooling of the PTR compressor increases its cooling power. We have succeeded in cooling the crystal down to ∼70 K, which is sufficient for our purpose. Usually, mechanical cooling methods produce microphonic noise and deteriorate energy resolution of Ge detectors. In our case, the Ge sensor-cooler unit has comparable energy resolution with that of the LN_2 cooling. thanks to small mechanical vibration of PTR. Furthermore, without a LN_2 Dewar,

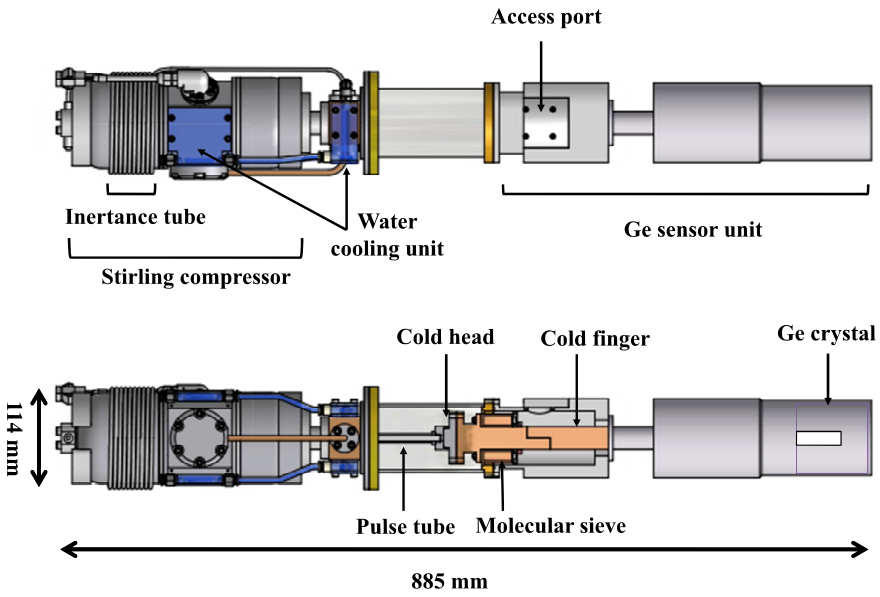

Figure 20: Schematic view of the mechanically-cooled Ge detector. A pulse-tube refrigerator (PTR) is coupled to each Ge crystal. Water cooling of PTR increases its cooling power.

dense placement and adjustable geometrical arrangement of the Ge detectors have become possible.

A thermocouple thermometer (Pt100) is placed close to the Ge crystal to monitor the temperature. In E13, we found that the crystal temperature changes by $\sim$1 K at maximum in a day due to changes of the room temperature the PTR operation power. Such a phenomenon does not occur in conventional LN_2-cooled Ge detectors because boiling LN_2 always keeps the crystal temperature constant. The observed crystal temperature change causes a gain drift of the Ge detector significantly, which was measured to be 0.3 keV (at 1.3 MeV) per 1 K in our detector [15]. The PTR power should be controlled with the temperature data, but we cannot do it because the PTR power supply needs to work at the maximum power to achieve 70K. Therefore, we decided to measure the Ge detector gain using various γ-ray sources at least every one hour during the beam time with the method described in Section 5.3 and in Section B.2.

Before mounting the Ge detectors, each of them needs to be pumped and backed for cleaning the Ge crystal and inside of the cryostat. The vacuum and cleanness are monitored during the beam time via the temperature as well as the preamplifier reset rate sensitive to the dark current on the crystal surface. In E13, the temperature rapidly increased for two detectors out of 23 after about one-month use and they cannot be operated after that. It may be due to vacuum deterioration caused by insufficient cleaning after fabrication of the cryostat vessel. Such problems will be sloved by cleaning the detectors for a sufficiently long time. By using a pumping station we prepared at our room in IQBRC, ten Ge detectors are able to be pumped and baked simultaneously. In this room, we also have a clean circumstance for handling inside of the Ge detector cryostal; we can repair the Ge detectors by ourselves in case an FET or a reset-transitors in the detector cryostat is broken down.

Reset-type preamplifier

In a typical condition of our hypernuclear γ-ray spectroscopy, the total energy deposit rate is more than 0.1 TeV/s for each Ge detector. In such a condition, output signals of conventional resistive-feedback type preamplifiers always saturate and cannot work at all. Thus the Ge detector in Hyperball-J is equipped with a transistor-reset type preamplifier.

In our experiment high energy particles in the beam halo and scattered beams off the target frequently pass through the Ge detectors. The energy deposit from a charged particle penetrating the Ge crystal is $\sim$70 MeV, extremely larger than that from a nuclear γ ray (typically 0–3 MeV). The counting rate for high energy charged particles is more than 10 kHz per detector in a typical experimental condition.

The transistor-reset type preamplifier resets their output signal voltage to the base line level by discharging the feedback capacitor when the output voltage exceeds the operational limit (typically $\sim$10 V). Usually, preamplifiers are designed so that this limit voltage corresponds to an accumulated energy deposit of $\sim$30–50 MeV. In order to reduce the dead time associated with the reset, we shifted up the reset energy to $\sim$120 MeV by increasing the feedback capacitance to reduce the preamplifier gain. With our shaping amplifier (ORTEC 973U), a dead time of $\sim$30 μs appears after each reset due to overload in differentiation of a steeply dropping reset signal ($\sim$10 V/5 μs). It gives about 30% dead time for a reset rate of 10 kHz, the highest rate we experienced in KEK E419, R518, E566 using 1 MHz pion beams irradiated on a 20g/cm^2-thick experimental target.

In E63 as well as E13, the beam intensity (of kaons and pions) is less than 5×10^5/spill (0.25 MHz) and the expected reset dead time is less than 7.5%.

Readout electronics

The readout electronics connected to the preamplifier are also specialized for the high counting and large energy deposit rate conditions. Figure 21 shows a block diagram of the readout circuit for a Ge detector. The Ultra-High-rate Amplifier (UHA, ORTEC 973U, integration time = 3 μs) is used as a main amplifier for analyzing the γ ray energy. In UHA, the output signal from the preamplifier is processed by a special shaper circuit with $\sim$0.5 μs shaping time and then integrated by a gated integrator circuit with a 3-μs integration time. Therefore, the dead time of the amplifier due to signal pile-up is 6 μs. The module also incorporates a fast shaper/discriminator circuit and outputs a Count-Rate-Monitor (CRM) TTL logic signal, which we use for a Ge detector self-trigger. The output analog signal from UHA is digitized by a peak-sensitive ADC with a 13 bit resolution (ORTEC AD413A).

For the timing information, the preamplifier output signal is processed through a fast shaping amplifier (Timing Filter Amplifier (TFA), ORTEC 579, differentiation/integration time = 100/100 ns), and a constant fraction discriminator (CFD, ORTEC 934). The timing information is digitized by a multi-hit TDC (Notice TDC64M).

The digitized data from the ADC modules are sent to a FERA driver module via FERA bus and then to a VME memory model called Universal MEMory module (UMEM). The data stored in UMEM and the multi-hit TDCs are transferred to a host computer via VME bus.

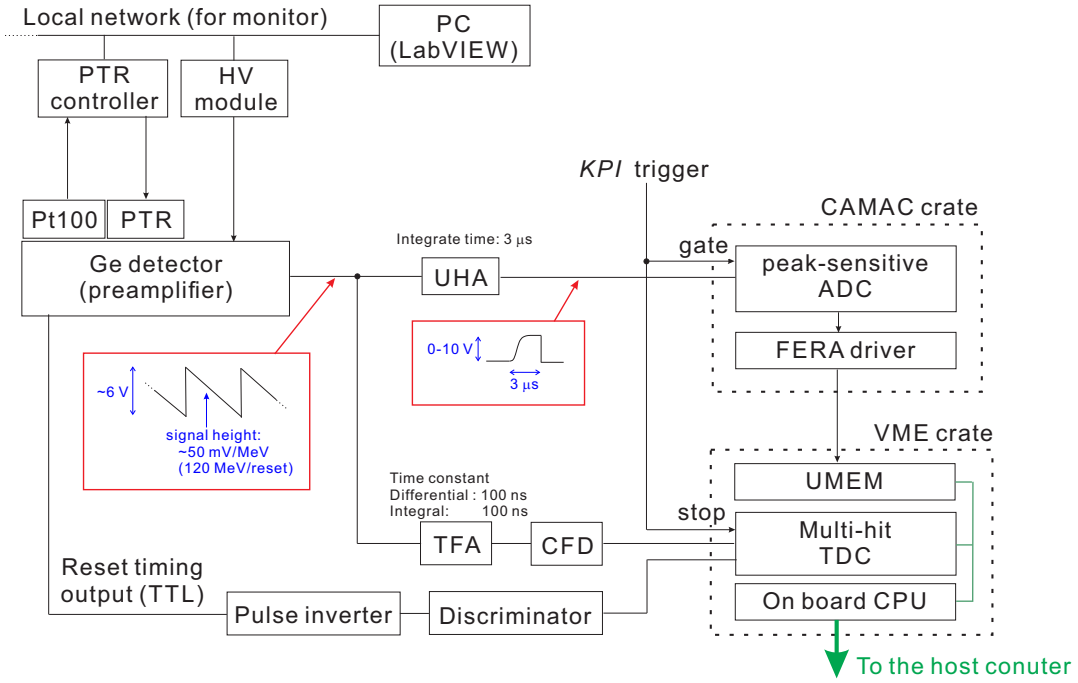

Figure 21: Block diagram for the Ge detector read-out and the control system.

Control system

We have also developed a Hyperball-J control system [15] based on the network communication (TCP/IP protocol) and the GUI programming language, LabVIEW. This system is capable of remote control of the Hyperball-J components including the bias HV of the Ge detectors and the pulse-tube refrigerator power. It also constantly monitors the crystal temperature of each Ge detector. Bias shutdown function is incorporated into the control system for protecting the Ge detector from high leakage currents when the crystal temperature goes up.

5.2 PWO counters

All of the Ge detectors are surrounded by PWO scintillation counters to suppress background events such as Compton scattering, high-energy γ rays from π^0 decay and high energy charged particles passing through the Ge crystal. Instead of conventional BGO scintillators usually used for such Ge detector arrays, we adopted PWO having a much shorter decay constant than BGO together with a larger density (8.28 g/cm^3) and a larger effective atomic number. In our experience with the previous Ge detector arrays with BGO counters (Hyperball and Hyperball2) used at KEK-PS and BNL-AGS, over suppression due to the long decay constant of BGO scintillator was a serious problem in high counting rate conditions. However, PWO was not used for such a purpose due to a much smaller light yield of PWO resulting in a less detection efficiency for low-energy γ rays. We increased the light yield about four times by doping a rare-earth element and by cooling the PWO crystal to $\sim$0 C°. In order to cool down

the PWO crystal, copper plates cooled by circulating coolant were made contact to the PWO crystals. In E13, at a room temperature more than 30C°, the crystal temperature was kept around 10–13 C°, below which the PWO casing started dewing even in an air-conditioned tent housing of Hyperball-J.

The configurations of the Ge + PWO detector unit are illustrated in Fig.22. Each Ge detector is surrounded by 6–12 pieces of the PWO scintillator with dimensions of 20 mm thick, 200 mm long, and 25–40 mm wide. In the B-type detector units, all the four sides of the Ge detector are covered with 12 pieces of PWO scintillator, while three sides are covered for the C-type and E-type units, and two sides for the L-type units as shown in Fig. 22. PMT's (ϕ 1-1/8", Hamamatsu H7416MO) are connected to the PWO crystal via silicon grease. Three PMT's are used for each side, except for the middle wall in the type B and E with two PMT's each.

In E13, the PWO counters were also found to have a sufficient background suppression capability. The continuum background was suppressed to 1/3 for 1–2 MeV as shown in Ref. 23. The performance of Hyperball-J in E13 is described in Section B.1.2.

5.3 LSO pulser

When Ge detectors are used under a high energy deposit rate, we need to monitor the dead time due to the preamplifier reset and the pile-up of signals and the energy resolution (and the peak shape) of the Ge detector during the beam time. In addition, the detector gain should be frequently measured because of a possible large gain drift for our PTR-cooled Ge detectors. In order to facilitate the monitoring, a Lu_2SiO_5 (LSO) scintillator ("LSO pulser") is installed close to each Ge detector and used as a triggerable calibration source. The LSO crystal contains

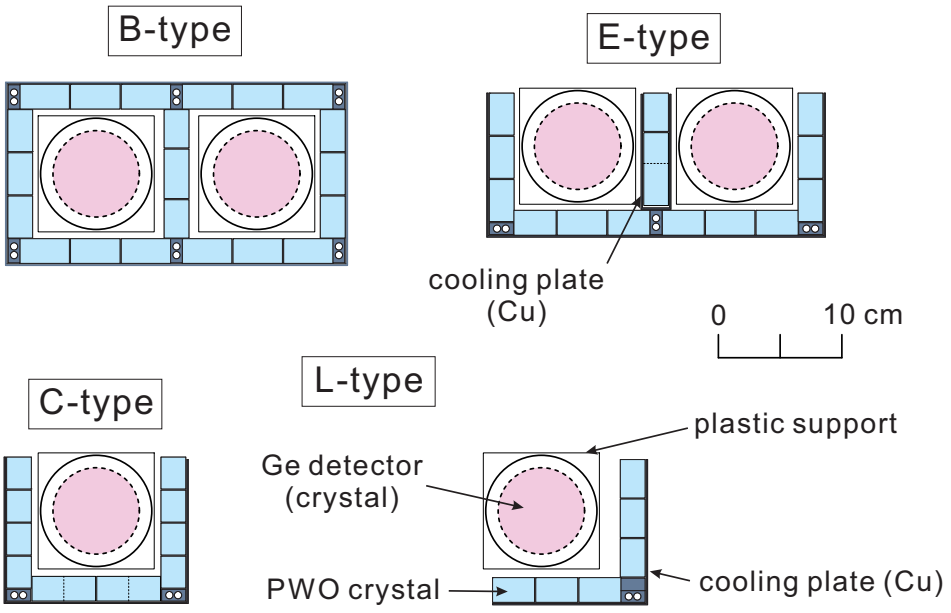

Figure 22: Configurations of Ge + PWO detector units.

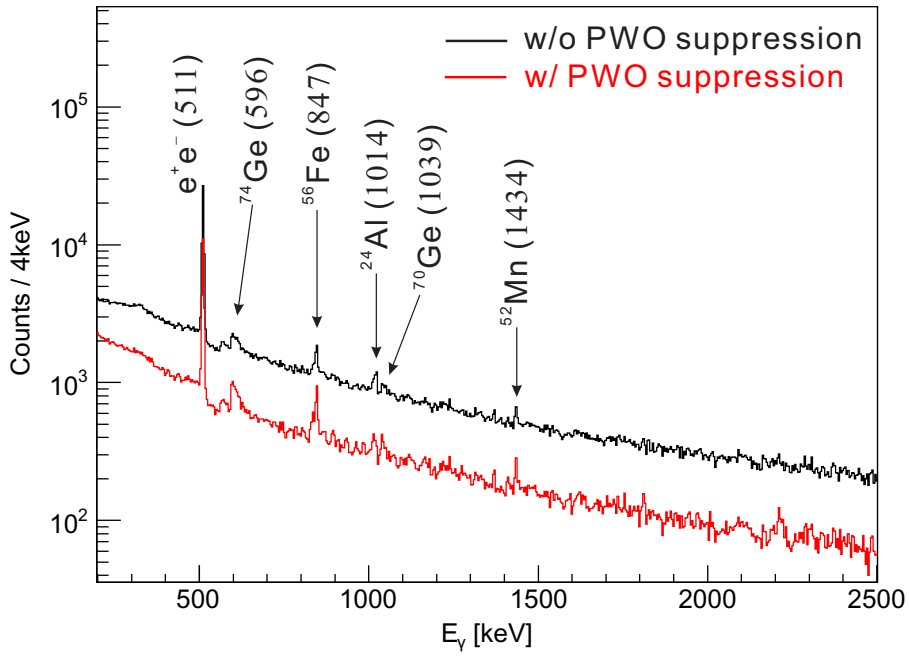

Figure 23: Performance of the PWO counters. Shown are the γ-ray spectra measured by Hyperball-J without event selection in the E13 beam time, (black) without and (read) with background suppression using PWO counters.

^{176}Lu, with a natural abundance of 2.6%, which has a half lifetime of 3.76×10^{10} y and emits 202 keV and 307 keV γ rays immediately after a beta decay. The beta ray produces a timing signal for the γ-ray emissions in the LSO scintillator. Through β-γ coincidence measurement between the LSO pulser and the corresponding Ge detector, we can discern γ rays from ^{176}Lu efficiently even under a huge background radiation during the beam spill period. Data taken both during the beam spill and off the beam spill are used to monitor the performance of the Ge detectors over the beam time. These data are collected with a stand-alone data acquisition system independent of the main DAQ system (HD-DAQ).

A LSO crystal of ϕ10 mm $\times$1 mm is connected to a PMT, Hamamatsu H3164-10. The decay rate of ^{176}Lu in this crystal is of the order of 100 Bq. In E13, a typical counting rate of the 202 keV and 307 keV γ ray peaks in a Ge detector was $\sim$1 Hz. With the LSO pulser system, the in-beam live time of the Ge detectors, which is the ratio of the ^{176}Lu γ-ray yields between the on-beam-spill and the off-beam-spill periods, was successfully measured through the whole beam time. It was typically 96% in E13.

6 Trigger and data acquisition system

6.1 Trigger

To select true (K^-,π^-) reaction events from a large amount of background such as (K^-,K^-) and (π^-,π^-) events, the trigger system is constructed as described in the following. Figure

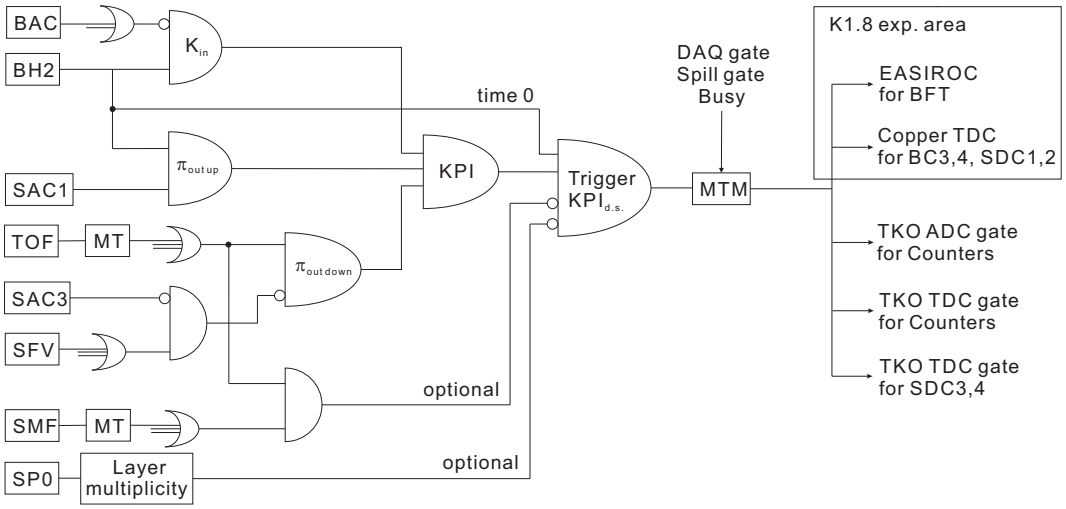

Figure 24: Trigger logic diagram for the (K^-, π^-) reaction.

24 shows the trigger logic diagram for the (K^-, π^-) reaction. In the trigger level, beam kaons ($K_{\rm in}$) and scattered pions ($\pi_{\rm out}$) are defined as

$$\begin{aligned} K_{\rm in} &= {\rm BH2} \times \overline{\rm BAC1} \times \overline{\rm BAC2} \\ \pi_{\rm out\ upstream} &= {\rm BH2} \times {\rm SAC1} \\ \pi_{\rm out\ downstream} &= {\rm TOF} \times \overline{({\rm SFV} \times \overline{\rm SAC3})}. \end{aligned}$$

The pion contamination in the kaon beam is rejected by taking an anti-coincidence of BACs and BH2. According to our experience in E13, BH1 does not join the trigger due to an extremely high single rate caused by scattered particles off the mass slit. The scattered pion is selected by taking a coincidence of SAC1 and BH2. Kaons which are misidentified as pions by SAC1 are partly rejected by the beam-through veto counter (SFV and SAC3). Scattered pions are discriminated by use of SAC3 and are not rejected.

The (K^-, π^-) reaction trigger (KPI) is defined as

$$KPI = K_{\rm in} \times \pi_{\rm out\ upstream} \times \pi_{\rm out\ downstream}.$$

SP0 and SMF may be included in the trigger in order to reduce the beam K^- decay events. Decay suppressed trigger $KPI_{\rm d.s.}$ is defined as

$$KPI_{\rm d.s.} = KPI \times \overline{{\rm SP0}_{\rm multiplicity}} \times \overline{\rm TOF \times SMF}.$$

The remaining contamination is removed in the off-line analysis based on the time-of-flight in BH1–BH2 and BH2–TOF and the momentum measured by SKS. For monitoring of the detector performance, data were also taken by the prescaled "BH2 only" trigger during the data taking period.

6.2 Data acquisition system

Figure 25 shows a block diagram of the data acquisition system. The network-based data-taking system (HD-DAQ) [16] used at K1.8 for E13 will be also used for E63. Previously the

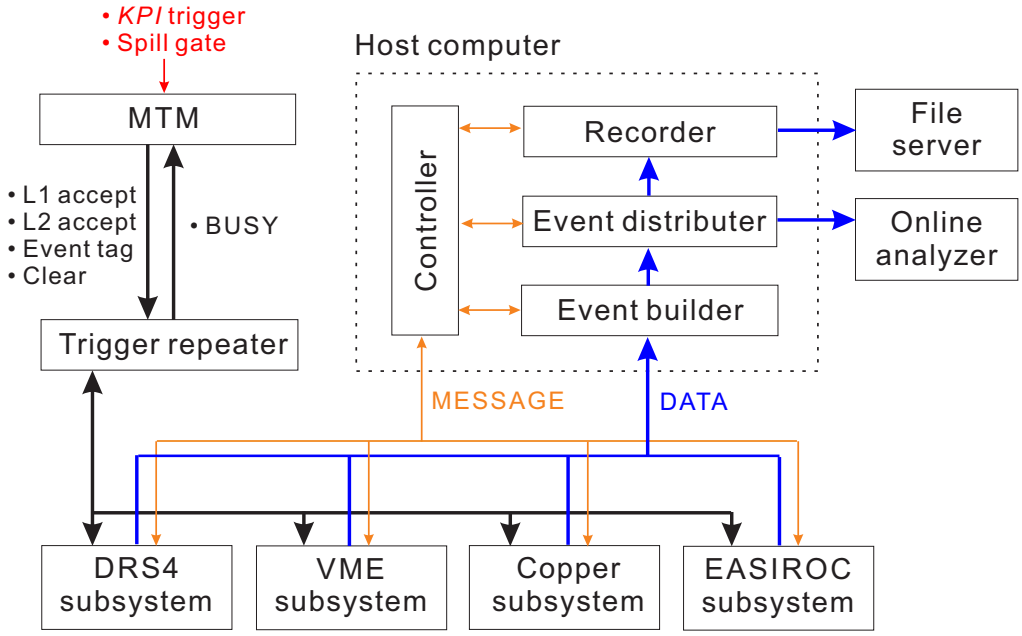

Figure 25: Block diagram of the data acquisition system.

TKO subsystem [5] was used for drift chamber TDCs and counter ADCs/TDCs, but in E63 the TKO TDC and ADC modules will be replaced by faster VME modules to improve the DAQ efficiency, while the other parts of the DAQ system will be unchanged.

The timing signals of SDC3,4 are digitized by VME multihit TDC modules (Notice TDC64M) with 1 ns resolution, while the timing signals of the trigger counters are digitized by VME high-resolution TDC modules (CAEN775 or others) with ∼35 ps resolution. The timing information of BFT is digitized by EASIROC (Extended Analogue Silicon PM Integrated Read-Out Chip) modules [17] which we recently developed for MPPC readout. The pulse height information of the trigger counters are digitized by newly-developed DRS4QDC modules.

The timing information of BC3,4 and SDC1,2 is digitized by the multi-hit TDC installed in the COPPER modules [18]. The BFT, BC3,4 and SDC1,2 data on the EASIROC and the COPPER modules are transferred to the server computers and then to the host computer. The data-acquisition cycle is processed event by event. The scalar counts of the trigger counters are recorded by VME scaler modules and transferred at the end of the spill.

The network-based data-taking system employs a DAQ software using TCP/IP protocol and a trigger/tag distribution system. For building up an event by combining data sets coming from different modules, the Master Trigger Module (MTM) distributes the event and spill numbers to a Receiver Module (RM) in each node. These numbers are transported together with digitized raw data to the host computer. MTM also manages busy signals for all the nodes. The data transferred from each module to the host computer are processed at first by the Event builder. Then they are transferred to the Event distributer and to the file server as well as to the on-line analyzer. A typical data size for one event is 2.8 kB. In E13, the data-taking efficiency was 70% for the (K^-, π^-) reaction with a trigger rate of 1.7×10^3/spill (∼800 Hz). In E63 it will be

significantly improved by replacing the TKO ADCs and TDCs into the faster TDC and ADC modules as described before.

6.3 Self-trigger data for Ge detectors

Self-triggered data for calibration and monitoring of the Ge detectors will be taken in the beam-spill period and off the beam-spill period. Figure 26 shows a block diagram of the self-triggered data system.

Ge self trigger (off-beam-spill)

The Ge self-triggered data are taken off the beam-spill period (∼4 s), which are used for a correction of Ge detector gain drift. In general, Ge detector gain depends on the crystal temperature. With the mechanical cooling of Ge detectors, the cooling power and consequently the crystal temperature is affected by a change of the room temperature and the cryostat vacuum. Thus the gain of the detector significantly changed during the beam time in our experience of E13. The trigger for the off-beam-spill data is made with the CRM signals from the 973U modules. For energy calibration using the self-triggered data, we use γ-ray peaks

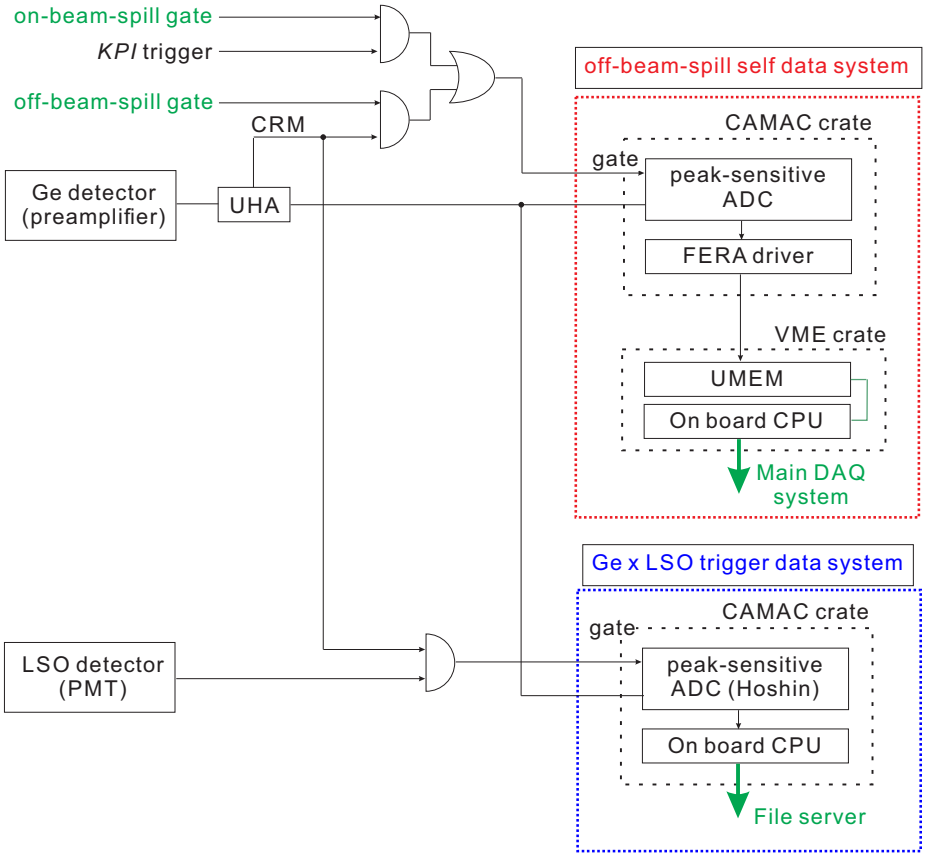

Figure 26: Block diagram of the self-triggered data system.

from excited nuclei produced by delayed β decays (lifetime longer than the order of 1 s) of unstable nuclei made by the beam, as well as daughter nuclei of the natural thorium decays. A bundle of thorium dioxide tungsten (2% ThO_2) sticks (ϕ10 mm$\times\ell$ = 60 mm) which emits 0.5–2.6 MeV γ rays is installed near the Ge detector as a reference γ-ray source. A bundle of ThO_2-W sticks weighs $\sim$40 g and is wrapped with a 1 mm-thick lead sheet to shield unwanted low energy ($<$200 keV) γ rays. The single rate of the Ge detectors increase by about 150 Hz with the ThO_2-W sticks placed near the Ge detectors.

Ge$\times$LSO trigger (on- and off-beam-spill)

The Ge$\times$LSO trigger data will be also taken in both on-beam-spill and off-beam-spill periods in order to monitor the live time of the Ge detectors by comparing peak counts of 202 keV and 307 keV γ ray peaks between the on-beam-spill and off-beam-spill period. The trigger is made from a Ge CRM signal coincident with a corresponding LSO signal. The energy data of the Ge detector is digitized by a CAMAC peak-sensitive ADC module, and the TDC data between a Ge detector and a LSO detector is also recorded. These data are transported to the file server by the on-board CPU module.

7 Target

In the ${}^{4}_{\Lambda}$H experiment, we use a 99%-enriched ^{7}Li metal target with dimensions of 4 cm $\times$ 4 cm $\times$ 26 cm. The thickness corresponds to 15 g/cm^3 for ^{7}Li. It is tightly enclosed in a laminated mylar bag filled with argon. The same type of ^{7}Li target was successfully made in a company and used for KEK-PS E419 (the first hypernuclear γ spectroscopy experiment by our group). Since the γ ray of interest has an energy of 1.1 MeV, the effect of γ ray absorption in the target is negligibly small and we do not need to carefully optimize the horizontal and vertical target size according to the beam size.

In the ${}^{7}_{\Lambda}$Li $B(M1)$ experiment, we will use single crystal Li_2O grains (ρ =2.01 g/cm^3) made of with natural lithium. Since the range of recoiling hypernuclei is of the order of a few μm. the target density should be uniform in the scale from $\sim$0.1 μm up to $\sim$0.1 mm to apply Doppler shift attenuation method. Li_2O is commercially availabe as fine power, but a sintered block made from fine power cannot be used due to inhomogenious density. To meet our requirement, single crystal grains with a size larger than $\sim$0.3 mm is necessary; a simulation showed that the effect of grain surface to the lifetime determination is less than 1% for a 0.3 mm grain. A large-size single crystal up to $\sim$5 mm can be produced by a special technique [19]. We will produce single crystal Li_2O grains of $\sim$1 mm size and contain them in a thin container of about 4 cm $\times$ 4 cm $\times$ 15 cm, with a Li_2O thickness of 10 cm (8.7 g/cm^2 for ^{7}Li). The taget will be packed in argon atomospere so as to avoid moisture absorption. The horizontal and vertical size of the target ontainer will be optimized using the beam profile data taken in the 1st running period at the K1.1 beam line.

8 Readiness and Schedule

The upstream part of the K1.1 beam line (K1.1BR) has been used for many test experiments and E36, while the downstream part of K1.1 should be constructed. The SKS magnet has been already moved from the K1.8 area to the K1.1 area, but the power supply and the refrigeration equipment including compressors should be installed and connected to the SKS magnet. In addition, the K1.1 experimental area (shieldings, power lines, etc.) as well as the counting room needs to be prepared. Detailed design for the K1.1 area construction is in progress by KEK staff.

Most of the detectors (BH1, BC3, BC4, BH2, BAC1, BAC2, SDC1, SDC2, SDC3, SDC4, SFV, SP0, TOF, SMF) are ready; they were once used at K1.8 and will be tested and installed again at the K1.1 area. We need to fabricate or modify some of the beam line trigger counters (BFT, SAC1, SAC3), of which cost and manpower are small. New support frames for BH1, BFT and BC3-4 will be fabricated, while the other detector frames used for E13 will be reused. We are also planning to repair broken wires in SDC3 and SDC4, which will take a half year but almost no cost. The total cost including additional electronics and HV modules will be around 20M yen, which will be covered mainly by the spokesperson's Grant-in-Aid. We can start installation of all the detectors for the beam/SKS spectrometers just after the K1.1 beam line construction is finished.

As for Hyperball-J, the power modules for the Ge detector refrigerators will be upgraded in 2016 so as to further reduce noise from power lines and improve the energy resolution. Then, Hyperball-J will be employed for the E03 experiment (Ξ-atomic X-rays) at K1.8 [20], which will most probably run in 2017. After E03, we need to perform Ge detector maintenance (evacuate, and anneal if necessary, all the Ge detectors) at our room in IQBRC and mount them to the Hyperball-J frame at the K1.1 area. It will take 3 months with almost no cost. So we hope to run at least 3 months after E03 is finished.

Appendix

Performance of the apparatus in the previous experiment (E13)

This appendix is a slightly modified copy of the chapter 3 and 4 of Yamamoto's doctoral thesis [21] describing details of data analysis for the E13 run with ^{4}He target [1].

The E13 experiment was successfully carried out in April and June in 2015. The setup of the proposing E63 experiment is almost the same as that of E13, except for the beam spectrometer magnets and the beam momentum, the target, and the SKS magnet setting. Therefore, most of the description in this Appendix on the detector performance and the analysis procedure in E13 also applies to E63.

A Magnetic spectrometers

In this Appendix, the performance of the magnetic spectrometers is described.

Employing the K1.8 spectrometer and the SKS spectrometer, the hypernuclear production events were identified by tagging true (K^-, π^-) reaction events from particle identification and calculating the mass of a produced hypernucleus ($M_{\rm HY}$) as a missing mass for the ^{4}He$(K^-, \pi^-)X$ kinematics. The mass is calculated by the following equation in the laboratory frame

$$M_{\rm HY} = \sqrt{(E_K + M_{\rm target} - E_\pi)^2 - (p_K^2 + p_\pi^2 - 2p_K p_\pi \cos\theta_{K\pi})},$$

where E_K and p_K are the energy and the momentum of the beam K^-. Similarly, E_π and p_π are those of the scattered π^-. $M_{\rm target}$ is the mass of the target nucleus (^{4}He), and $\theta_{K\pi}$ is the angle between the measured momentum vector of the K^- and that of the π^-. True ^{4}He(K^-, π^-) events were also selected with the reaction vertex point information.

The off-line analysis procedure of the (K^-, π^-) reaction for data from the magnetic spectrometers is listed below:

- particle identification with the time-of-flight counters,
- local tracking of the drift chambers,
- momentum reconstruction for beam K^-,
- momentum reconstruction of scattered π^-,
- reaction vertex and scattering angle ($\theta_{K\pi}$) reconstruction,
- calculation of missing mass,
- calculation of velocity of a produced hypernucleus and reconstruction of its momentum vector.

The analysis procedure is illustrated in Fig. 27.

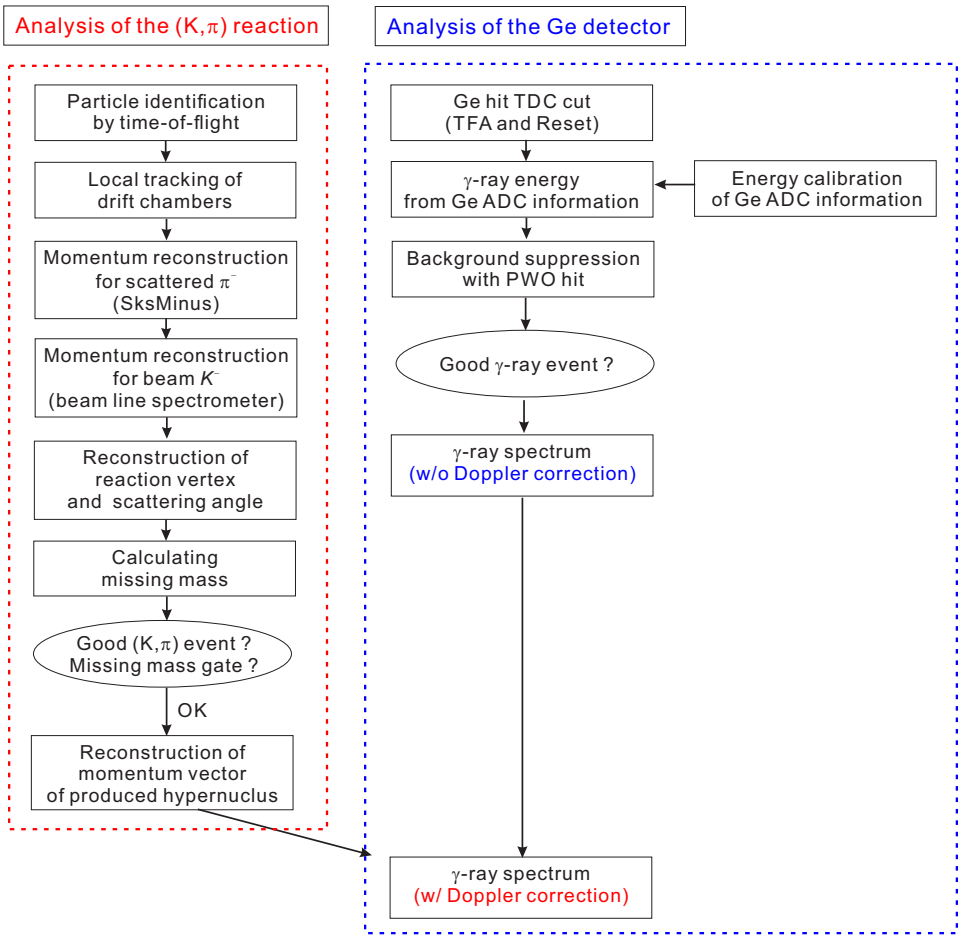

Figure 27: The analysis procedure for the obtained data.

A.1 Analysis of incident particle

A.1.1 Momentum reconstruction for beam particle

The momentum of the beam particle was reconstructed from the data of the fiber scintillation counter (BFT, installed at the upstream of QQDQQ magnets) and the drift chambers (BC3,4, installed at the downstream of the magnets), using the third-order transport matrix for the beam line spectrometer.

A clustering analysis of BFT provides a horizontal position of beam kaon trajectory at the upstream of QQDQQ magnets. Figure 28 shows a time distribution and a hit profile of BFT for beam K^- mesons. Events with a single cluster hit within a time gate of ± 5 ns was accepted. BFT made the time gate much shorter that that for previously used MWPCs ($\sim$100 ns) [22]. The yield loss after the BFT analysis was $\sim$7%, which came from a shortage of the effective area and the multiplicity cut. A local straight track was reconstructed from measured positions in BC3 and BC4 by the least χ^2 fitting method, where number of degree of freedom (NDF) is 8 (=12 [number of layers of the sense wire plane] -4 [parameters]). In the local tracking, tracks with minimum χ^2 values of more than 20 were rejected as a fake track. Events with a single

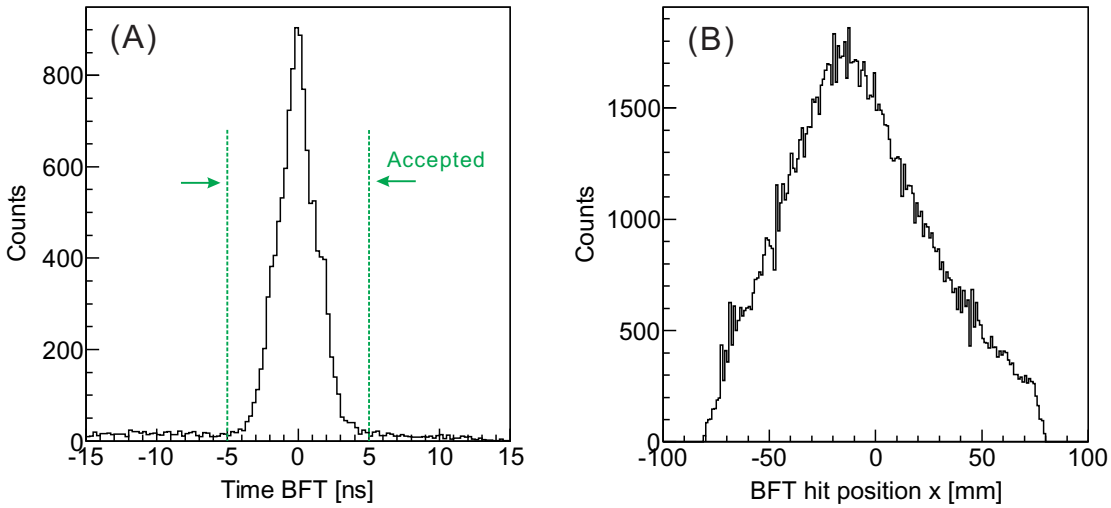

Figure 28: (A) Time distribution of BFT (BH2−BFT) and (B) hit profile of BFT for beam K^- mesons.

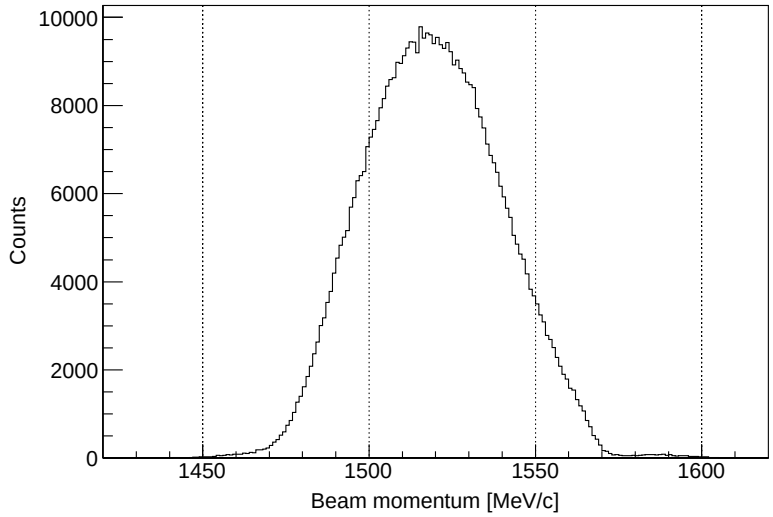

Figure 29: Momentum distribution of beam K^- measured by the beam spectrometer. The beam momentum was set at 1.5 GeV/c.

track was accepted. The yield loss due to the BC3,4 tracking was ∼2%. The track information obtained with the local tracking of BC3,4 was used as an incident vector of K^- for calculation of a scattering angle $\theta_{K\pi}$.

A momentum of the beam particle was uniquely calculated with the transport matrix using a horizontal position (x) at the upstream of QQDQQ magnets as well as positions (x,y) and a direction (u=Δx/Δz,v=Δy/Δz) at the downstream of the magnets. Figure 29 shows the reconstructed momentum distribution of the beam K^-.

A.1.2 Selection of K^-

Beam K^- particles were efficiently selected by aerogel Čerenkov counters (BAC1,2) at the trigger level. Figure 30 shows a time-of-flight distribution between BH1 and BH2 for KPI triggered events, where the horizontal axis is a time difference from the pion time-of-flight. A small amount of pions can still be seen in the spectrum. These contaminations were removed by selecting time-of-flight for kaons. The region of -3.2 ns $<$ beam TOF (BH1-BH2) < -0.5 ns was selected as the time gate for the beam K^- with a negligibly small loss of the beam K^- events. The time-of-flight (BH1–BH2) resolution was 155 ps in rms, and the K/π resolving power ($= \Delta t_{\pi\leftrightarrow K}/(\sigma_\pi + \sigma_K)$) was 5.4σ.

A.2 Analysis of scattered particle

A.2.1 Momentum reconstruction for scattered particle

The momentum vector of the scattered particle was reconstructed from the data of the drift chambers, SDC1,2 installed at the upstream of SKS magnet and SDC3,4 installed at the downstream of the magnet. A local straight track was drawn from measured positions in SDC1,2 for entering tracks into SKS and in SDC3,4 for outgoing tracks, by the least χ^2 fitting method. In the local tracking, tracks with minimum χ^2 values of more than 20 were rejected as fake tracks.

The Runge-Kutta method [7] was used for reconstruction of SKS trajectories using a magnetic field map. The magnetic field map was calculated by the TOSCA code [8] with the finite element method. The trajectory and the momentum of the scattered particle were obtained by

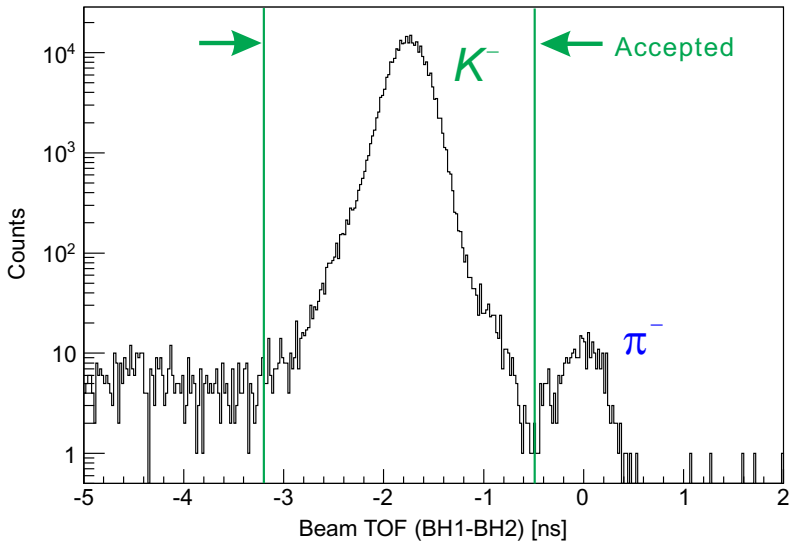

Figure 30: Time-of-flight distribution between BH1 and BH2 for KPI triggered events. The region of -3.2 ns $<$ beam TOF (BH1–BH2) < -0.5 ns was selected as the time gate for the beam K^-.

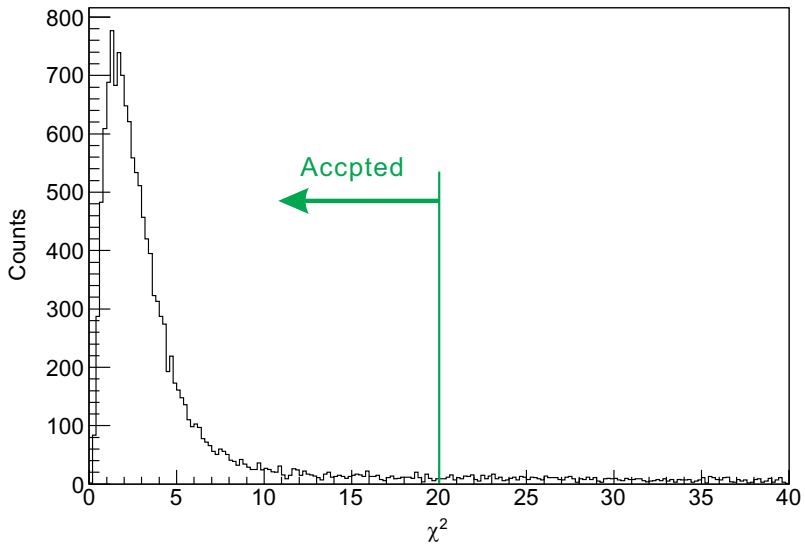

Figure 31: χ^2 distribution in the SKS tracking for scattered π^-.

the least χ^2 fitting method. The χ^2 value of SKS trajectory is defined as

$$\chi^2_{SKS} = \frac{1}{n-5}\sum_{i=1}^{n}\left[\frac{x_i^{\rm tracking} - x_i^{\rm data}}{\sigma_i}\right]^2,$$

where n is the number of layers having hits (the maximum number of layers is 22), $x_i^{\rm tracking}$ is the reconstructed hit position on the i-th layer on the SKS trajectory, and $x_i^{\rm data}$ and σ_i denote the measured hit position and the position resolution of the i-th layer, respectively. Typical position resolutions of a sense plane in these drift chambers are listed in Table 7. In the present analysis, events in which χ^2 in the SKS tracking was less than 20 were selected. Figure 31 shows a χ^2 distribution in the SKS tracking, and Fig. 32 shows the reconstructed momentum distribution for scattered pions selected by the time-of-flight method as described in the next section. Even after suppression of beam K^- decay events was applied using the SMF hit information, a small contamination from $K^- \to \mu^- + \bar{\nu_\mu}$ and a large contamination from $K^- \to \pi^- + \pi^0$ are expected to remain in this spectrum. Thanks to the wide momentum acceptance of SksMinus, Σ hyperon production events were also included in the data.

If more than one track was found in the local tracking, all possible combinations of those local tracks were tried in the SKS tracking. If reconstructed tracks do not pass through the hit segment of TOF, they were rejected as fake tracks in this analysis. Events in which more than one track remained were rejected. The yield loss by rejecting multi-track events was ∼3%. The track information reconstructed by the SKS tracking was used for an outgoing vector of π^- in calculation of a scattering angle $\theta_{K\pi}$.

A.2.2 Selection of π^-

In the KPI trigger, a large amount of background events were accepted due to a misidentified kaon as a pion by SAC1. To reject these events, a time-of-flight (BH2–TOF) cut was applied in

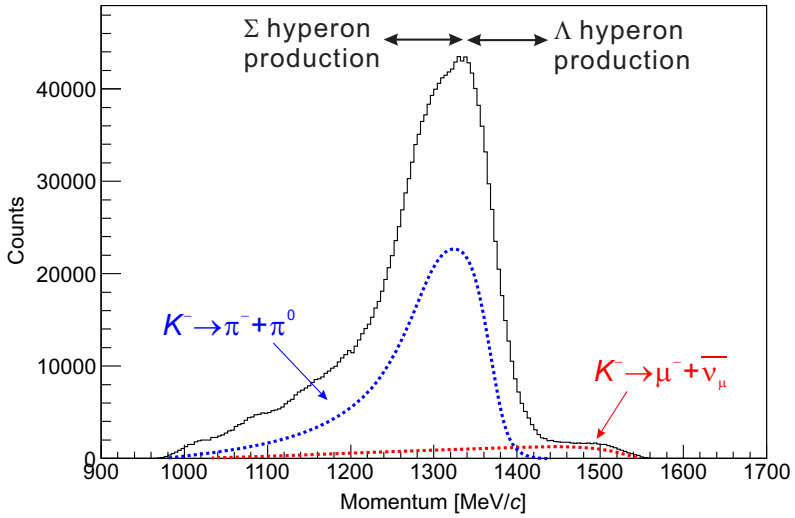

Figure 32: Momentum distribution reconstructed in the SKS tracking for scattered π^-. Contribution of beam K^- decay was estimated from data obtained with similar setup and no target material. See Section A.9 for a description of the beam K^- decay analysis.

the off-line analysis. By using the time-of-flight information and a result of the SKS tracking, the mass of the scattered particle ($M_{\rm scat}$) can be calculated as

$$M_{\rm scat} = \frac{p}{\beta}\sqrt{1-\beta^2}, \quad \beta = \frac{L}{c\Delta t},$$

where p is the momentum of the scattered particle reconstructed by the SKS tracking, and β is a velocity of the scattered particle. β was calculated from a path length of a trajectory (L) between the target and TOF (typically of 5 m) obtained by the SKS tracking analysis and a time-of-flight (Δt) between BH2 and TOF correcting for a distance between BH2 and the target. Figure 33 shows a mass square spectrum for scattered particles in the unit of $({\rm GeV}/c^2)^2$ for the KPI triggered events. Contamination from "beam K^- scattering" events is seen in the spectrum. The region of -0.10 $({\rm GeV}/c^2)^2 < M^2_{\rm scat} < 0.15$ $({\rm GeV}/c^2)^2$ was selected for the scattered π^-. The K/π resolving power ($= \Delta t_{\pi\leftrightarrow K}/(\sigma_\pi + \sigma_K)$) was 3.6σ where a dominant inaccuracy came from the time-of-flight (BH2–TOF) resolution of 135 ps in rms.

A.3 Reconstruction of scattering angle and reaction vertex

The scattering angle ($\theta_{K\pi}$) and the reaction vertex point were determined from vectors of an incident particle and an outgoing particle at the target region. The track obtained by the local tracking of BC3,4 was used as an incident particle vector, while the track from the SKS tracking was used as an outgoing particle vector instead of the straight track from the local tracking of SDC1,2, because of an effect of the magnetic fringing field of the SKS magnet at the SDC1,2 position.

The scattering angle ($\theta_{K\pi}$) was defined as the angle between the vectors of the incident particle and the outgoing particle in the laboratory frame. The resolution of $\theta_{K\pi}$ was checked

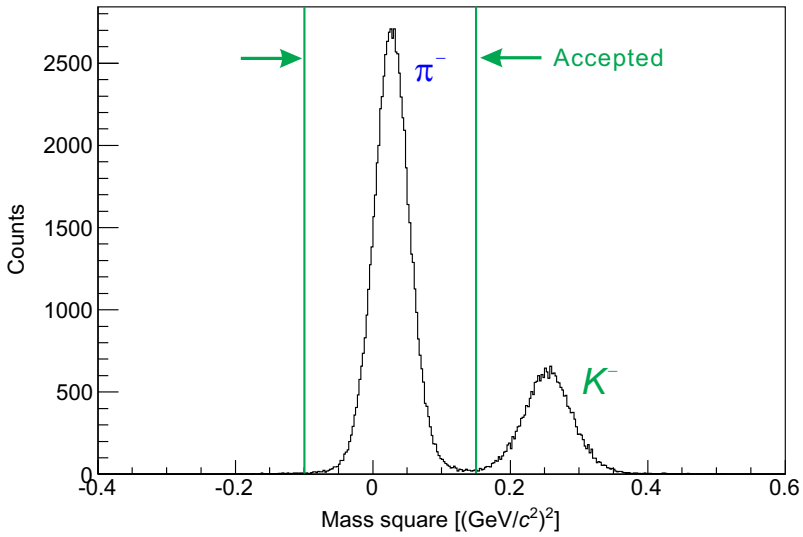

Figure 33: Mass spectrum for scattered particles for the KPI triggered events. The mass is plotted in the scale of mass square.

using beam-through data by letting beam pions having a momentum of 1.5 GeV/c pass through both the beam line spectrometer and SksMinus with a liquid helium target. The resolution was better than 0.5 deg. (FWHM).

The reaction vertex point was determined by taking a spatially closest point between the vectors of the incident particle and of the outgoing particle. Figure 34 (A) shows projections of the reaction vertex position onto the z-axis (z-vertex distribution) for the beam K^- scattering events, where the z axis is defined as the beam direction and z=0 is defined as the center of Hyperball-J. In this figure, a black line shows the vertex point distribution with the liquid helium target, and the blue line with the empty target vessel. Background events in which the beam particle was scattered in the material of the detectors around the target (BH2, BACs, SAC1, SDC1) are shown in blue. On the other hand, an enhancement near the center was found with the liquid helium., which indeed indicates the presence of liquid helium in the target vessel. Figure 34 (B) shows a z-vertex distribution for the (K^-, π^-) events for the KPI triggered events. In this distribution, a large amount of beam K^- decay events that occurred between BACs and SAC1 ($\sim$45 cm in distance) overlapped with true (K^-, π^-) reaction events. Because of this background in the KPI triggered events, accepted gate for the z-vertex position was decided using the beam K^- scattered events. The z-vertex resolution depends on $\theta_{K\pi}$ and was 22 mm (σ) at $\theta_{K\pi}$= 5°, which was measured with a thin stainless steel target described in Section A.5.

Figure 35 shows a contour plot of z-vertex points versus $\theta_{K\pi}$ for the beam K^- scattered events with liquid helium. Events in which $\theta_{K\pi}$ was less than 3.5° were rejected in the present analysis because of a worse z-vertex resolution and also of a large amount of contamination from beam $K^- \rightarrow \pi^- + \pi^0$ decay events which kinematically overlap with the hypernuclear production events. To reject a background events from material other than liquid helium, a z-vertex cut was applied in the present analysis. A region of -140 mm $<$ z-vertex point $<$ 120

mm was selected in the analysis. The yield loss due to this tight z-vertex cut was estimated to be ∼4% in total by a simulation using an angle dependence of the ^{4}He(1^+) production cross section based on a DWIA calculation [23].

A.4 Calculation of missing mass

The missing mass is calculated using measured momenta of the beam K^- meson and of the scattered π^- meson and the scattering angle ($\theta_{K\pi}$) as described in Section A.1. In the present analysis, we applied corrections for measured momenta of the kaon (p_K) and the pion (p_π), namely, (1) the horizontal and vertical angle dependence for p_K, (2) the energy loss in the target for p_K and p_π.

Horizontal and vertical angle dependence for p_π

In the SKS magnet system, a measured p_π has a systematic shift which depends on the trajectory through the SKS magnet due to an ambiguity in the calculated magnetic field map. In the present analysis, the measured p_π was corrected with a 2nd-order polynomial function of

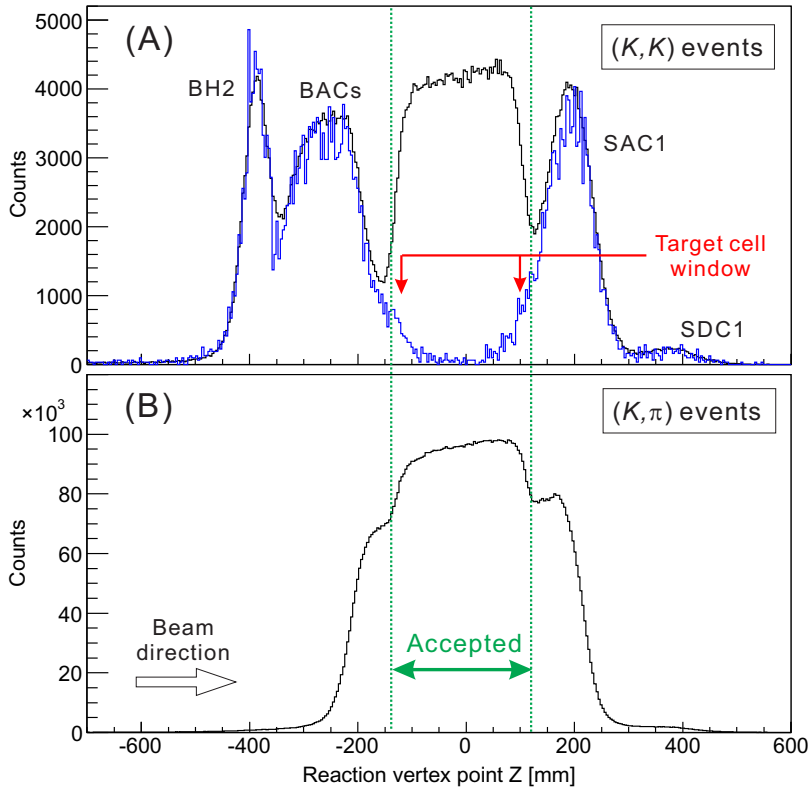

Figure 34: Z-axis projection of the reaction vertex position, where z axis is defined as the beam direction: (A) the distribution for the beam K^- scattering events, (B) the distribution for the KPI triggered events. In the spectrum (A), black line and blue line show the vertex distribution with the liquid helium target and with the empty target vessel, respectively.

horizontal angle ($u = dx/dz$) and vertical angle ($v = dy/dz$) of the scattered π^- vector at the target position. This correction was usually applied for the SKS analysis in the previous experiments [22, 24, 25, 26]. Figure 36 (A) shows contour plots of the calculated missing mass for the ^{4}He$(K^-, \pi^-)X$ kinematics versus the horizontal angle (u) of scattered π^-, and (B) shows that for the vertical angle (v). The missing mass is plotted in excitation energy ($E_{\rm ex}$). A major peak for the $^4_\Lambda$He(0^+ or 1^+) production is seen around $E_{\rm ex}$=0 in these plots. We determined optimum parameters of the 2nd-order polynomial functions for the correction by comparing measured $p_\pi^{\rm measured}$ and calculated $p_\pi^{\rm calcurated}$ with the ^{4}He$(K^-, \pi^-)^4_\Lambda$He kinematics. Figure 36 (C) and (D) show the plots after the u and v corrections, respectively.

Energy loss in the target for p_K and p_π

The momentum of the beam K^- at the reaction point was reduced from the p_K measured by the beam line spectrometer due to energy loss effects in the trigger counters (BH2, BAC1,2) and some materials of the target system (thin windows and liquid helium). The momentum of the scattered π^- just after the reaction should be larger than the p_π measured by SKS due to energy loss in some parts of the target system and SAC1. These energy loss effects were estimated by a simulation using the Geant4 code. The energy losses were estimated to be 7.3 MeV in total for the beam K^- having a momentum of 1.5 GeV/c and 4.0 MeV for the scattered π^- with p_π=1.4 GeV/c, when the reaction point is at the center of the target. Difference in the momenta p_K (and also p_π) was not considered because a change in the energy loss is less than 0.1 MeV against 0.1 GeV/c momentum change. The energy loss in the liquid helium with a total length of ∼230 mm was estimated to be ∼5 MeV, but the dependence of the calculated

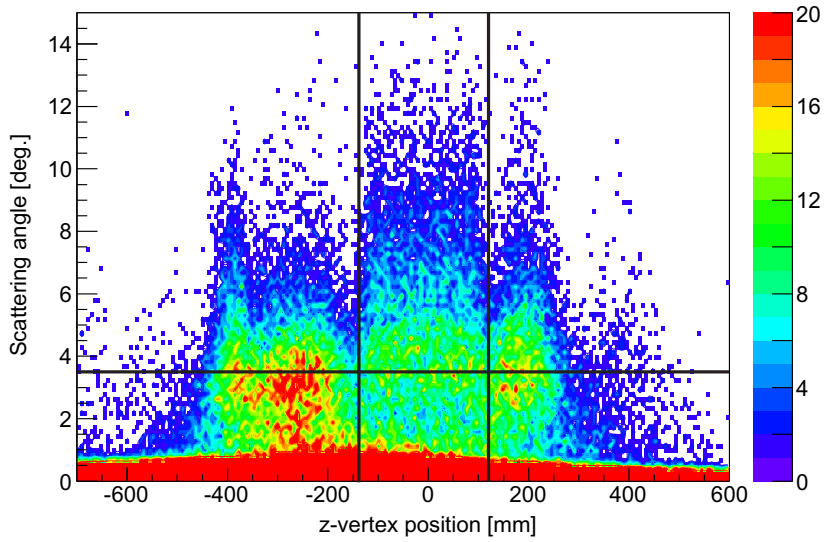

Figure 35: Contour plot of z-vertex points versus $\theta_{K\pi}$ for the beam K^- scattering events with liquid helium. Region of -140 mm $<$ z-vertex point $<$ 120 mm was selected as the reaction events on helium. Events in which $\theta_{K\pi}$ was less than 3.5° were rejected because of a worse z-vertex resolution and also a large amount of contamination from beam $K^- \to \pi^- + \pi^0$ decay events.

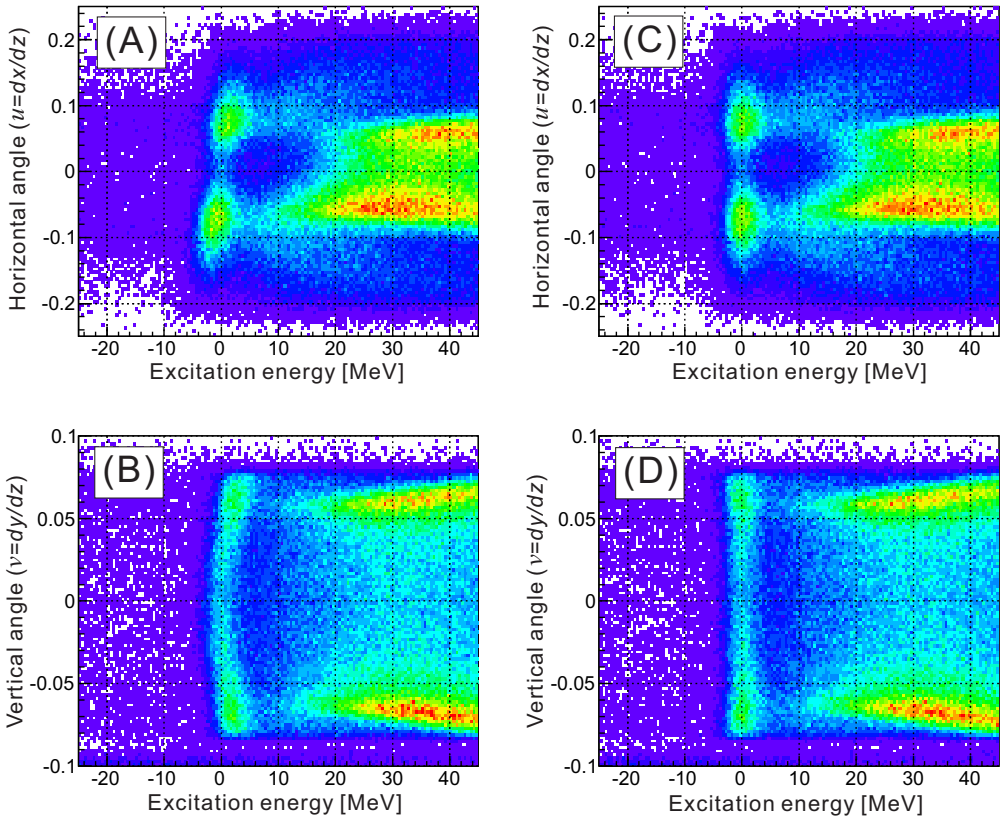

Figure 36: (A): Contour plots of calculated missing mass for the ^{4}He$(K^-,\pi^-)X$ kinematics versus the horizontal angle (u) of scattered π^-, (B): that for the vertical angle (v). (C) and (D): these plots after the u and v correction, respectively. A major peak for the $^4_\Lambda$He(0^+ or 1^+) production is seen around $E_{\rm ex}$=0.

missing mass on the reaction point along the z-axis is estimated to be much smaller (∼0.2 MeV) than the energy resolution of our spectrometer system (∼5 MeV). Therefore, energy loss difference along z-vertex points was not taken into account in this analysis.

A.5 Mass spectrum of Σ^+ and $^{12}_\Lambda$C

For validating our missing mass analysis as well as our detector system, we took data with a polyethylene (CH_2) target with a thickness of t=2.9 g/cm^2 that is almost the same as the liquid helium target [2.8 g/cm^2]. With the corrected momentum of the beam kaon ($p_K^{\rm corrected}$), that of the scattered pion ($p_\pi^{\rm corrected}$) and the scattering angle ($\theta_{K\pi}$), the missing mass is calculated for the $p(K^-,\pi^-)\Sigma^+$ and ^{12}C$(K^-,\pi^-)^{12}_\Lambda$C kinematics.

Figure 37 (A) shows a missing mass spectrum for the $p(K^-,\pi^-)X$ reaction. Σ^+ producing events were clearly observed on top of the beam K^- decay background and hyperon production with a $^{12}_\Lambda$C nucleus. An energy resolution of 4.9(1) MeV (FWHM) is achieved.

Figure 37 (B) shows a missing mass spectrum for the ^{12}C$(K^-,\pi^-)X$ kinematics in which data points are plotted against the Λ-binding energy (-B_Λ) scale. Decay events were suppressed

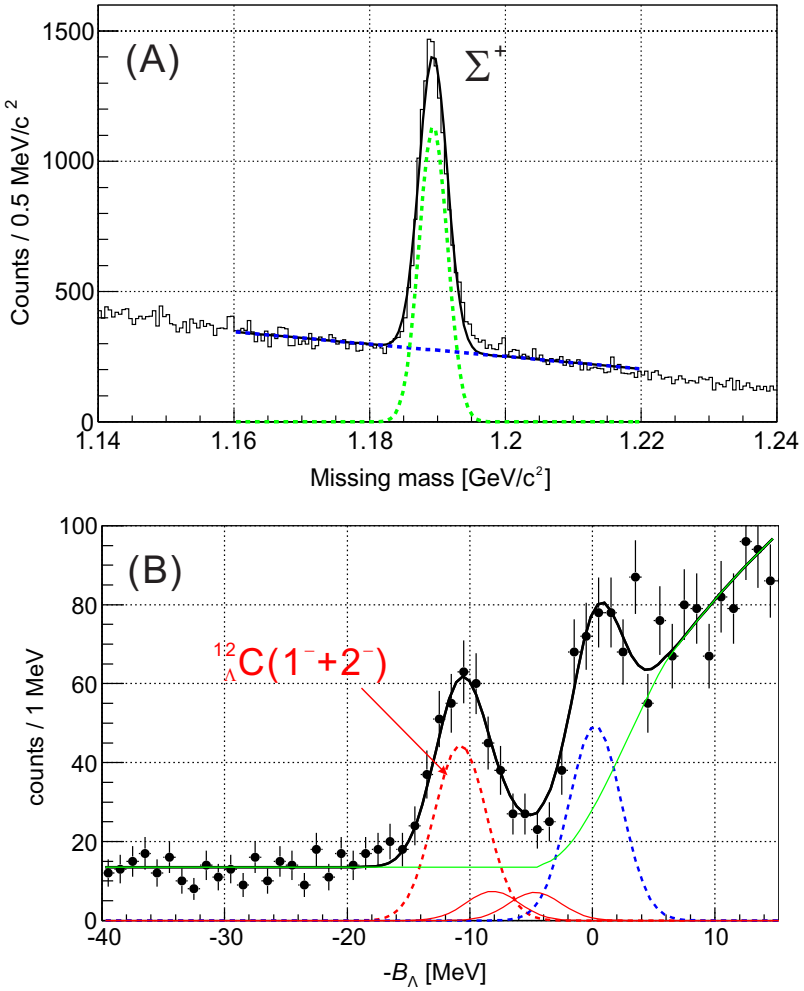

Figure 37: Missing mass spectra with a CH_2 target (t=2.9 g/cm^2): (A) shows the spectrum for $p(K^-,\pi^-)X$ kinematics. Peak structures in these spectra correspond to elementary Σ^+ production events. (B) shows the spectra for the ^{12}C$(K^-,\pi^-)^{12}_{\Lambda}$C reaction, in which data points are plotted against the Λ-binding energy ($-B_\Lambda$). Scattering angles of 4–15° were selected to avoid contamination of beam K^- decay events. Energy positions and relative cross sections ($\sigma_{\rm coreexcited}/\sigma_{g.s.}$) of $^{12}_{\Lambda}$C core exited states are taken from the past experiment [27] in the fitting. K^- decay events were suppressed using SMF.

by using SMF and by selecting $\theta_{K\pi}$ >4° in this spectrum. Two peak structures can be seen. Each peak corresponds to the s- and p-Λ states of $^{12}_{\Lambda}$C, respectively. In the fitting, relative energy positions and cross sections ($\sigma_{\rm core\ excited}/\sigma_{g.s.}$) of $^{12}_{\Lambda}$C core exited states are taken from the past experiment using the (π^+,K^+) reaction [27]. The background function is defined as $a\sqrt{E_{>threshold}}+b$. First, $\sqrt{E_{>threshold}}$ function for the energy distribution of the quasi-free Λ production is assumed where $E_{>threshold}$ denotes an excess energy from B_Λ=0. Secondly, constant b for the distribution of the beam K^- decay contamination is taken, of which shape was confirmed from data with the empty target to be almost flat in the shown mass range.

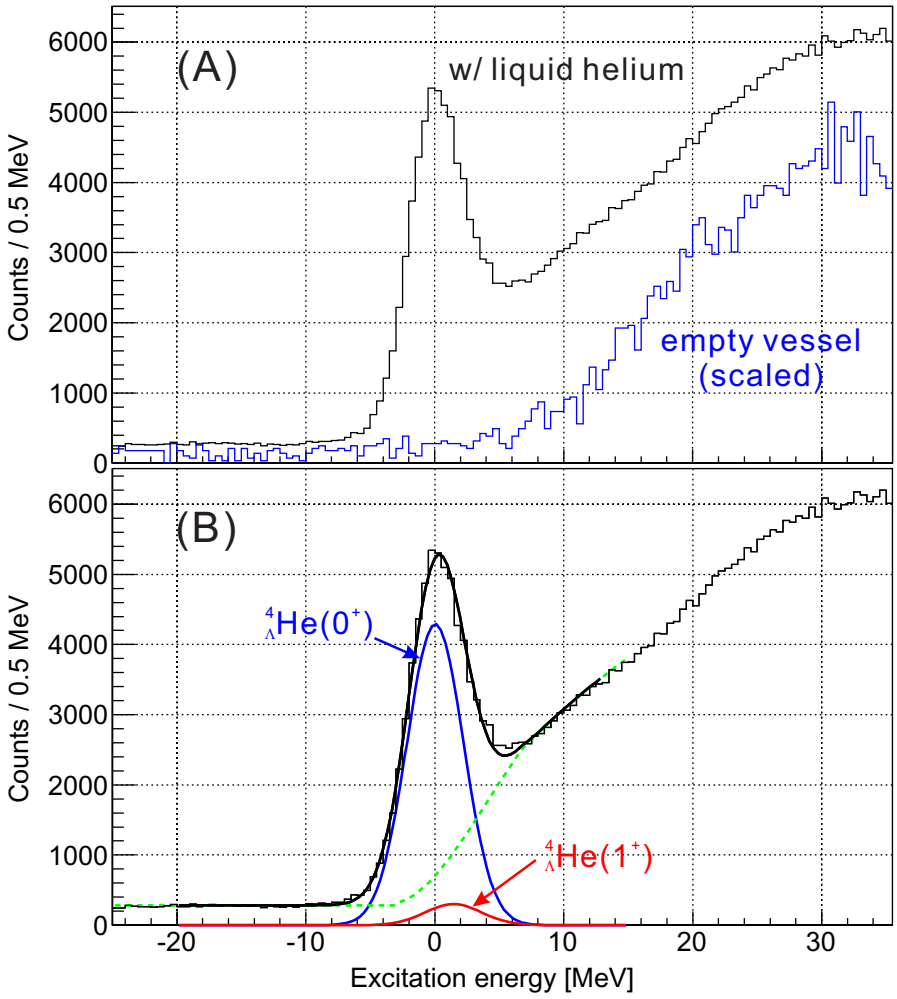

Figure 38: The missing mass spectrum for the ^{4}He$(K^-,\pi^-)^4_\Lambda$He kinematics plotted as a function of the excitation energy, $E_{\rm ex}$, where events with scattering angles ($\theta_{K\pi}$) larger than 3.5° are selected. In figure (A), black and blue lines show a spectrum with and without liquid helium, respectively. Figure (B) shows a result of the fitting using the result of the γ-ray analysis.

The missing mass resolution, assumed as 5 MeV (FWHM), was convoluted into the background distribution as Gaussian. From the fit result, a missing mass resolution of 4.8(3) MeV (FWHM) is obtained combined with the beam line spectrometer.

The accuracy of absolute mass (energy) scale was estimated to be ∼1 MeV from the difference between the obtained peak position and the known mass of $^{12}_{\Lambda}$C [28]. From these results, we validated our analysis procedures for obtaining the missing mass.

A.6 Mass spectrum of $^4_\Lambda$He

Figure 38 shows the missing mass spectrum plotted as a function of the excitation energy, $E_{\rm ex}$, where the missing mass was calculated for the ^{4}He$(K^-,\pi^-)^4_\Lambda$He kinematics. Events with

scattering angles ($\theta_{K\pi}$) larger than 3.5° are selected to reduce the background due to beam $K^- \to \pi^- + \pi^0$ decay events. The background spectrum associated with materials other than liquid helium as well as with K^- beam decay events was obtained with the empty target vessel as shown together in Fig. 38 (A); it is evident that the observed peak originates from the ^{4}He(K^-, π^-) reaction. In the spectrum with the empty target vessel, dominant events in the region of $E_{\rm ex}$ >10 MeV came from the beam $K^- \to \pi^- + \pi^0$ decay events. A small amount of constant background covering the entire region of the spectrum corresponds to the (K^-, K^-) events which remained even after the particle identification described in Section A.3.2 and beam $K^- \to \mu^- + \bar{\nu_\mu}$ decay events resulted from the inefficiency of SMF. According to a theoretical calculation, the $^4_\Lambda$He(0^+) ground state is predicted to be predominantly populated, while the $^4_\Lambda$He(1^+) excited state is produced at a lower rate ($\sim 1/4$ of $^4_\Lambda$He(0^+)) [23]. Therefore, the obtained peak is composed of $^4_\Lambda$He(0^+) with a small contribution from $^4_\Lambda$He(1^+), and the peak width of 5 MeV (FWHM) approximately corresponds to the missing mass resolution. Figure 38 (B) shows a fit result of the missing mass spectrum with two Gaussian functions and a background function where the threshold energy ($E_{>threshold}$) of 2.39 MeV (corresponds to $B_\Lambda = 0$) was taken from the emulsion experiment [29]. (See Section A.6 for a description of background function.) The center position and the height of the second Gaussian function was fixed according to the result of the present analysis. The obtained peak width [5.1(1) MeV (FWHM)] is consistent with the resolution in the test data of $^{12}_\Lambda$C production.

A.7 Information for the Doppler correction

A produced hypernucleus $^4_\Lambda$He has a recoil velocity (β) at the time of reaction, then slows down in the target medium. Figure 39 (A) shows a calculated initial velocity (β) of the produced $^4_\Lambda$He as a function of $\theta_{K\pi}$ for the (K^-, π^-) reaction with a beam momentum of 1.5 GeV/c, and (B) shows a changing rate of the velocity of the $^4_\Lambda$He traversing the target medium estimated by a simulation using the SRIM code [30]. The minimum stopping time was estimated to be 25 ps. γ rays were emitted from $^4_\Lambda$He immediately after the production because of an estimated life time of the $^4_\Lambda$He(1^+) state is of ∼0.1 ps assuming weak coupling between the core nucleus and the Λ [31]. Then, the γ-ray energy measured by Ge detectors was shifted due to Doppler effect.

In the analysis of the Ge detectors, the Doppler correction is applied to obtain γ-ray energy spectra by using a following equation,

$$E_\gamma^{\rm corrected} = E_\gamma^{\rm measured} \cdot \frac{1}{\sqrt{1-\beta^2}}(1 - \beta\cos\theta_\gamma),$$

where $E_\gamma^{\rm corrected}$ and $E_\gamma^{\rm measured}$ are a corrected γ-ray energy and a measured energy by the Ge detector, respectively, β denotes velocity of the hypernucleus, θ_γ is an angle between the momentum of the hypernucleus and the γ-ray. The momentum and the velocity (β) of $^4_\Lambda$He just after the reaction are used for the Doppler-shift correction. Reduction of β in 0.1 ps after the reaction is estimated to be less than 0.05%. The γ-ray vector is defined as a vector from the reaction vertex point to the center position of the registered Ge crystal. The spatial distance between the γ emission point and the reaction vertex is expected to be less than 10 μm with a life time of 0.1 ps, and thus is negligibly small comparing with the vertex resolution (∼20

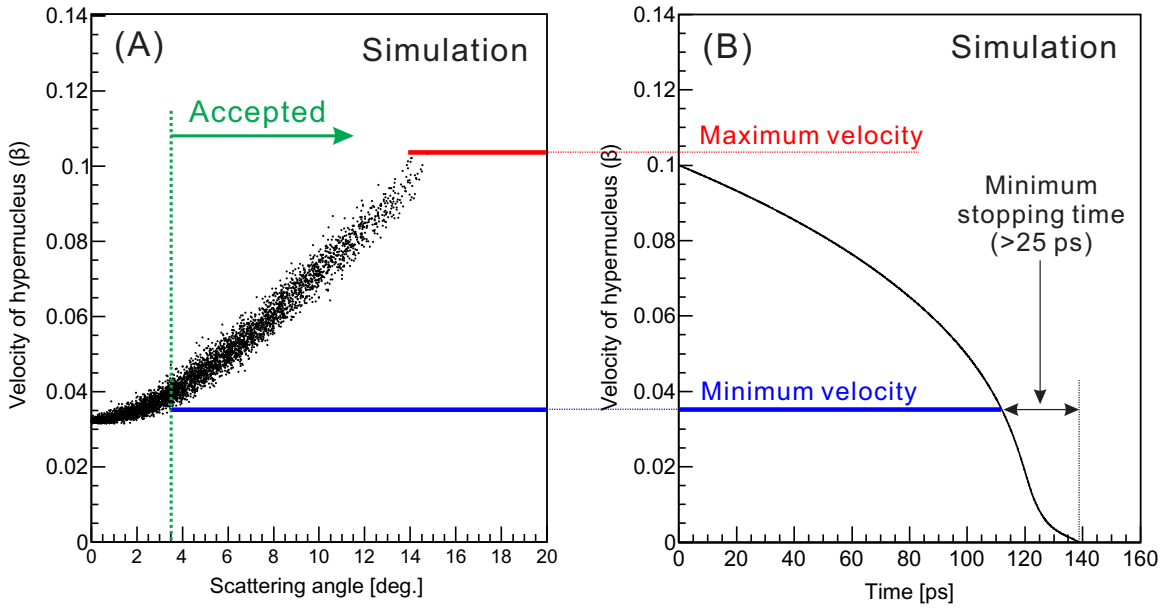

Figure 39: Calculated velocity and stopping time of the produced ${}^{4}_{\Lambda}$He, (A): initial velocity (β) of the produced ${}^{4}_{\Lambda}$He as a function of $\theta_{K\pi}$ for the (K^-, π^-) reaction with a beam momentum of 1.5 GeV/c, (B): changing rate of the velocity (recoil speed) of the ${}^{4}_{\Lambda}$He in the target medium.

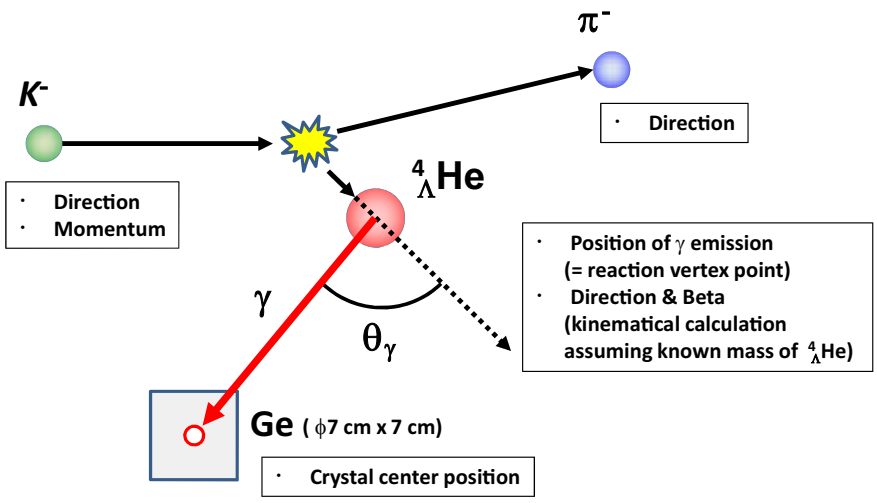

Figure 40: Illustration of the Doppler-shift correction.

mm) and the size of Ge crystal (ϕ70 mm$\times$ ℓ = 70 mm). Figure 40 illustrates the Doppler-shift correction method.

The information from the (K^-, π^-) analysis used for the Doppler-shift correction is summarized below:

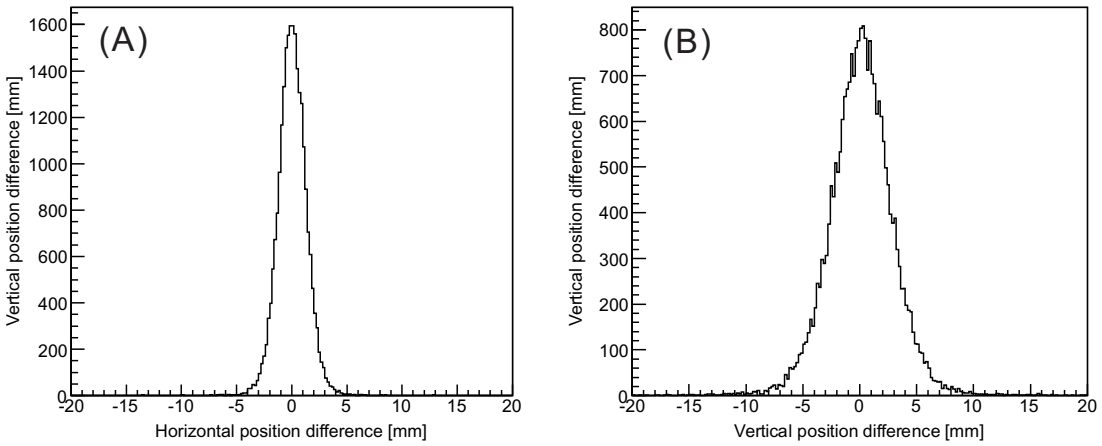

Figure 41: (A) distribution of a difference in the x-position of the incident vector and the outgoing vector at the target, (B) that in the y-position.

- recoil momentum of hypernuclei,
- reaction vertex position as a point of γ-ray emission.

In the following section, calculation of the recoil momentum of the produced hypernuclei and estimation of the reaction vertex resolution are described.

Recoil momentum of hypernuclei

The recoil momentum of hypernuclei was calculated using reconstructed tracks from the (K^-, π^-) analysis by using kinematical conservation laws. For the calculation, inputs are listed as follow: (1) the vectors of the incident kaon and the scattered pion, (2) the measured momentum of the incident kaon (p_K), (3) the known mass of ${}^{4}_{\Lambda}\mathrm{He}(0^+) + 1$ MeV(excitation energy). The measured momentum of the scattered pion (p_π) is not used in this calculation because of uncertainty in the calibration of the absolute momentum scale based on the calculated magnetic field map. The Λ binding energy for the ${}^{4}_{\Lambda}\mathrm{He}(0^+)$ of 2.39 MeV was taken from the past emulsion experiment [29]. The effect of a 1 MeV change in the ${}^{4}_{\Lambda}\mathrm{He}$ mass is estimated to be negligibly small. The accuracy of the velocity of the hypernucleus was estimated to be 1.2% (< 0.001 in β) from a simulation.

Reaction vertex resolution

In the analysis of Ge detectors, we estimated a γ-ray peak width after the Doppler-shift correction. The reaction vertex resolution was used as an input in this estimation.

x- and y-vertex position The x- and y-vertex position resolutions were checked by using data with a liquid helium target, in which the beam particles pass through both the beam line spectrometer and SksMinus. In these events, x and y positions of the incident vector and

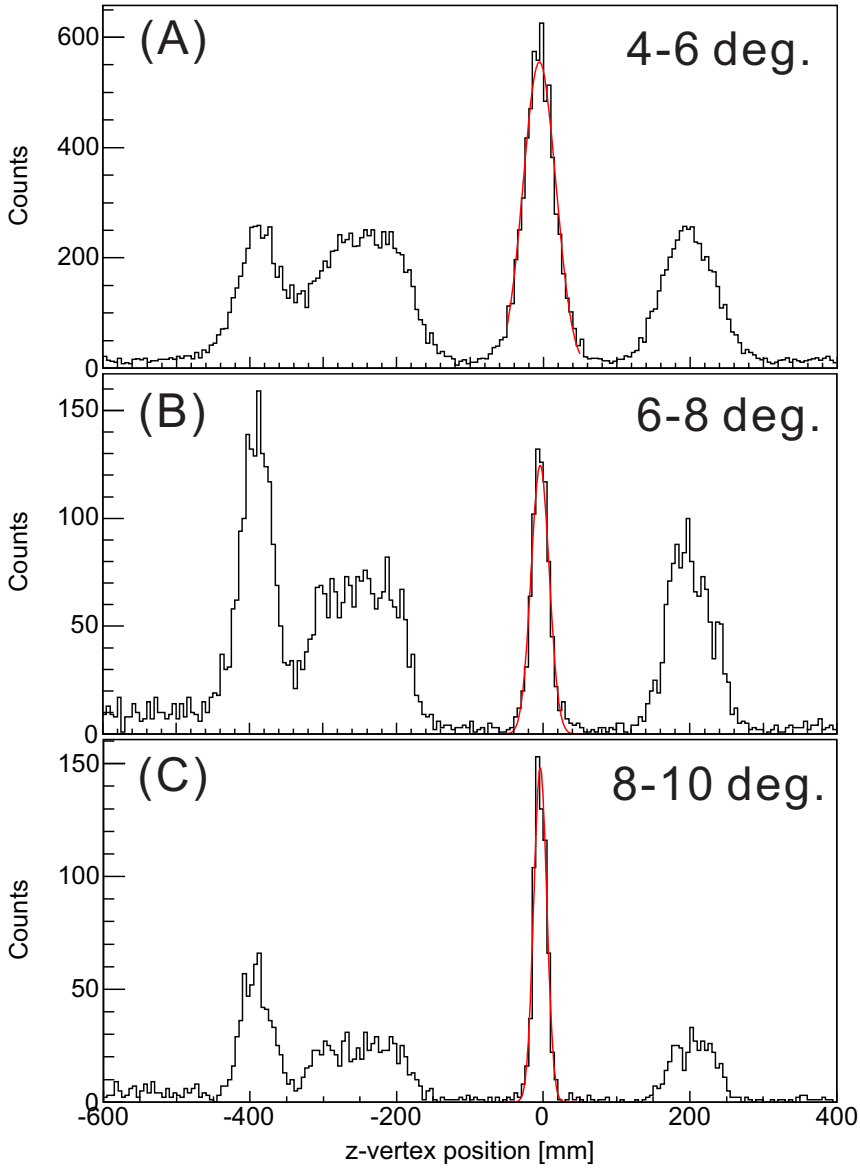

Figure 42: Z-vertex distributions with the SUS target for the beam particle scattering events. (A), (B) and (C) are for the scattering angles ($\theta_{K\pi}$) of 4°–6°, 6°–8°, and 8°–10°, respectively.

of the outgoing vector at the target should be identically the same. Figure 41 (A) shows a distribution of a difference in the x-position of incident vector and the outgoing vector at the target, reconstructed from the analysis of the beam line spectrometer and SksMinus, respectively. Similarly Figure 41 (B) shows a distribution for the y-position. The resolutions of x- and y-vertex positions were 1.2 mm and 2.6 mm (σ), respectively.

z-vertex position The z-vertex resolution was checked with a thin stainless steel (SUS) target (t=3 mm) data. Figure 42 shows z-vertex distributions at $\theta_{K\pi}$=4°–6°, 6°–8°, and 8°–10°

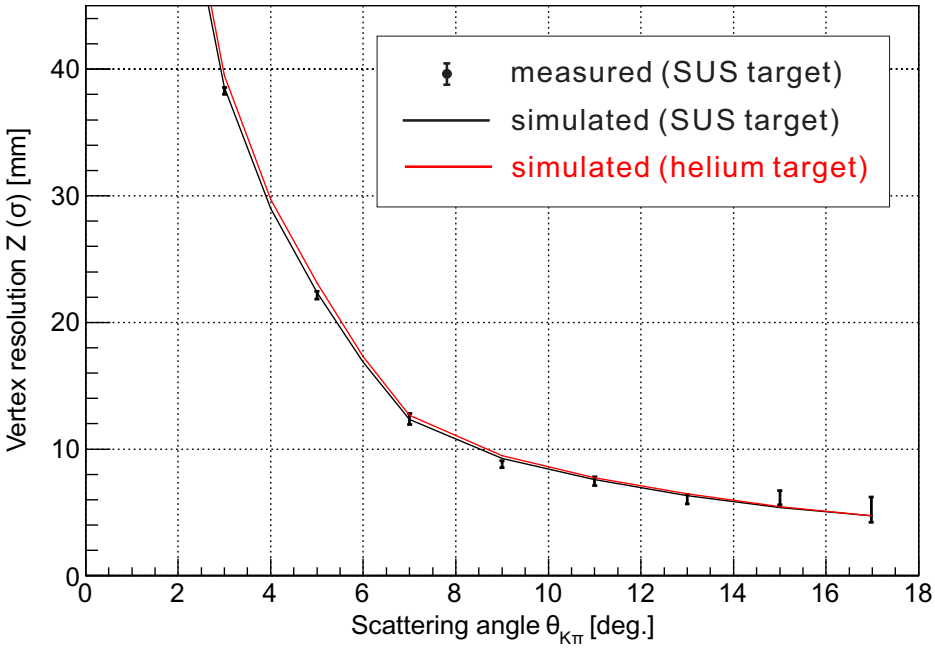

Figure 43: z-vertex resolution as a function of $\theta_{K\pi}$ obtained by a fitting of data with thin SUS target (t=3 mm). Black and red line are simulated vertex resolutions with the thin SUS target and the long liquid helium target, respectively.

for the beam particle scattered off the SUS target. The z-vertex resolution was obtained by a fit of this spectrum and is shown in Fig. 43 as a function of $\theta_{K\pi}$. The resolution of the z-vertex position was 22 mm (σ) at $\theta_{K\pi} = 5°$. The effect of the thickness of the SUS target (t=3 mm) is estimated to be less than 0.1 mm (σ) for the obtained resolution, and thus is ignored in the estimation.

With the liquid helium target, of which length in z-axis is longer (∼230 mm) than that of the SUS target, the z-vertex resolution becomes worse due to a multiple scattering effect. This effect was estimated by a simulation using the GEANT4 code. The simulated z-vertex resolutions are shown together in Fig. 43; black line and red line shows the simulated values with the thin SUS target and with the long helium target, respectively. From these results, the difference in z-vertex resolution between the SUS target and the liquid helium target is estimated to be ∼1 mm at $\theta_{K\pi}$=5°. The estimated resolutions for the liquid helium target was used for the peak shape simulation. The accuracy of the simulated resolution is expected to be less than 2 mm, which is obtained from the difference between the measured and estimated resolutions.

A.8 Performance of decay suppression counter

The efficiencies of SP0 and SMF for beam-decay events were checked with the KPI trigger for the empty target, where only K^- decay events make the KPI trigger. $K^- \to \pi^- + \pi^0$ and $K^- \to \mu^- + \overline{\nu_\mu}$ events are selected by missing mass spectrum, gating corresponding mass

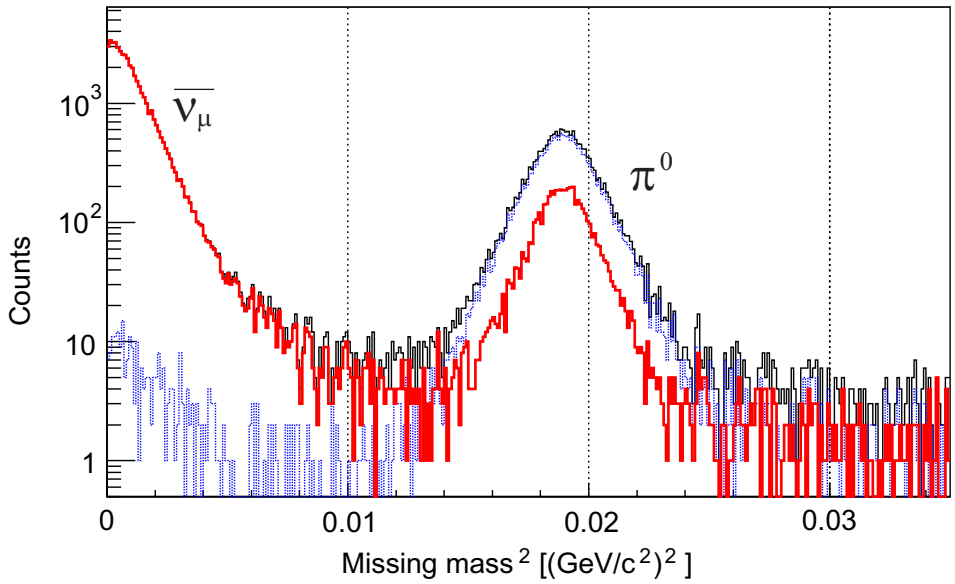

Figure 44: Missing mass square (M^2) distributions for the KPI trigger with empty target, reconstructed by missing mass analysis for empty$(K^-, \pi^-)X$ kinematics (solid black line). Enhancements around $M^2 = 0$ and $= 0.02$ correspond to particles from K^- decay, $\overline{\nu_\mu}$ and π^0, respectively. Decay events can be suppressed by SP0 multiplicity cut (thick red line) and SMF cut (dotted blue line).

regions for π^0 and $\overline{\nu_\mu}$. Figure 44 shows a missing mass square distribution reconstructed for $K^- \to \pi^- X$ kinematics, assuming $m_{\mu^-} \simeq m_{\pi^-}$.

$K^- \to \pi^- + \pi^0$ rejection using SP0

By selecting number of hit layers in SP0 with setting threshold for the number, $K^- \to \pi^- + \pi^0$ events can be suppressed. The suppression with SP0, however, was not applied in the present analysis for ${}^{4}_{\Lambda}$He production because of a large branching ratio of π^0 emission decay channel leading ∼6% yield loss [32]. Figure 45 shows number of hit layers for events of the decay channel. The numbers for events of Σ^+ production via the (K^-, π^-) reaction was also shown, from where misidentification ratio for hypernuclear production due to detecting π^0 from Λ decay can be checked, considering analogy between Λ and Σ^+ in out going particles from their decay. These show different distributions; decay events fire 1–8 layers while 0–2 for Σ^+ production events. Setting hit layer threshold as 3, more than 69% of the decay events were tagged for over all SksMinus acceptance as shown in Fig.44 and 45, while misidentification ratio of Σ^+ production is obtained to be ∼11%. Focusing on scattering angles of 2°–4° in where the decay events kinematically overlap with hypernuclear production events as shown in Fig.46, the suppression efficiency is 54%. Misidentification ratio for ${}^{12}_{\Lambda}$C production events is estimated to be ∼2% by Monte Carlo simulation considering decay branching ratio [33] and minor difference with Σ^+ decay [32]. Suppression performance of SP0 is summarized in Table 10.

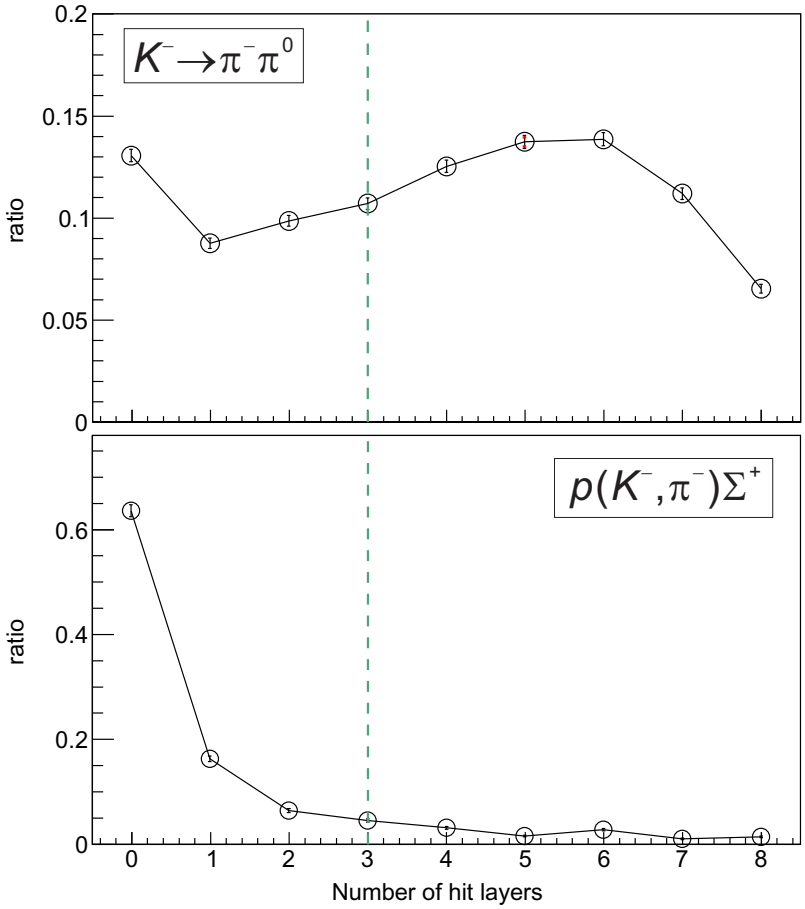

Figure 45: Number of hit layers of SP0 for $K^- \to \pi^- + \pi^0$ decay events (upper) and Σ^+ production events (lower). The layer multiplicity threshold is set to be >3 as shown in dashed green line.

Table 10: Suppression efficiency of SP0 and SMF

	Efficiency
SP0 efficiency (layer multiplicity ≥ 3)	
$K^- \to \pi^- + \pi^0$ events (θ:1–12°)	69(1)%
$K^- \to \pi^- + \pi^0$ events (θ:2–4°)	54(1)%
Σ^+ production events	11(1)%
SMF efficiency	
$K^- \to \mu^- + \overline{\nu_\mu}$ events (θ:1–14°)	99.5(1)%
$K^- \to \mu^- + \overline{\nu_\mu}$ events (θ:5–7°)	99.5(1)%
Σ^+ production events	13(1)%

$K^- \to \mu^- + \overline{\nu_\mu}$ rejection using SMF

By requiring SMF hit, more than 99.5% of $K^- \to \mu^- + \overline{\nu_\mu}$ events were suppressed as shown in Fig. 44. Misidentification of hypernuclear production events can be caused by scattered π^-

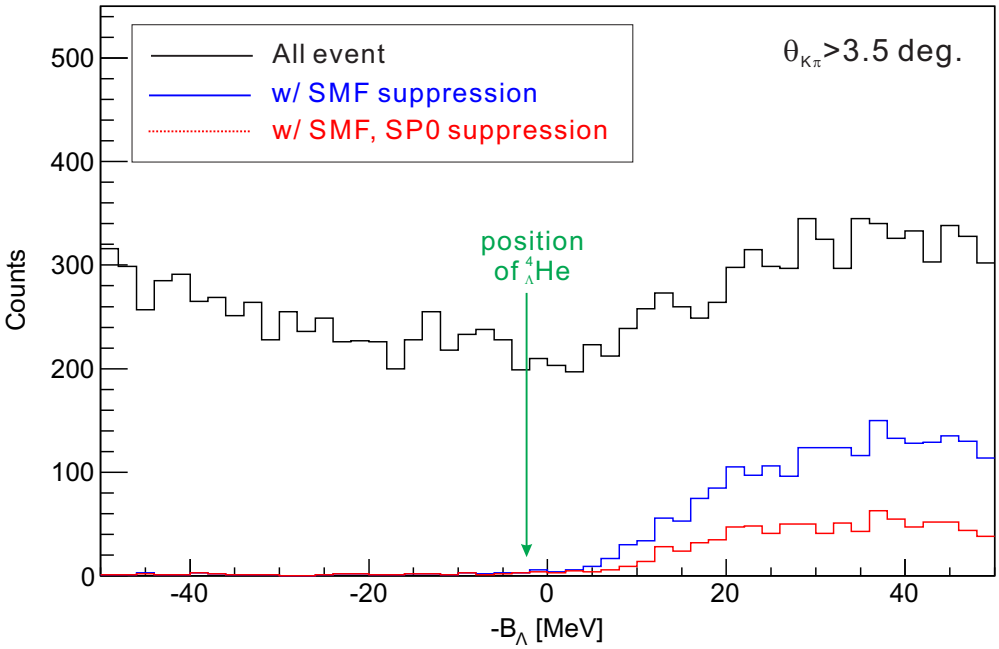

Figure 46: Binding energy spectra with empty target reconstructed for ^{4}He$(K^-,\pi^-)^4_\Lambda$He kinematics. Decay events (black line) which overlap to region of the hypernuclear production (green lines) can be suppressed using SMF as shown in blue line. Dotted red lines show spectra in which both SMF and SP0 are used for the suppression.

which is not stopped in the iron block and also by neutrons and γs generated from the absorption of π^-. To check this effect, the over-kill probability for Σ^+ production was measured to be $\sim$13%. The probability for hypernuclear production is estimated to be $\sim$10% [32]. Suppression performance of SMF is also summarized in Table 10. By adding the SMF (veto) signal to the trigger, the trigger rate was reduced to $\sim$43% leading 37% increase of the efficiency of the data-acquisition system.

Effect of the beam decay suppression on the missing mass spectrum

Figure 46 shows missing mass distribution for K^- decay events obtained with empty target, reconstructed for ^{4}He$(K^-,\pi^-)^4_\Lambda$He kinematics. The distribution with suppression using SP0 and SMF are also shown. More than 95% of background events in hypernuclear mass region can be suppressed by using SMF, leading to better S/N ratio in the γ-ray energy spectrum as well as in the hypernuclear mass spectrum. The contamination from the π^0 emission decay channel was small in the hypernuclear bound region when events in which the scattering angle ($\theta_{K\pi}$) of $<3.5^\circ$ are selected.

B Hyperball-J

In this Appendix, the performance of the Ge detector array, Hyperbal-J in the E13 experiment is described.

The analysis procedure of Hyperball-J data is illustrated in Fig. 27 and also summarized below:

- event selection by using timing information of the Ge detectors and the PWO counters,
- energy calibration of the Ge detectors,
- Doppler-shift correction for γ-ray energy,
- simulation of a peak shape in the Doppler-shift corrected spectrum.

B.1 Event selection

The timing signal from the Ge detectors was not used for the KPI trigger. The accepted coincidence time window between the Ge signal and the KPI trigger (= BH2 timing) was very wide (2.5 μs) in the trigger level. This window corresponds to the gate width for the peak-sensitive ADC modules for the readout of the Ge detectors, and is much wider than the time resolution of the Ge detector ($\sim$15 ns at E_γ= 1 MeV). Therefore, an event selection using a tight time window was applied to improve a signal to noise ratio in the γ-ray energy spectrum.

Furthermore, background events from incomplete charge correction of the Ge detectors and from Compton scattering were rejected in the off-line analysis described in this section.

B.1.1 Coincidence events with the (K^-, π^-) reaction

To select γ rays from the produced hypernuclei in the off-line analysis, we took a coincidence between the Ge detector and the KPI trigger, using timing information of the Ge detectors which was processed through the Timing-Filter Amplifier (TFA) and the Constant-Fraction Discriminator (CFD) and then was digitized by the multi-hit TDC modules. CFD modules were used because of a large dynamic range of Ge signals which results in pulse height (energy) dependent timing. Even though the timing signal was processed through the CFD modules, the recorded timing distribution has a correlation with the ADC value. Figure 47 shows a typical correlation between the timing distribution (Ge detector$-KPI$ trigger) and the measured γ-ray energy (E_γ). A tight timing window can be applied for an energy region of $E_\gamma > 600$ keV, while a wider window is necessary for the lower energy region. In the present analysis, however, we concentrated on the energy region of $\sim$ 1 MeV for the γ ray from ${}^{4}_{\Lambda}$He. Figure 48 shows a typical timing distribution for an energy region of 600 keV $< E_\gamma <$ 7000 keV. A typical time resolution of the Ge detector was 13 ns (FWHM) for the measured energy region of 600–7000 keV. Also the width of the timing window for this event selection was set typically 50 ns, which was optimized for each Ge detector.

B.1.2 Background events

Preamplifier reset and pulse pileup In the pulse shaping process by the main amplifier (UHA 973U), some of the pulses suffer from two factors: (1) a base line shift in the output signal of UHA 973U caused by the reset of the preamplifier, (2) a signal pileup which occurs when more than two pulses arrive within the integration time of UHA 973U.

When a pulse rides on a distorted base line following a reset, the measured pulse height and thus the energy will be shifted in peak-sensitive ADC modules. Figure 49 shows a typical correlation between the ADC value and the timing of the reset. In the figure, the Reset Time (RT) was defined as "KPI trigger - reset signal from the preamplifier". The reset timing pulse was output from the preamplifier and then was digitized by the multi-hit TDC. The effect of the base line shift is seen in the region of RT $\simeq$ 40 μs. Furthermore, the reset makes a fake peak at a particular energy ($\sim$300 keV) for a typical detector as shown in Fig. 49. The recorded energy of the fake peak is less than 600 keV. Therefore, the fake peak will not affect in the energy region of $E_\gamma > 600$ keV, even when the event selection with the reset timing associated with the fake peak was not applied. To reject pulses affected by the reset, hit information of a Ge detector was removed in the off-line analysis, when the recorded reset timing is in the gate of 5 μs $<$ RT $<$ 55 μs. The time window is illustrated in Fig. 49.

The pulse height for the piled-up events become larger because of summing of more than one pulse within the integration time of the UHA 973U module, which is set to be 3 μs in the present experiment. Therefore, those events in which there is more than one hit in a Ge

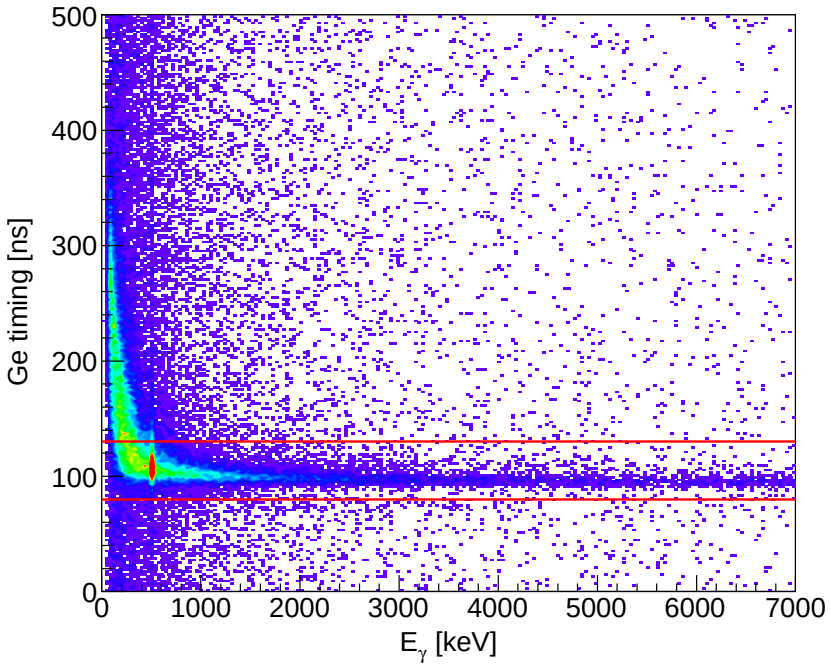

Figure 47: Typical correlation between the timing distribution (Ge detector$-KPI$ trigger) and the measured γ-ray energy (E_γ).

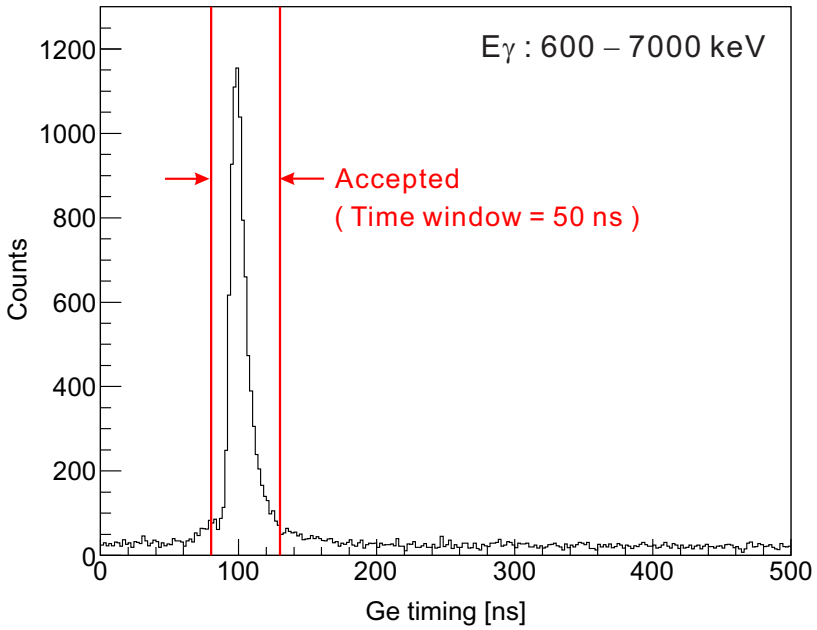

Figure 48: Typical timing distribution for an energy region of $E_\gamma > 600$ keV.

detector in the ± 3 μs time gate were removed in the off-line analysis.

Background suppression with PWO counters Backgrounds in the γ-ray spectrum originate from such as Compton scattering, electro magnetic shower due to high energy γ rays from π^0 decay, and passing of a high energy charged particle. These events can be suppressed by taking an anti-coincidence between the Ge detector and surrounding PWO counters. Figure 50 shows a typical time distribution of the PWO counters, where the time difference between the PWO counter and the KPI trigger (= BH2 timing) is used instead of the corresponding Ge detector timing which has worse time resolution than BH2. The time resolution of the PWO counters was 8 ns (FWHM). The anti-coincidence gate width was set to be 50 ns, which was studied in the test experiment with a known γ ray from ^{10}B [34]. The anti-coincidence gate was illustrated in the Fig. 50. The rate of accidental killing of good events was estimated to be 1% in the present analysis, which is smaller than that with conventional BGO counters, due to the short decay constant of the PWO crystal.

Figure 51 shows the γ-ray energy spectra for the KPI triggered events before/after the background suppression with the anti-coincidence of the PWO counters. In the spectrum, the event selection based on the timing information of the Ge detectors (the TFA timing cut, the preamplifier reset and the pulse pileup rejection) was made. As shown in this figure, the background events were suppressed while the γ-ray peaks from normal nuclei were not. The suppression efficiency depends on the γ-ray energy. Background events were suppressed by a factor of $\sim$3 at the energy region of $E_\gamma = 1$ MeV.

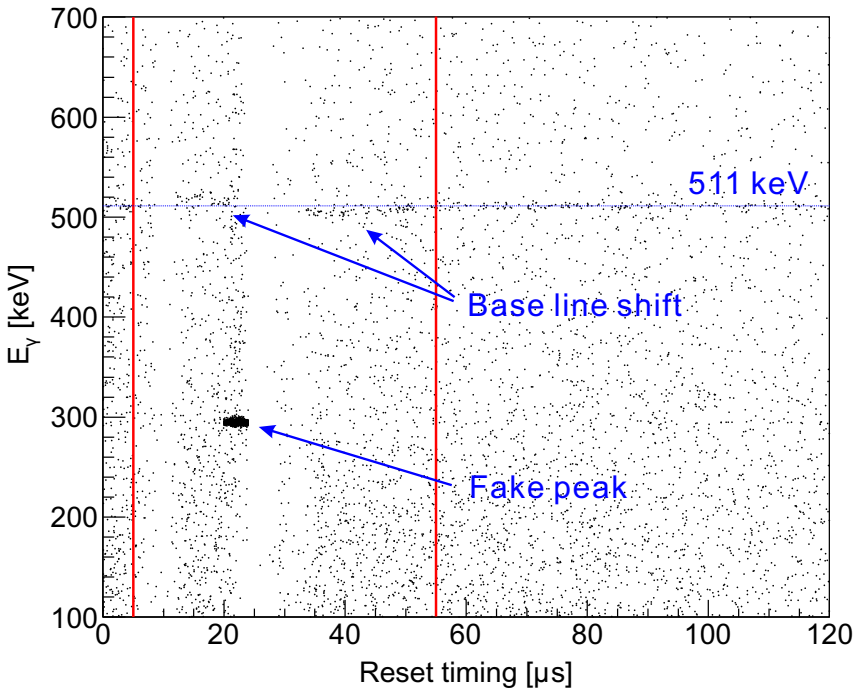

Figure 49: Typical correlation between the ADC value and the Reset Time (RT= KPI trigger - reset signal).

B.2 Energy calibration of Ge detectors

The energy calibration for the Ge detector can be separated in two steps; the first is to obtain an energy calibration curve in the off-beam-spill period, and the second is correction of a peak shift between the on-beam-spill and the off-beam-spill periods. These two analyses for the energy calibration are described in this section.

B.2.1 Calibration curve

The energy range of the Ge detectors was set to be 0.15–7 MeV. The low energy end (0.15 MeV) corresponds to the threshold of CFD. The high energy end (7 MeV) was decided because the highest γ-ray energy from ${}^{19}_{\Lambda}$F is expected to be $\sim$6 MeV. (We also took data for a γ-ray spectroscopy of ${}^{19}_{\Lambda}$F with the same setup, and the result will be reported elsewhere.) In the present analysis, we concentrated on the energy region of $\sim$1 MeV for γ rays from ${}^{4}_{\Lambda}$He. Therefore, the energy calibration was performed for the narrow energy region of 0.5–2.6 MeV. We applied a two-step calibration by using the off-beam data. First, a gain drift is corrected by applying a rough energy calibration with γ rays from the Th-series source during the beam time on daily basis. Second, an energy calibration curve is obtained with γ rays from ^{152}Eu just after the beam time.

We took calibration data with the Ge self-trigger in the off-beam-spill period, where γ rays from the Th-series source installed adjacent to each Ge detector were observed. Figure 52 shows

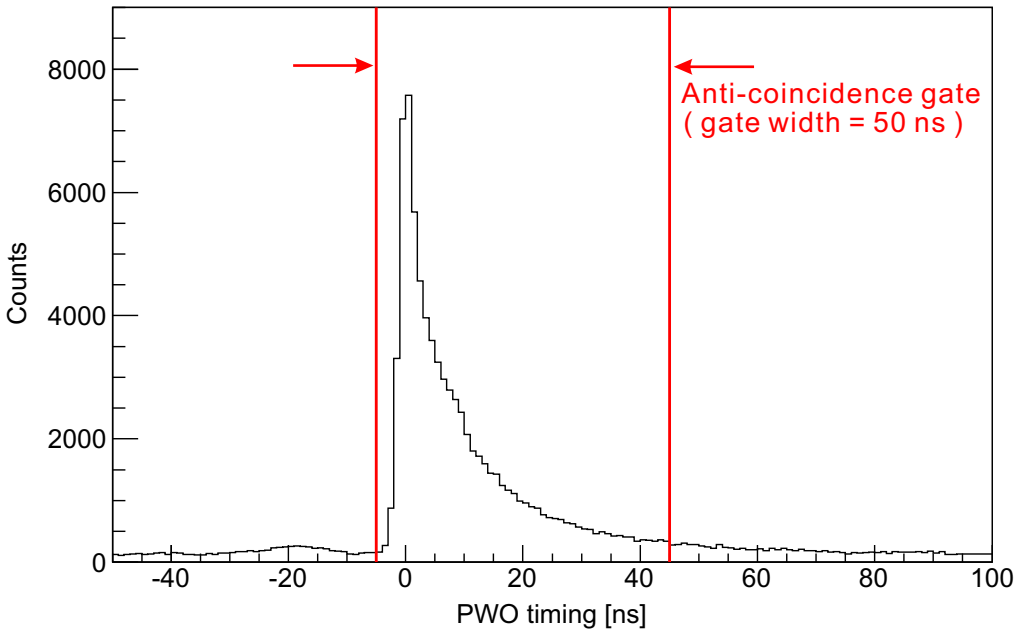

Figure 50: Typical time distribution of the PWO counters. The time difference between the PWO counter and the KPI trigger (= BH2 timing) is used.

Table 11: Selected γ rays from the Th-series source for the gain shift correction. SE denotes a Single-Escape peak.

Parent nucleus	γ-ray energy [keV]
^{208}Tl	583.2
^{228}Ac	911.2
^{208}Tl (SE 2614 keV)	2103.5
^{208}Tl	2614.5

a γ-ray energy spectrum obtained with the Ge self-trigger in the off-beam-spill, for $\sim$1 hour which equals the run cycle of the KPI triggered data. γ-ray peaks are seen between 0.5 and 2.6 MeV in this spectrum. We selected four γ-ray peaks as "clean peaks" and used them for correcting the gain shift. The selected γ rays from the Th-series source are listed in Table 11. The other peaks were not used because of overlap with other γ-ray peaks or insufficient statistics after one day data taking. Figure 53 shows drift of the peak position of 2.6 MeV (^{208}Tl) γ ray for a typical Ge detector through out the data taking period where x-axis is a run number of the KPI triggered data. The drift of the peak position was $\pm$0.8 ADC channel, corresponding to $\pm$ $\sim$0.7 keV. To correct this gain shift, a rough calibration curve was determined by fitting these calibration energies with a 2nd-order polynomial function.

A more accurate calibration curve was obtained with the data taken just after the beam time, where γ rays from ^{152}Eu source were added. 4th-order polynomial correction function

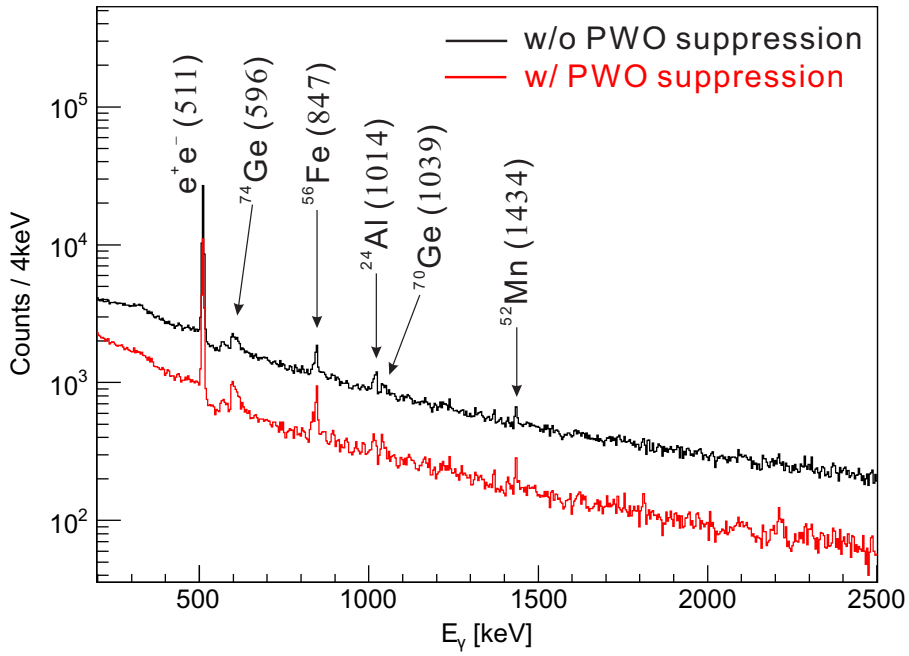

Figure 51: γ-ray energy spectra for the KPI triggered events before/after the background suppression with the anti-coincidence of the PWO counters. In the spectrum, events with Ge detector hits in the correct timing are selected via the TFA timing cut, as well as rejecting bad events via timing cuts for the preamplifier reset and the pulse pileup.

Table 12: γ-ray peaks used in the fitting for accurate energy calibration. SE denotes a Single-Escape peak.

Parent nucleus	γ-ray energy [keV]
^{208}Tl	583.19
^{212}Bi	727.33
^{152}Eu	778.90
^{228}Ac	911.20
^{152}Eu	1112.07
^{152}Eu	1408.00
^{228}Ac	1630.63
^{208}Tl (SE 2614 keV)	2103.51
^{208}Tl	2614.51

was obtained by fitting the "roughly energy calibrated" peak positions of γ rays from ^{152}Eu and Th-series source. γ-ray peaks used in the fitting are listed in Table 12. Figure 54 shows residuals of the fitting. Accuracy of the energy calibration for the whole data set is discussed in Section B.5.1.

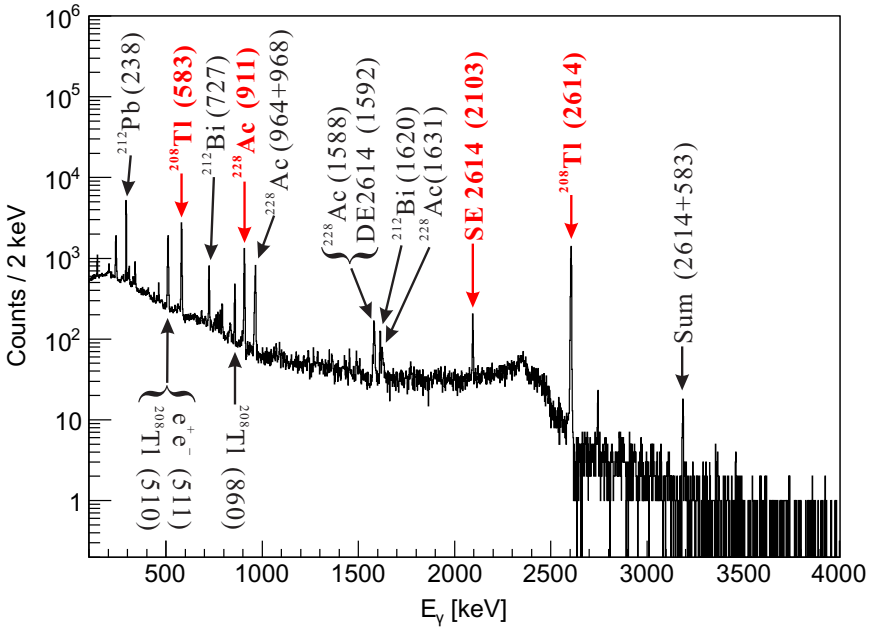

Figure 52: γ-ray energy spectrum with the Th-series source. The data was taken with the Ge self-trigger in the off-beam-spill. The data taking time was $\sim$1 hour.

B.2.2 Peak shift

In beam-on conditions, γ-ray peak positions shifted to lower energy by 1 keV or less compared to the beam-off conditions. A higher single counting rate of the Ge detector caused the base line to shift in the main amplifier (UHA 973U). A similar shifting of peaks was also observed in the previous experiments with Ge detector arrays, Hyperball and Hyperball-2 [35, 36, 10]. To correct for the peak shift, measured γ-ray energies were shifted by a constant value so as to bring the annihilation peak to 511 keV. We did not include a gain shift in this correction. No gain shift was observed from the measured peak position of the 2614-keV γ-ray peak in all summed up spectrum of the on-beam-spill, which peak can be appears by an accidental coincidence with the KPI trigger.

B.3 Doppler-shift correction

The $M1$ γ-ray transition from ${}^{4}_{\Lambda}$He is expected to be Doppler broadened because the life time of ${}^{4}_{\Lambda}$He(1^+), estimated to be of $\sim$0.1 ps assuming the excitation energy of 1 MeV, is much shorter than the stopping time of the recoiling ${}^{4}_{\Lambda}$He ($>$ 25 ps). See Section A.7 for the detailed description of the Doppler broadening.

Measured γ-ray energies were corrected for the Doppler shift event by event by using the following equation,

$$E_\gamma^{\rm corrected} = E_\gamma^{\rm measured} \cdot \frac{1}{\sqrt{1-\beta^2}}(1-\beta\cos\theta_\gamma),$$

where β denotes the recoil speed of ${}^{4}_{\Lambda}$He obtained from the analysis of the (K^-,π^-) reaction. θ_γ

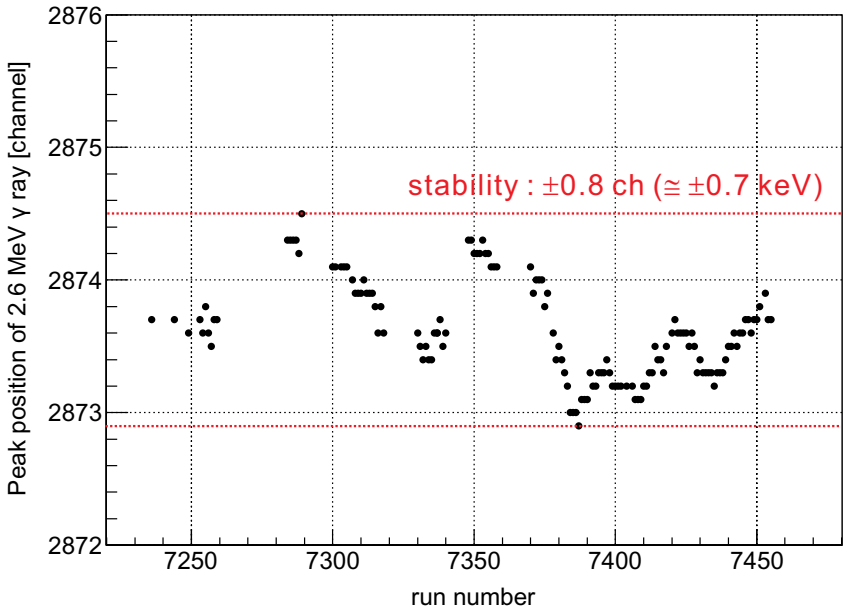

Figure 53: Peak position drift of the 2.6 MeV (^{208}Tl) γ ray for a typical Ge detector through out the data taking period (10 days in total), where x-axis is a run number of the KPI triggered data.

is the angle between the γ-ray vector and the momentum of $^{4}_{\Lambda}$He, where γ-ray vector originates from the reaction vertex point and ends at a center position of the Ge crystal with a hit.

B.4 Performance of Hyperball-J

B.4.1 Accuracy of the energy calibration

The accuracy of the energy calibration over the entire data-taking period was checked by using data accumulated in the off-beam-spill period, and summed up for all the beam time. Figure 55 shows the residuals between measured and their known γ-ray energies. In this figure, only prominent peaks are shown; the others have insufficient statistics or overlap with neighboring peaks. A overall accuracy of the energy calibration in the range of 0.6–2.6 MeV was estimated to be less than 0.4 keV from these residuals. (see the section 4.3.1****).

B.4.2 Energy resolution

The energy resolution of Hyperball-J was measured by summing up all of the off-beam-spill data (Ge self-triggered data) for all the Ge detectors. Figure 56 shows the energy resolution in FWHM as a function of the γ-ray energy. The peak width of Single-Escape (SE) peak of 2614-keV γ ray at 2103 keV is broadened by in-flight annihilation of a positron with an electron. The energy resolution is expected to be a root-squared function of the energy as

$$\delta E = \sqrt{A \cdot E_\gamma + B^2},$$

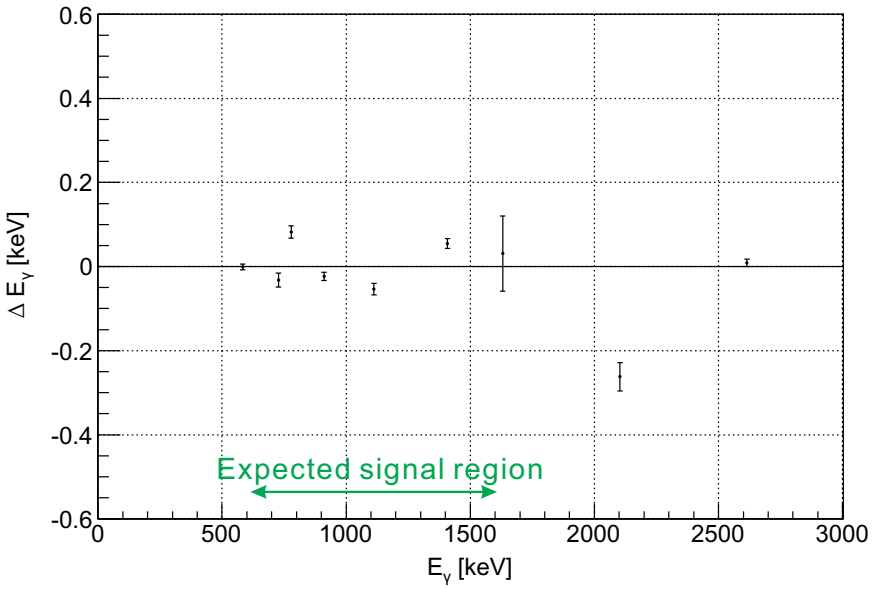

Figure 54: Residuals of the fitting to obtain the energy calibration curve for typical Ge detector with ^{152}Eu and Th-series sources.

where parameters A and B are obtained by fitting the measured energy resolution excluding the 2103-keV peak. The obtained function is also shown in Fig. 56 with A = 5.03(4) $\times$ 10^{-3} keV and B = 3.92(1) keV. The in-beam resolution was checked with the 1434-keV (^{52}Mn) and the 2614-keV (^{208}Tl) peaks produced by the beam. They are seen in the KPI-triggered data without applying an event selection by taking coincidence between the Ge detectors and the KPI trigger. Under the in-beam condition, B = 4.40(8) keV was obtained by fitting these peaks with a fixed value of A from the off-beam-spill.

B.4.3 Expected peak shape with Doppler-shift correction

The γ-ray peak shape broadened by the Doppler effect and also its shape after the Doppler-shift correction were simulated. Conditions for the simulation are listed below,

- response function of the Ge detector for a stopped γ-emission peak was assumed to be Gaussian with the expected peak width described in Section B.5.2,
- measured positions of the detector and the target were used,
- γ-ray source point was generated over the target volume taking the beam x- and y-profile into account,
- momentum of the hypernucleus was calculated with the ^{4}He$(K^-,\pi^-)^4_\Lambda$He kinematics assuming the mass of $^4_\Lambda$He to be $M(^3\mathrm{He})+M(\Lambda)-B_\Lambda(=2.39$ MeV$)+$ $E_{\mathrm{ex}}(=1$ MeV$)$,
- measured performance of the magnetic spectrometers, such as the reaction vertex resolution and the momentum resolution for a recoiling hypernucleus, were considered.

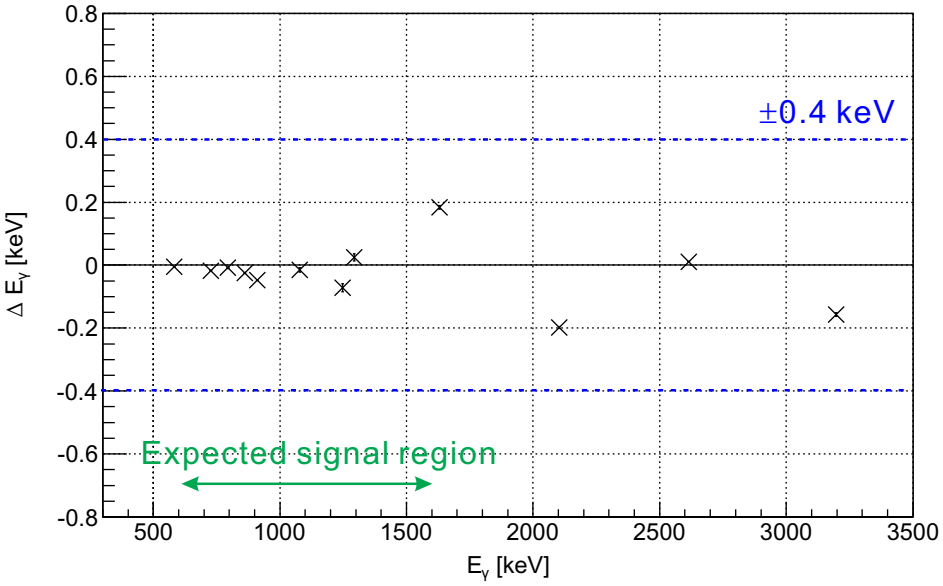

Figure 55: Residuals of the measured γ-ray energy position from known energies. The residuals were obtained by using data accumulated in the over all the off-beam-spill period and summed up for all of the Ge detectors.

Figure 57 shows simulated peak shapes for the 1-MeV γ rays. The peak widths of the simulated peak shapes are 5, 90 and 14 keV (FWHM) for the stopped γ-emission peak, the Doppler-broadened peak and the Doppler-shift corrected peak, respectively. The simulated peak before the Doppler-shift correction has an asymmetric shape because the numbers of Ge detectors located at the upstream side and at the downstream side in Hyperball-J with respect to the target center are different. The peak width after the Doppler-shift correction is wider than the stopped γ-emission peak shape due to inaccuracy of the measured momentum of the hypernucleus, the reaction vertex position, and the γ-ray hit position (assumed to be the center of the Ge crystal).

B.4.4 Photo-peak efficiency

The absolute photo-peak efficiency of Hyperball-J was estimated by using a simulation based on the Geant4 code. In the simulation, we incorporated the measured detector positions, all materials around the Ge crystals, and γ-ray absorption in the target medium. The efficiencies of the data acquisition system and the analysis were not taken into account.

Figure 58 shows the simulated total absolute photo-peak efficiency of Hyperball-J as a function of γ-ray energy. In this figure, a black line shows the efficiency with a point source placed at the center of Hyperball-J and without the target material, and a red line shows the efficiency when γ ray is uniformly generated in the liquid helium target. The efficiency shown in the red line was smaller than that of the point source shown in the black line. This is because there is an effect of absorption in the target material and an effective solid angle for source position distributing over the target volume is smaller. The dependence of the simulated

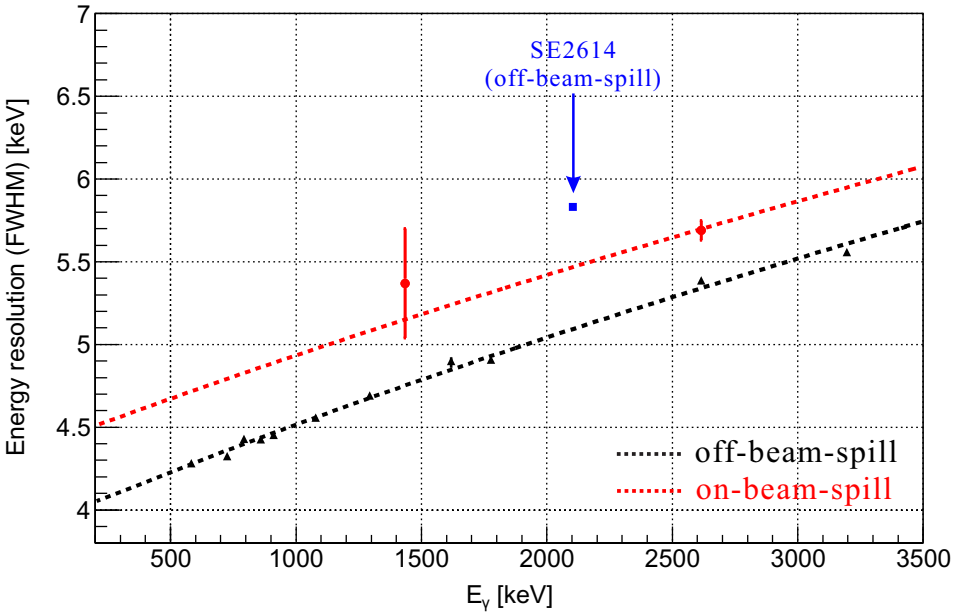

Figure 56: Energy resolution in FWHM as a function of the γ-ray energy. Black triangle shows measured energy resolutions from the off-beam-spill data, and red point shows the in-beam resolution. The resolution functions ($\sqrt{A \cdot E_\gamma + B^2}$) for the off-beam-spill (dotted black line) and for the on-beam-spill (dotted red line) are also shown.

efficiency on energy was derived from the measured relative efficiency of γ rays from a ^{152}Eu source. The measured relative efficiency was scaled and plotted in Fig. 58. Absolute efficiency was not obtained from data with a ^{152}Eu source because of uncertainty in the live time of the data acquisition. To check the absolute efficiency, additional data were taken with a ^{60}Co source and a 2" NaI counter as a γ tagging counter. Absolute value of the simulated efficiency at the energy of 1.17 MeV was compared to the measured efficiency with a ^{60}Co source where angular correlation between the two γ rays from ^{60}Co was taken into account in the simulation. From this comparison, a scaling factor ($\epsilon_{\rm measured}/\epsilon_{\rm simulated}$) of 0.76 was obtained to be applied to the simulated efficiency curve. A less than one scaling factor would be due to idealized geometry and size of Ge crystal in the simulation. In addition, actual mechanical structure of Ge detectors are much simplified in the simulation.

Real efficiency of Hyperball-J is expected to be further reduced by two effects: (1) an in-beam live time of the Ge detectors which was measured to be typically 96% from the analysis of the Ge×LSO triggered data (2) over-kill due to the accidental suppression by the PWO counters which was estimated to be of 1%. In total, the actual efficiency of Hyperball-J was estimated to be 95% of the efficiency curve in Fig. 58.

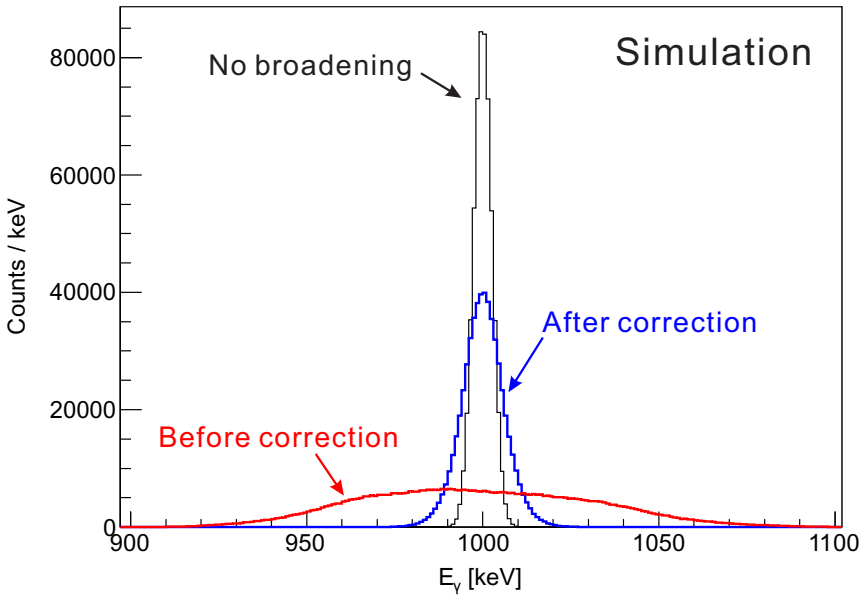

Figure 57: Simulated peak shapes for the 1-MeV γ rays. Black line is the peak shape with no Doppler effect. Red and blue lines are the Doppler broadened and the Doppler-shift corrected peak shapes, respectively.

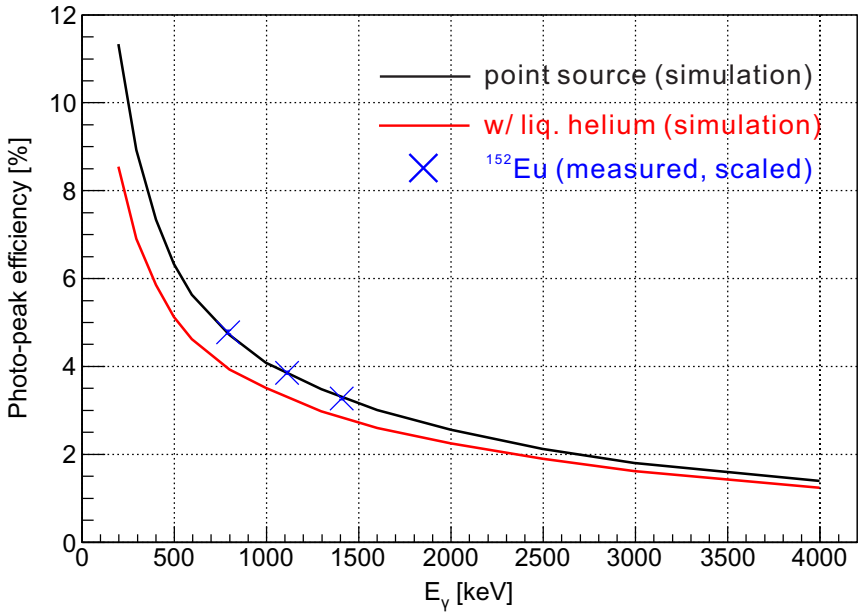

Figure 58: Simulated total photo-peak efficiency of Hyperball-J as a function of γ-ray energy. Black line is the efficiency with a point source placed at the center of Hyperball-J, and red line is that with the liquid helium target system and with randomly distributed γ-ray source points. Blue points are measured relative efficiency for γ rays from a ^{152}Eu source.

References

[1] T.O. Yamamoto *et al.*, Phys. Rev. Lett. 115 (2015) 222501.

[2] H. Tamura et al., J-PARC proposal E63, "Gamma-ray spectroscopy of light Λ hypernuclei II".

[3] K. Tanabe, Master thesis, Tohoku University, 2014.

[4] R. Honda, K. Miwa, Y. Matsumoto, N. Chiga, S. Hasegawa, K. Imai, Nucl. Instr. Meth. A 787 (2015) 157.

[5] T. Fukuda et al., Nucl. Instrum. Methods A361 (1995) 485.

[6] T. Takahashi *et al.*, Prog. Theor. Exp. Phys. (2012) 02B010.

[7] J. Myrheim and L. Bugge, Nucl. Instr. Meth. 160 (1979) 43.

[8] J. Myrheim and L. Bugge, Three Dimentional Computer Program (TOSCA) for Non-Linear Electromagnetic Fields, RL-81-070557 (1982).

[9] H. Hotchi, Doctoral thesis, University of Tokyo, 2000.

[10] K. Hosomi, Doctoral thesis, Tohoku University, 2013.

[11] M. Ukai *et al.*, Phys. Rev. C 73 (2006) 012501.

[12] T. Nagae et al., Phys. Rev. Lett. 80 (1998) 1605.

[13] T. Koike *et al.*, Nucl. Instr. Meth. A 770 (2014) 1.

[14] E. Hull, R.H. Pehl et al., IUCF Ann. Rep. (1993) 143.

[15] T.O. Yamamoto, Master thesis, Tohoku University, 2009.

[16] Y. Igarashi et al., IEEE Trans. Nucl. Sci. 57 (2010) 618.

[17] R. Honda and K. Miwa, Proceedings of 3rd International Workshop on New PhotonDetectors, PoS Press (2012) 031.

[18] Y. Igarashi et al., IEEE Trans. Nucl. Sci. 52 (2005) 2866.

[19] I. Shindo et al., J. Nucl. Mterials 79 (1979) 418.

[20] K. Tanida *et al.*, J-PARC proposal E03, "Measurement of X rays from Ξ^- Atom".

[21] T.O. Yamamoto, Doctoral thesis, Tohoku University, 2016.

[22] K. Shirotori et al., Phys. Rev. Lett. 109 (2012) 132002.

[23] T. Harada et al., Private communication, 2006.

[24] M. Moritsu et al., Nucl. Phys. A 914 (2013) 91.

[25] Y. Ichikawa wt al., Prog. Theor. Exp. Phys. 2014 (2014) 101D03.

[26] H. Sugimura et al., Phys. Lett. B 729 (2014) 39.

[27] O. Hashimoto and H. Tamura, Prog. Part. Nucl. Phys. 57 (2006) 564.

[28] P. Dluzewski et al., Nucl. Phys. A 484 (1988) 520.

[29] M. Juric et al., Nucl. Phys. B 52 (1973) 1.

[30] J.F. Ziegler *et al.*, "SRIM–The Stopping and Range of Ions in Matter", *http://www.srim.org/*

[31] R.H."Dalitz and A. Gal, Annals Phys. 116 (1978) 167.

[32] Y. Sasaki, Master thesis, Tohoku University, 2014.

[33] H. Outa et al., Nucl. Phys. A 754 (2005) 157c.

[34] A. Sasaki, Master thesis, Tohoku University, 2013.

[35] K. Tanida, Doctoral thesis, University of Tokyo, 2000.

[36] M. Ukai, Doctoral thesis, Tohoku University, 2004